

AD-A013 336

LABORATORY INVESTIGATION OF WAVE  
BREAKING. PART II. DEEP WATER WAVES

W. G. Van Dorn, et al

Scripps Institution of Oceanography

Prepared for:

Office of Naval Research  
Advanced Research Projects Agency

June 1975

DISTRIBUTED BY:

**NTIS**

National Technical Information Service  
U. S. DEPARTMENT OF COMMERCE

230112

Advanced Ocean Engineering Laboratory  
Scripps Institution of Oceanography  
University of California, San Diego

ADA013336

## LABORATORY INVESTIGATION OF WAVE BREAKING

### Part II: Deep Water Waves

by  
W. G. Van Dorn  
S. E. Pazan

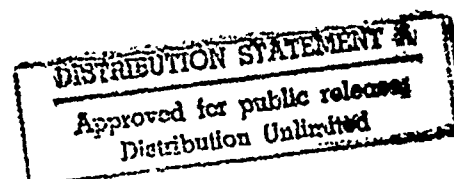
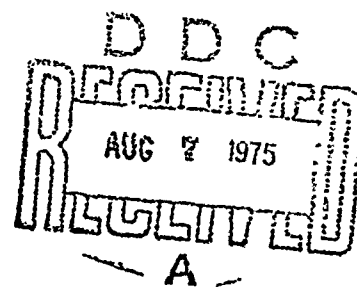
SIO Reference Number 75-21  
AOEL Report #71

This research was sponsored by the  
Advanced Research Projects Agency  
Advanced Engineering Division  
and administered by the  
Office of Naval Research  
Contract N00014-69-A-0200-6012

Reproduced by  
NATIONAL TECHNICAL  
INFORMATION SERVICE

U.S. Department of Commerce  
National Technical Information Service  
Springfield, VA 22151

June 1975



Unclassified

SECURITY CLASSIFICATION OF THIS PAGE (When Data Entered)

REPORT DOCUMENTATION PAGE		READ INSTRUCTIONS BEFORE COMPLETING FORM
1. REPORT NUMBER SIO Reference No. 75-21	2. GOVT ACCESSION NO.	3. RECIPIENT'S CATALOG NUMBER
4. TITLE (and Subtitle)  LABORATORY INVESTIGATION OF WAVE BREAKING Part II: Deep Water Waves		5. TYPE OF REPORT & PERIOD COVERED Final Report Jan. 1972 - Dec. 1974
7. AUTHOR(s) W. G. Van Dorn S. P. Pazan		6. PERFORMING ORG. REPORT NUMBER AOEL No. 71
9. PERFORMING ORGANIZATION NAME AND ADDRESS Advanced Ocean Engineering Laboratory Scripps Institution of Oceanography P.O. Box 1529, La Jolla, Calif. 92037 (714) 452-3496		8. CONTRACT OR GRANT NUMBER(s)  N00014-69-A-0200-6012
11. CONTROLLING OFFICE NAME AND ADDRESS Advanced Research Projects Agency 1400 Wilson Boulevard Arlington, Virginia 22217		10. PROGRAM ELEMENT, PROJECT, TASK AREA & WORK UNIT NUMBERS  NR 294-016
14. MONITORING AGENCY NAME & ADDRESS (if different from Controlling Office) Office of Naval Research 800 N. Quincy Street Arlington, Virginia 22217		12. REPORT DATE July 1975
		13. NUMBER OF PAGES 110
		15. SECURITY CLASS. (of this report) Unclassified
		15a. DECLASSIFICATION/DOWNGRADING SCHEDULE
16. DISTRIBUTION STATEMENT (of this Report) Distribution of this document is unlimited		
17. DISTRIBUTION STATEMENT (of the abstract entered in Block 20, if different from Report)		
18. SUPPLEMENTARY NOTES		
19. KEY WORDS (Continue on reverse side if necessary and identify by block number)  Waves: Breaking of Flow Fields Within Energy Losses		
20. ABSTRACT (Continue on reverse side if necessary and identify by block number)  This study represents the first known attempt to examine in some detail the flow dynamics of the terminal growth and breaking of periodic surface waves in deep water, under controlled and reproducible laboratory conditions. This work was considered a necessary preliminary to future studies of storm wave breaking, a phenomenon of considerable engineering importance that has received little scientific attention.  In the present study, a tape-controlled servo-paddle system produced single-frequency, deep water wave trains, which were laterally converged to the		

DD FORM 1 JAN 73 1473

EDITION OF 1 NOV 68 IS OBSOLETE  
S/N 0102-LF 014-6601

Unclassified

SECURITY CLASSIFICATION OF THIS PAGE (When Data Entered)

Unclassified

SECURITY CLASSIFICATION OF THIS PAGE(When Data Entered)

breaking point within a tapered channel. Using high-response elevation and velocity sensors, profiles and internal velocity fields of growing waves were determined as functions of time and distance before and after breaking. Parametric analysis of these data yielded the following descriptions of consecutive growth stages.

- 1) For wave steepnesses smaller than 0.1, wave profiles remained fairly symmetric, and all observed properties corresponded reasonably to those given by Stokes fifth-order theory.
- 2) For steepness within the range  $0.1 < H/L < 0.12$ , wave development was characterized by increasing profile asymmetry, steepening of the forward face, and forward tilting and upward concentration of internal isolines of constant velocity. These changes were confined to the upper 30 percent of the wave height. The rate of increase of potential energy density along the channel before breaking was found to be inversely related to channel width, consistent with conservation of energy flux.
- 3) Wave breaking occurred upon attainment of steepnesses within the range  $0.125 < H/L < 0.140$ , and was associated with near-verticality of the forward crest face, and distortion of velocity isolines so as to wrap around a jet issuing from the forward face just below the crest. The vertical profiles of maximum horizontal velocity were essentially hyperbolic, and maximum jet velocity exceeded the local crest velocity by as much as 10 percent. The latter velocity was found to closely approach the theoretical limit,  $C_* = 1.2g/2\pi f$ , for Stokes waves of maximum height.
- 4) Breaking intensity - as determined from potential energy loss rate - was found to be correlated with the rate of potential energy increase before breaking, indicating that any deterministic theory for breaking must include some prescription of a wave's previous history.
- 5) Post-breaking energy loss rates were found to be roughly in equilibrium with energy input resulting from continuing channel convergence.

ia

Unclassified

SECURITY CLASSIFICATION OF THIS PAGE(When Data Entered)

**Advanced Ocean Engineering Laboratory  
Scripps Institution of Oceanography  
University of California, San Diego**

# **LABORATORY INVESTIGATION OF WAVE BREAKING**

## **Part II: Deep Water Waves**

by

W. G. Van Dorn

S. E. Pazan

**NO Reference Number 75-21  
AOEL Report #71**

This research was sponsored by the  
Advanced Research Projects Agency  
Advanced Engineering Division  
and administered by the  
Office of Naval Research  
Contract N00014-69-A-0200-6012

**June 1975**

Reproduction in whole or in part is permitted for  
any purpose of the United States Government  
Distribution of this Document is Unlimited

**ib**

TABLE OF CONTENTS

	Page
TITLE PAGE	i
TABLE OF CONTENTS	ii
SYMBOLS AND TERMINOLOGY	iv
ABSTRACT	1
1. INTRODUCTION	2
2. BACKGROUND	3
3. FACILITIES AND INSTRUMENTATION	5
3.1 Wave Channel and Convergent Barrier	5
3.2 Wave Generation	7
3.3 Velocity Measurements	9
3.4 Elevation Measurements	11
3.5 Data Acquisition	13
4. METHODOLOGY AND PROCEDURES	14
4.1 Velocity Measurement Procedures	17
4.2 Elevation Measurement Procedures	18
5. RESULTS	19
5.1 State Parameters for Waves of Finite Height	19
5.1.1 Wave Propagation Speed	27
5.1.2 Steepness-Growth Rate Diagram	31
5.1.3 Breaking Steepness	31
5.2 Stationarity in Growing Waves	33
5.3 Scaling and Similitude	36
5.4 Results of Flow Velocity Measurements	37
5.4.1 Profiles of Horizontal Velocity	38
5.4.2 Internal Velocity Fields	43
5.5 Surface Profiles	51
5.5.1 Low Steepness Profiles	51
5.5.2 Asymmetry in Steep Waves	53
5.6 Wave Energy	55
5.6.1 Energy Balance Within a Convergent Channel	57
5.6.2 Energy Flux	59

	Page
5.6.3 Viscous Dissipation	60
5.6.4 Wave Reflection	60
5.6.5 Potential Energy After Breaking	60
5.7 Energy Flux and Breaking Losses	61
5.7.1 Flux Conservation Before Breaking	64
5.7.2 Breaking Energy Loss Rate	68
6. DISCUSSION	72
6.1 Results Summary and Interpretation	72
6.2 Interactive Breaking	75
BIBLIOGRAPHY	82
APPENDIX	
A Determination of Fluid Velocity and Direction	85
B Purity of Generated Waves	92
C Energy Error Arising from Assumed Stationarity	94
D Wave Height and Potential Energy	96
E Wave Reflection	102
F Error Estimates	103
G Energy Partition in an Inhomogeneous Wave Field	105
DD Form 1473	

## SYMBOLS AND TERMINOLOGY

$c, m$  = subscripts denoting 'carrier' and 'modulation'

$f$  = frequency

$g$  = gravitational acceleration

$g_i$  = empirical cosine coefficients of probe angular response

$k = 2\pi/L$  = wavenumber

$n$  = probe response exponent

$n_i$  = radian frequency of biharmonic wave components

$t$  = time referred to arbitrary origin

$u$  = horizontal component of  $\vec{u}$

$\vec{u}$  = fluid flow velocity

$w$  = channel width

$x$  = coordinate distance from the paddle mid-position positive along the channel

$y$  = cross-channel coordinate

$z$  = vertical coordinate referred to still water level.

$a$  = asymmetry coefficient, also paddle servo voltage, probe directional coefficient

$B = (k_m n_c - k_c n_m) / k_c n_c$  = biharmonic wave parameter

$C$  = phase velocity

$C_g$  = group velocity

$C_i$  =  $i$ th order Stokes phase velocity

$C_*$  = Stokes limiting wave phase velocity

$D$  = channel depth

$E$  = total energy density

$E_k$  = kinetic energy density

$E_p$  = root-mean-square surface elevation (potential energy density =  $\rho g E_p$ )

$E_{px}$  = spatial equivalent of  $E_p$

$F$  = potential energy flux



$F_0 = F_x (G = 0.19) =$  normalizing energy flux

$F_t =$  total energy flux

$F(t) =$  initial growth function

$G = -L_* (\partial w / \partial x) / w =$  growth rate

$H =$  wave height, crest to trough

$H/L =$  wave steepness

$L =$  wavelength

$L_i = C_i / f$

$L_* = C_* / f =$  length of Stokes limiting wave

$Q =$  total energy loss rate

$Q_b =$  breaking energy loss rate

$Q_r =$  reflected energy loss rate

$Q_v =$  viscous energy loss rate

$T = 1/f =$  wave period

$U =$  fluid flow speed

$V =$  anemometer signal voltage

$V_0 =$  still water signal voltage

$\alpha = n_2 / n_1 =$  biharmonic frequency ratio

$\Delta =$  finite time or space increment

$\eta =$  surface elevation referred to still water

$\theta =$  angle of flow with respect to hot-film probe axis

$\nu =$  kinematic viscosity of water

$\rho =$  water density

$\phi =$  flow angle with respect to orthogonal probe bisector

$\omega = 2\pi f =$  wave radian frequency

$\overline{\quad} =$  overbar indicating ensemble average

$*$  = subscript for Stokes limiting wave

$\rightarrow =$  vector sign

$\nabla = \partial/\partial x + \partial/\partial y =$  differential operator

# ABSTRACT

This study represents the first known attempt to examine in some detail the flow dynamics of the terminal growth and breaking of periodic surface waves in deep water, under controlled and reproducible laboratory conditions. This work was considered a necessary preliminary to future studies of storm wave breaking, a phenomenon of considerable engineering importance that has received little scientific attention.

In the present study, a tape-controlled servo-paddle system produced single-frequency, deep water wave trains, which were laterally converged to the breaking point within a tapered channel. Using high-response elevation and velocity sensors, profiles and internal velocity fields of growing waves were determined as functions of time and distance before and after breaking. Parametric analysis of these data yielded the following descriptions of consecutive growth stages.

- 1) For wave steepnesses smaller than 0.1, wave profiles remained fairly symmetric, and all observed properties corresponded reasonably to those given by Stokes fifth-order theory.
- 2) For steepness within the range  $0.1 < H/L < 0.12$ , wave development was characterized by increasing profile asymmetry, steepening of the forward face, and forward tilting and upward concentration of internal isolines of constant velocity. These changes were confined to the upper 30 percent of the wave height. The rate of increase of potential energy density along the channel before breaking was found to be inversely related to channel width, consistent with conservation of energy flux.
- 3) Wave breaking occurred upon attainment of steepnesses within the range  $0.125 < H/L < 0.140$ , and was associated with near-verticality of the forward crest face, and distortion of velocity isolines so as to wrap around a jet issuing from the forward face just below the crest. The vertical profiles of maximum horizontal velocity were essentially hyperbolic, and maximum jet velocity exceeded the local crest velocity by as much as 10 percent. The latter velocity was found to closely approach the theoretical limit,  $C_* = 1.2 g/2\pi f$ , for Stokes waves of maximum height.
- 4) Breaking intensity - as determined from potential energy loss rate - was found to be correlated with the rate of potential energy increase before breaking, indicating that any deterministic theory for breaking must include some prescription of a wave's previous history.
- 5) Post-breaking energy loss rates were found to be roughly in equilibrium with energy input resulting from continuing channel convergence.

## 1. INTRODUCTION

The present experiments were initially proposed as the first phase of a continuing investigation of the breaking of deep water waves, such as occurs in Nature on all scales, from incipient whitecapping under light winds to massive plunging of higher waves under storm conditions. The principal argument for the overall program is that wave breaking is very little understood, but of manifest theoretical and practical importance to many areas of ocean science and technology.

- o It is generally conceded to be the principal energy loss mechanism regulating the growth of sea state toward spectral equilibrium under steady winds (Phillips, 1969, p. 109).
- o It is conceptually a more efficient mechanism for transferring momentum from wind to mean surface flow than viscous dissipation by non-breaking waves (Longuet-Higgins, 1969a), or direct tangential stress (Snyder & Cox, 1966).
- o At advanced sea states, breaking waves exert by far the largest unitized forces against ships and interfacial structures, with all their implications to ship design and operation.

In view of the above, one is led to wonder why almost all wave-oriented research within the past two decades has been directed towards wave growth mechanisms, as opposed to wave breaking. There seem to be at least two reasons. Wave breaking--as defined by turbulent energy loss--is a non-stationary and nonlinear process for which there is presently no adequate mathematical description. Second, even under steady winds, the sea surface is highly irregular and non-repeatable in time or space, so that its properties are not readily definable on a wave-by-wave basis. Instead, it has been found more practical to work with statistical or spectral representations that define only average properties and their probabilistic extremes.

In a macroscopic sense, however, breaking is a wave-by-wave phenomenon, which is believed to occur sporadically whenever random spectral components constructively interfere to locally increase the height of a particular wave to the point where it becomes unstable. While the criteria for wave instability are not known<sup>1</sup>, where the surface spectrum is reasonably narrow, as manifested by fairly regular wave groups, Donelan, et al.

---

<sup>1</sup>Phillips (1969) supposes, by analogy to the well known stability limits for progressive and standing gravity waves, that the probability of irregular waves breaking is some function of the local fluid acceleration at the surface as a fraction of the gravitational acceleration,  $g$ .

(1972) have observed (and confirmed by simple experiment) that wave breaking occurs systematically at the group antinodes, and at intervals equal to roughly twice the period of the principle waves present. This result, coupled with increasing evidence (Rye, et al., 1974) that storm spectra are much narrower than those proposed some years ago by Pierson and Moskowitz (1964), suggest the possibility that a careful series of laboratory experiments might yield descriptions of the breaking process that have application to the real ocean.

While interactive breaking is readily produced without wind in the laboratory, and is currently proposed for the next phase of this investigation, it was considered desirable to first explore the growth toward breaking of single-frequency, uniform wave trains by slow lateral convergence within a tapered channel whose depth was great enough not to significantly affect the motion. This method of approach had the following advantages:

- o wave growth was fully controllable and reproducible, and permitted detailed observation of wave properties at all stages,
- o it most nearly meets the assumptions of steady-state theories for waves of finite height,
- o it permitted control of breaking intensity by varying only initial wave amplitude, although frequency was also varied to give a greater range of initial wave steepness.

The basic research objectives of this study include:

- 1) for representative initial wave steepnesses, to make sufficiently detailed measurements of surface elevation and internal fluid velocities, as functions of time and position, so as to reasonably define the flow fields within waves approaching the breaking point,
- 2) to compare these results with relevant theories,
- 3) to attempt to parameterize breaking and breaking intensity (energy loss) in terms of observable variables, as a guide for future laboratory or field experiments with interactive breaking.

## 2. BACKGROUND

The present investigation was closely patterned after a similar set of convergent breaking experiments reported by Le Mehaute et al. (1968).

The latter were confined to shallow water waves, were conducted in a channel about half the present dimensions, and were limited to waves about one-sixth as high (10 cm). Data consisted of stroboscopic photos of surface profiles and the orbital motions of neutral-density particles of nitrile rubber. Their methodology and results are of interest here for several reasons. First, the experiment was designed to most nearly idealize the theoretical assumptions of steady motions in uniform depth. Second, the observed distributions of horizontal particle velocity beneath the wave crests (considered to be the most sensitive test of theoretical validity) were inconsistent with those predicted by any of eight theories examined. These included shallow-water expansions of Stokes waves from first- to fifth-order, Gerstner waves, and Solitary waves. Within its region of applicability, the Stokes fifth order solution gave the best fit to the observed wave profiles, and vertical velocity distributions of smaller non-breaking waves, although the observed velocity magnitudes were smaller by as much as 25 per cent. The evidence is that no present theory reasonably predicts the flow fields within steep shallow-water waves.

In deep water, the bottom boundary condition for irrotational waves becomes much simpler, and one is left, effectively, with Stokes' solutions of higher order for waves of finite height (Kinsman, 1965). Partly because of their complexity and partly because stochastic sea state models are consequently limited to linear combinations of small-amplitude waves, these solutions have not received much practical application. The current situation is summarized by Meekmeyer and Kutzbach (1965), who also present a numerical method of obtaining solutions to any order, although the conditions of profile symmetry and steady motion are still retained. As later shown, their calculated wave profile for a 15th-order wave of steepness,  $H/L = 0.1$ , is in good agreement with those observed in these experiments during the earliest growth stage.

The limiting form of a Stokes wave has been studied extensively (Lamb, 1932, pp. 418-419). The development is based on the kinematic assumption that the flow velocity at the crest cannot exceed the phase speed, and well known properties include:

- o a cusped crest symmetric about the vertical, with an included angle of  $120^\circ$ ;
- o a phase velocity 20 percent greater than that for infinitesimal waves of the same frequency:  $C_* = 1.2g/2\pi f$ ;

- o a maximum height equal to 14.2 percent of the maximum wavelength,  $L_* = C_*/f$ ;
- o a maximum crest acceleration of 0.5g directed interiorly (Longuet-Higgins, 1969b).

Various recent theoretical attempts to describe breaking all start from the Stokes limiting form and are restricted to steady motion<sup>1</sup> (Price, 1971; Longuet-Higgins, 1973, 1974). In contrast, our results indicate that breaking is strongly influenced by the rate at which waves grow, so that any realistic description of breaking must include some specification of growth rate.

### 3. FACILITIES AND INSTRUMENTATION

#### 3.1 Wave Channel and Convergent Barrier

All experiments were conducted in the 2.4 x 2.4 x 43 m (8 x 8 x 150 ft) wind-wave channel in the Scripps Institution's Hydraulic Facility (Fig. 1). For the convergent breaking experiments, a rigid barrier 2.4 m high and 24.3 m long was constructed of heavy plywood backed by steel channel frames. The frames were bolted together and through the channel bottom, and were laterally braced at the top and mid-height so that there were negligible deflections during wave passage. The barrier was faired into one channel wall about 1 m from the wave paddle and converged toward the opposite wall at a rate  $dw(x)/dx \approx 0.10$  for about 19 m, where it terminated in a hinge point at a convergence width,  $w = 51.5$  cm. An additional 6.1 m hinged barrier extension was designed to be adjustable over the range  $0 < dw/dx < 0.05$ , and could be rigidly secured in any position.

It was originally hoped that the hinged barrier might be adjusted by trial so as to maintain breakers of constant height, but this was found impossible because of strong reflections from the 1:8 beach slope just beyond the convergence. After some experimenting, it was determined that reflections could be virtually eliminated by closing the convergence to a terminal gap of 30 cm, adding a divergent extension at an angle of about 45° across the slope, and covering the upper part of the slope with wire

---

<sup>1</sup>A necessary and sufficient condition for steady motion that is that flow velocities are a function of phase only,  $\phi = kx - 2\pi ft$ .

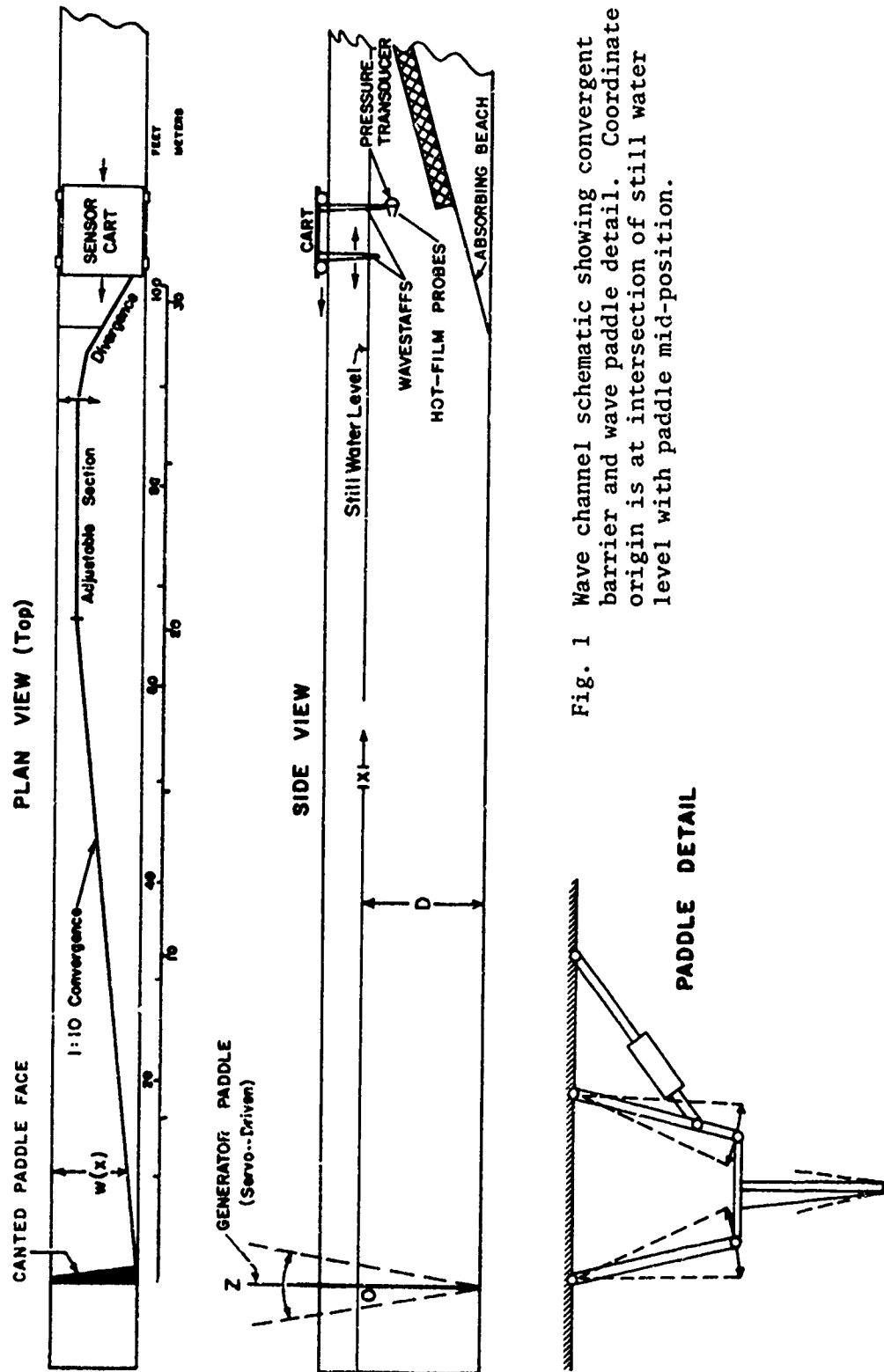


Fig. 1 Wave channel schematic showing convergent barrier and wave paddle detail. Coordinate origin is at intersection of still water level with paddle mid-position.

cages of metal turnings. All reported observations were ultimately conducted within the 1/10 convergent section, and a 1.2 m plexiglass window was cut into the channel wall 18 m from the wave paddle for sidewall photography.

Figure 1 also shows the coordinate system used throughout these experiments; the origin was located at the intersection of the still water level and the paddle mid-position, with the x-axis positive away from the paddle, and the z-axis positive upwards. While the local convergence width,  $w(x)$ , remained constant, the water depth,  $D$ , was varied with wave frequency, as later described.

### 3.2 Wave Generation

The wave generator is an integral part of the channel complex and was used without modification. It consists of a 2.5 cm plywood paddle reinforced by tapered aluminum backing struts, and dependent from a double-articulated trapezoidal framework bolted to the building roof structure (Fig. 1). By changing the spacing of the lower hinge points, the paddle motion can be adjusted to pivot about any horizontal axis from infinitely far below the channel (planar piston) to above the channel top. For these experiments, the paddle was set to pivot at the channel bottom, which position was found to produce deep water waves whose spectra were essentially free from unexpected energy peaks (App. B). To minimize cross-channel reflections that excited side modes, the paddle was fitted with a canted front face whose normal bisected the convergence angle. This resulted in very uniform wave crests which sloped up barely perceptibly at the sidewalls (Fig. 5), causing the initiation of breaking at these points an instant before it occurred along the remainder of the crest.

The wave paddle was driven by a hydraulic piston whose position was controlled by a potentiometric hydraulic servo system slaved to an electrical analog input voltage. Maximum paddle excursions corresponded to a voltage swing of about  $\pm 7$  volts, and 0-volts represented the paddle mid-position. The actual wavemaking instructions consisted of computer-produced analog signals recorded on FM tape. These were demodulated and played back to the servo to generate completely reproducible wave series as often as desired, the wave amplitude being controlled by the demodulator setting.



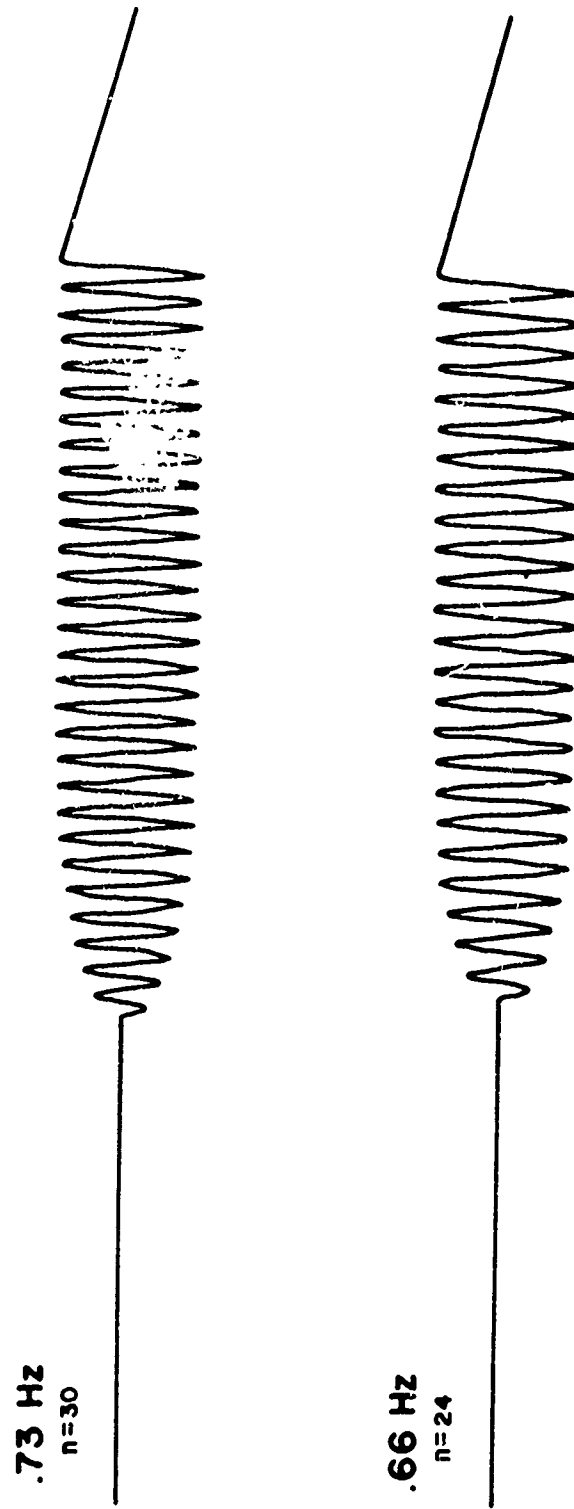


Fig. 2 Typical voltage inputs to paddle servomechanism. Paddle displacement is proportional to voltage.

Because the initial wave coming off the paddle traveled at roughly the limiting phase speed in shallow water, whereas the energy 'front' moved essentially at deep water group velocity, it was necessary to smoothly increase the paddle stroke from zero amplitude to its asymptotic uniform value in order to prevent premature breaking of those waves preceding the energy front. This was accomplished by incorporating an initial growth function,  $F(t)$ , in the paddle displacement equation

$$A = A_0 F(t) \cos(2\pi f t + b), \quad (1)$$

where  $A$  and  $A_0$  are the input and maximum servo voltages, respectively, and  $b$  is an arbitrary constant. Typical input forms for the function,  $F(t) = \tanh(2\pi f t/n + 9/4n)$ , are shown in Figure 2. For each combination of  $f$  and  $n_0$ , the constant  $n$  was adjusted by trial to obtain a continuous succession of uniform breakers at a fixed position in the channel. In most cases, the wave series was terminated by a ramp function after about 30 seconds. Scale and time reference to the paddle motion were produced by a motion transducer mounted on the paddle arm.

### 3.3 Velocity Measurements

Utilizing an orthogonal pair of DISA 55A81 wedge-shaped hot film probes coupled to DISA 55D01 constant temperature anemometers, over 600,000 individual determinations of flow speed and direction within growing waves were made during the course of these experiments. The probe shanks were encased in a watertight aluminum turret with their emergent tips abutting at right angles (Fig. 3). Since the anemometer output from a single probe is an analog voltage that is functionally related to the product of a velocity term and a direction term, the signals from two orthogonal probes whose calibration constants are known provide an unambiguous measurement of the flow vector for two-dimensional flow in the plane defined by the probe axes. While the resolution of flow speed in this plane is practically limited by backflow to the  $90^\circ$  angle subtended by the probe axes, this window could be broadened by rotating the turret in  $45^\circ$  increments in either direction.

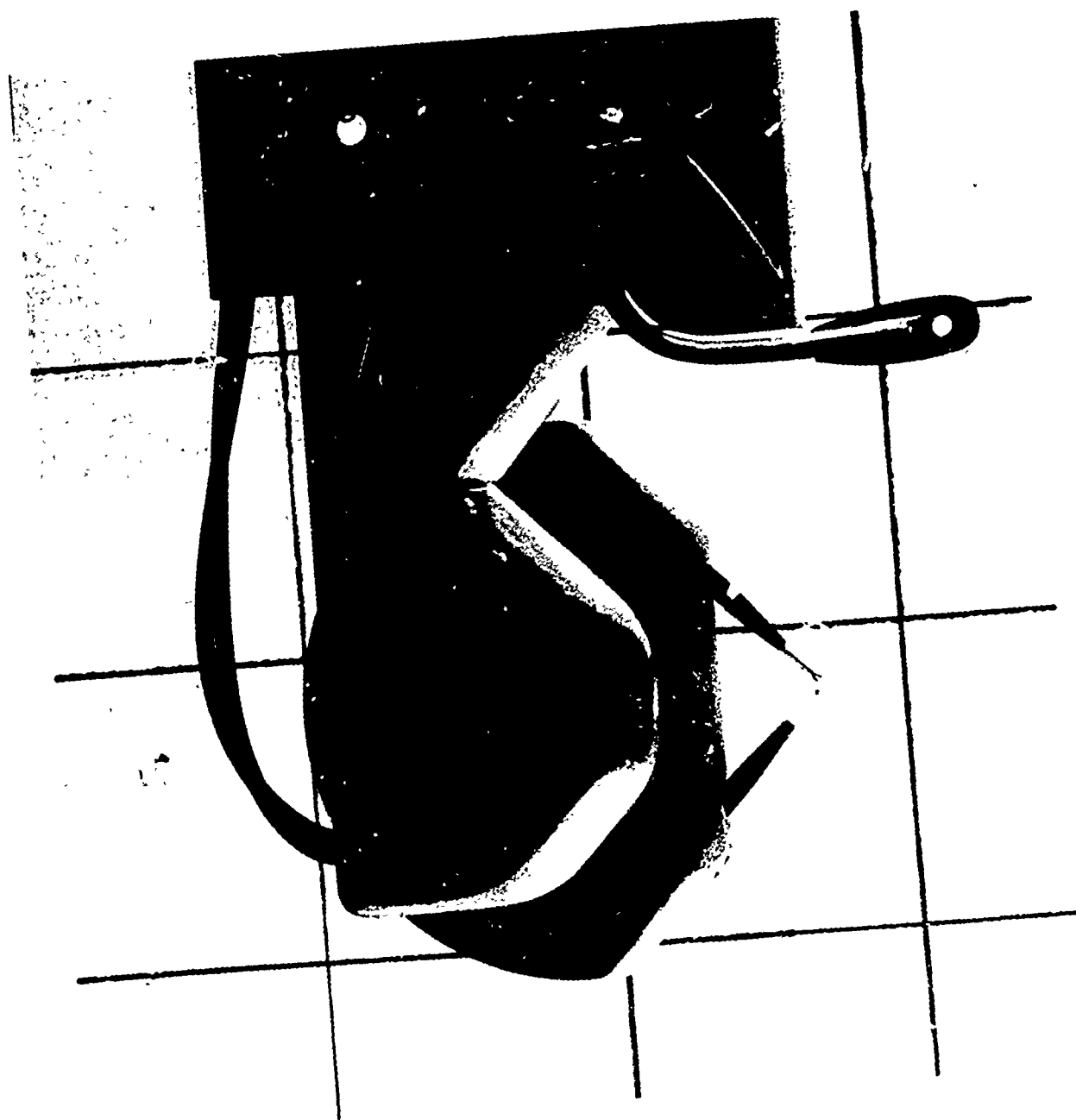


Fig. 3 Probe turret with two orthogonal hot-film probes. Tip of wave staff (above) carries a pressure sensor tap.

The probe turret was mounted on a vertical support strut dependent below an instrument cart that could be rolled to any position along the wave channel (Fig. 4). The turret plane was parallel to--and 25 cm distant from--the channel wall, or about in the middle of the convergence at its hinge point. Because principal interest was directed toward measuring high crest velocities having components in the direction of wave propagation, and because negative trough velocities were generally too low to resolve accurately, all measurements were made with the probes oriented in the semi-circle towards the wave paddle. The elevation of the turret was adjustable by a rack and pinion from an upper (calibrate) position above the water surface to approximately 1 m beneath the surface; and it could be locked in any position. Elevation control was provided by a vernier scale on the rack.

To calibrate the probes, the strut could be rotated  $90^{\circ}$  and the turret locked with the probe tips just beneath the bottom orifice of the calibrating cylinder, from which a water jet flowed over the tips at a metered rate. Because these experiments were unique and very high measurement accuracy was desired, calibration procedures and error limits are described in detail in Appendix A.

### 3.4 Elevation Measurements

For the purpose of obtaining wave profiles and their speed of travel (phase velocity,  $C$ ), measurements of surface elevation were obtained by two complimentary methods; recording wave staffs and side-window photography.

Wave staffs consisted of 120 cm tapered strips of circuit board stock exposed edgewise to the waves and bearing a vertical array of 96 gold-plated shorting contacts at 1 cm intervals. A logic circuit at the top of each staff produced an analog voltage which changed by 125 mv per immersed contact with a response rate of 20 khz. Since meniscus effects were limited to a millimeter or so, the staff resolution was 1 cm, except in breaking waves, in which case the output provided only an upper bound to surface elevation. The staffs were calibrated during data taking by generating a continuous train of waves of maximum height and examining their respective

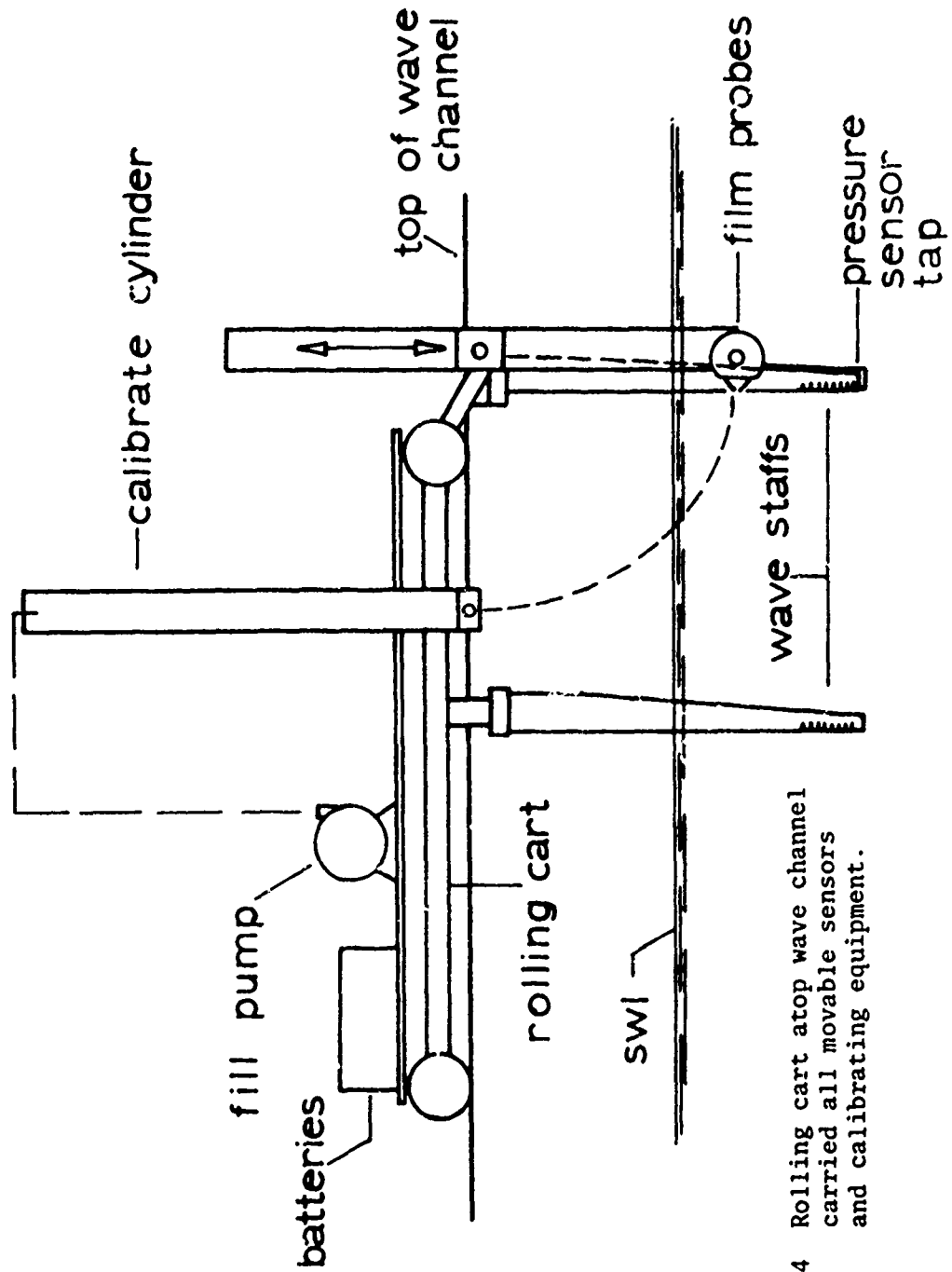


Fig. 4 Rolling cart atop wave channel carried all movable sensors and calibrating equipment.

contact shorting cycles on an oscilloscope, whose display indicated faulty contacts or incorrect bridge excitation voltages as "missing teeth".

For most of this study, three staffs were mounted on the rolling cart: two crosswise of the channel with their contact edges in the plane of the probe tips at distances of 9 cm from the channel sidewall and convergent barrier, respectively; and one staff in tandem at 9 cm from the sidewall and displaced variably toward the wave paddle at distances between 167 cm and 280 cm. The two transverse staffs provided a means of monitoring cross-channel variations in elevation (almost always less than 2 cm). The tandem staffs were generally displaced one-half wavelength apart at the operating wave frequency, from which phase velocity could be deduced from consecutive arrival times of a long train of identical waves. During other series concerned with measurement of fluid velocities, as many as four additional staffs were employed, both on the cart and at fixed locations between the cart and the wave paddle.

Although limited to the single channel viewing window, motion picture and single-frame photography provided a means of testing the accuracy of the wavestaff elevations, as well as demonstrating that a time record of surface elevation at a fixed point is practically equivalent to a wave profile in space centered on that point (see 5.2).

### 3.5 Data Acquisition

All analog sensors were serially multiplexed at the rate of 100 hz per channel through an A/D converter and stored on magnetic tape in the IBM 1130 computer. At a wave phase velocity of 280 cm/sec, this data rate produced one elevation and one velocity sample for each 2.8 cm of wave travel distance. All analog signals, including that from the paddle arm transducer were also routinely monitored on a Statos Mark 3 strip chart recorder, principally as a guide to sensor function.

In order to minimize redundant data storage, data acquisition was limited to the first 6-8 equilibrium waves of each series. This was accomplished by constructing a digital timer having an adjustable time delay which could be preset in 0.01 second intervals from zero to 120 sec.

The timer was started by a microswitch on the paddle arm, and provided the computer with a data start pulse after the preset time delay. Such precision time control provided easy identification of individual waves in separate data series made at different velocity probe elevations, and permitted time-registering of data samples to within  $\pm 0.02$  sec during the construction of velocity field contour plots.

#### 4. METHODOLOGY AND PROCEDURES

These experiments are roughly divisible into two categories according to procedures and objectives: (a) velocity measurements to define the flow fields; and (b) elevation measurements to define wave profiles, leading to estimates of potential energy flux and energy loss due to breaking. In both cases, measurements were made at several stations before breaking--and, in the latter, at several post-breaking stations--in order to define the rates of change of these properties. Similar sets of measurements were made for series of heavily breaking and lightly breaking waves, as determined only by initial wave steepness. Lastly, in some cases comparative measurements were made at three different wave frequencies (0.66, 0.73 and 0.80 hz) to determine whether or not the behavior of steep waves obeys Froude similitude, so that important wave parameters are scalable in terms of frequency only.

Before discussing procedures, the concept of growth rate and the distinction between light and heavy breaking need clarification. Prior to the measurements described herein, a series of breaking experiments was performed at constant wave frequency. Starting with a paddle stroke so small that no wave broke in the test section, the stroke was then incrementally increased. It was observed that breaking first occurred farthest from the paddle and was of the intense (plunging) type (Fig. 5). Progressively higher strokes resulted in moving the breaking point closer to the paddle and decreasing the breaking intensity (Fig. 6). The wave height at breaking was --if anything--slightly lower for barely breaking waves than for plunging waves. While the relative constancy of breaking height can reasonably be attributed to a stability limit imposed by steepness alone, the variation of breaking intensity is more logically associated with



Fig. 5 Heavily breaking 0.66 h: wave about 18 m from the paddle.





Fig. 6b Rear view of heaving breaking waves.



Fig. 6a Light breaking 0.66 Hz wave about 6 m from paddle.

corresponding variation of the scaled channel convergence rate,  $-L(\partial w/\partial x)/w$ , which increases inversely with distance from the paddle. If, as in shallow water (Van Dorn, 1975), energy flux is conserved prior to breaking, then it follows that breaking intensity is directly related to a wave's growth history within the convergence. A fundamental objective of the experiments was to explore the nature of these relationships.

#### 4.1 Velocity Measurement Procedures

Having, as above, experimentally determined the paddle strokes (tape demodulator voltages) corresponding to light and heavy breaking at the three operating frequencies,<sup>1</sup> measurement stations were established where the first four uniform waves in each series had achieved the following growth stages:

- o Young waves of relatively low steepness ( $H/L \leq 0.10$ ), at the station nearest the paddle where the waveform first became stable, as evidenced by the absence of anomalous peaks in the Fourier spectrum (App. B).
- o Pre-breaking waves of steepness  $0.10 < H/L < 0.12$ , characterised by marked profile asymmetry, and where videotape photography first exhibited specific evidence of crest instability. These locations varied by a few centimeters from wave to wave, but their respective flow fields were found to be essentially similar, except within the upper 2-3 cm beneath their crests.
- o Breaking waves, experimentally determined to have maximum horizontal flow velocities, and generally characterized by maxima of wave height and steepnesses in the range  $0.12 < H/L < 0.14$ .

These definitions are rather subjective, particularly as regards the distinction between light and heavy breaking. In fact, 'breaking' itself is better described as a continuous development, involving increasing steepness, height, profile asymmetry, and internal velocities, the rate and degree of which are all functions of frequency, initial steepness, and position along the convergence (growth rate). Probably the most useful and easily observable definition of breaking is that stage of development corresponding to maximum wave height.

---

<sup>1</sup>For dimensional consistency, water depths were adjusted to one-half the small-amplitude wavelength ( $D = g/4\pi f^2$ ), despite the fact that Miché (1944) has shown that under these conditions water depth has an insignificant influence on the properties of steep waves. This scaling, however, had the advantage that the paddle stroke amplitude was nearly the same at different frequencies for the same breaking intensity.

Because of physical limitations of the channel, it was not possible to produce both light and heavy breaking at all three frequencies at all of the above growth stages. For this reason, as well as because of the time required to make detailed velocity measurements, efforts were concentrated at a frequency of  $f = 0.66$  hz, for which the widest range of breaking intensity could be accommodated, supplemented by additional observations of heavily breaking 0.73 and 0.80 hz waves.

Measurement procedures at each station were virtually identical. Following calibration, the probe turret was initially positioned at its lowest possible elevation (88 cm above the channel bottom), the timer was set to initiate data taking with the arrival of the first uniform wave, and three or four wave series were recorded to establish repeatability. The turret was then raised by 4-5 cm, and the data sequence repeated. Elevation increments were reduced as the wave crest elevation was approached in order to better resolve high velocity gradients. Because the probe-pair acceptance angle was limited to  $90^\circ$ , repeat runs were conducted at the lower turret elevations with the turret rotated by  $\pm 45^\circ$ , so as to resolve velocity vectors making angles greater than  $45^\circ$  to the horizontal. During all velocity measurements, surface elevation was simultaneously recorded as previously described.

#### 4.2 Elevation Measurement Procedures

For the elevation measurements, ten stations along the 21.4 m test section were selected for each wave frequency. Station spacing was densest near the breaking points of pretest waves. These stations were then occupied in pairs by deploying two to three cross-channel wave staffs and one or two tandem staffs at a time, and moving them sequentially between stations. For each staff configuration, three or four duplicate wave series were generated, starting with a paddle amplitude just low enough to preclude breaking, and increasing the stroke incrementally so as to produce heavy, intermediate, and light breaking, respectively. The frequency was then changed, and the entire schedule repeated. As with the velocity measurements, not all growth stages could be produced for all frequencies, and the most extensive results were associated with 0.66 hz waves.

Because of station overlap between the velocity and elevation measurements, a complete list of station identifiers, paddle distances and associated wave heights is given in Appendix D, which is prefaced with remarks relevant to order and content.

## 5. RESULTS

### 5.1 State Parameters for Waves of Finite Height

The work of Stokes and others (Section 2.) indicates that the only independent parameter distinguishing the immediate state of steady waves of finite height from those of negligible amplitude is wave steepness,  $H/L$ , whose limiting value,  $H_*/L_* \approx 1/7$ , is ordinarily assumed to characterize breaking inception.<sup>1</sup> Since the present experiments dealt with unsteady waves, whose limiting steepnesses and breaking intensities varied significantly and clearly depended upon initial steepness and growth rate, it was early apparent that some additional growth parameter was necessary to define a wave's immediate rate of change.

In Nature, wave growth is dependent upon the relative amplitudes and speeds of the principal Fourier components of the wave field, as manifested by the 'group' phenomenon for a narrow spectrum (Section 6.2). In these experiments, growth was produced by lateral squeezing of individual waves within the converging channel. The scaled channel convergence rate<sup>2</sup> (in space) is given by:

$$G = -L_*(\partial w/\partial x)/w(x), \quad (1)$$

where  $w(x)$  is the channel width at paddle distance,  $x$ . Because  $\partial w/\partial x \approx -1/10 = \text{constant}$ , and  $w$  varied inversely with  $x$ ,  $G$  was a monotonically increasing function of  $x$  as a wave progressed down the channel, and fell within the range,  $0.165 < G < 0.75$ , for all three experimental frequencies.

If the energy flux is conserved among growing waves, then wave energetics should be determined by growth rate alone. For shoaling periodic

---

<sup>1</sup> $L_* = 1.2g/2\pi f^2$  is the Stokes limiting wavelength at frequency,  $f$  (Michell, 1944).

<sup>2</sup>Also called 'growth rate' hereinafter.

waves. Van Dorn (1975) has shown that potential energy flux is approximately conserved right up to breaking, and it was similarly found here to be conserved in deep water. A principal result of these experiments is to show that the frequency, steepness, and growth rate suffice to determine wave kinematics and energetics, and to examine how other wave properties depend upon these parameters.

Because of their relevance to all subsequent discussion, specific values of these parameters for all stations considered in this report are listed below in Tables I and II. Both tables are keyed to-and ordered in the same manner as Table D; that is, for each wave frequency, wave series A, B, C...are ordered in terms of increasing paddle stroke amplitude, measurement stations are ordered according to increasing paddle distance (and growth rate). Other tabulated parameters comprise further condensations of the repetitive series averages in Table D. The methods of averaging and the determination of error estimates are given in App. F. The 95% confidence limits for these parameters depend slightly upon the state of wave development, and are expressed below as percentages of the tabulated values:

Steepness Range	Steepness H/L	Potential Energy Density	Potential Energy Flux
<0.10	±3%	±3%	±5%
0.10-0.14	±4%	±3%	±5%
Post-breaking	±6%	±5%	±6%

Unless otherwise qualified, these confidence limits are reflected in future figures by error bars through individual data points.

In both tables, frequency,  $f$ , is that of paddle motion, later shown to be that of the principal Fourier component (App. B). Steepness was calculated from the wave height averages in Table D, divided by the Stokes 5th-order wavelength (Section 5.1.1). Growth rate was calculated from the local channel width,  $w(x)$ , the constant convergence rate,  $\partial w/\partial x = -0.097$  (elsewhere given, nominally as  $1/10$ ), and the Stokes limiting wavelength,  $L_* = 1.2g/2\pi f^2$ . Values of potential energy density are averages from Table D, and potential energy flux was obtained by multiplying them by the Stokes 5th-order group velocity (Section 5.6.2).

In Table II, small numbers 1 and 2 appearing to the left of some station numbers refer to early and late stages of 'breaking' waves, respectively, as distinguished by initial instability and terminal plunging. For heavy breaking, these distinctions tend to coincide.

Table I

State Parameters for Velocity Measurement Stations

Wave frequency  $f = 0.66$  hz, Depth  $D = 187$  cm

Breaker Type	Station	Paddle Distance $x(\text{cm})$	Channel Width $w(\text{cm})$	Growth Rate $G$	Wave Height $H(\text{cm})$	Wave Steepness $H/L$
Light	E4	959	155	0.266	52	0.126
Heavy	B3	857	166	0.250	40	0.100
Heavy	B9	1771	78	0.535	56	0.132
Heavy	B10	1848	71	0.592	58	0.136

Wave frequency  $f = 0.73$  hz, Depth  $D = 154$  cm

Heavy	F1	163	163	0.208	33	0.103
Heavy	F2	1801	75	0.454	48	0.137

TABLE II  
STEEPNESS, POTENTIAL ENERGY, POTENTIAL ENERGY FLUX

Wave frequency  $f = 0.66$  hz, Depth  $D = 187$  cm.

Station		Paddle Distance x(cm)	Channel Width w(cm)	Growth Rate G	Steepness H/L	Potential Energy Density E <sub>p</sub> (cm <sup>2</sup> )	Potential Energy Flux F(cm <sup>3</sup> /sec)
A	1	357.	214.5	0.1939	0.0624	33.5	0.44341E 04
	2	593.	191.7	0.2169	0.0667	41.1	0.55390E 04
	3	833.	168.6	0.2468	0.0679	40.5	0.54706E 04
	4	1069.	145.8	0.2855	0.0724	47.0	0.64699E 04
	5	1186.	134.5	0.3096	0.0763	50.5	0.70545E 04
	6	1379.	115.9	0.3595	0.0839	62.2	0.89879E 04
	7	1422.	111.7	0.3730	0.0820	57.9	0.82977E 04
	8	1615.	93.1	0.4479	0.0906	74.6	0.11122E 05
	9	1766.	78.5	0.5315	0.0945	80.2	0.12187E 05
	10	2002.	55.8	0.7504	0.1111	118.6	0.19685E 05
B	1	430.	207.5	0.2005	0.0886	73.3	0.10828E 05
	2	586.	192.4	0.2162	0.0934	82.0	0.12386E 05
	3	857.	166.2	0.2503	0.1000	92.5	0.14465E 05
	4	1118.	141.1	0.2951	0.1056	99.2	0.15971E 05
	5	1388.	115.0	0.3623	0.1131	117.3	0.19691E 05
	6	1500.	104.2	0.4000	0.1208	132.0	0.23190E 05
	7	1508.	103.4	0.4030	0.1182	122.8	0.21239E 05
	8	1577.	96.8	0.4309	0.1227	140.0	0.24854E 05
	9	1771.	78.0	0.5348	0.1317	149.6	0.28094E 05
	10	1848.	70.6	0.5915	0.1362	170.7	0.32967E 05
C	1	357.	214.5	0.1939	0.1126	111.5	0.18660E 05
	2	593.	191.7	0.2169	0.1149	128.5	0.21794E 05
	3	833.	168.6	0.2468	0.1165	115.5	0.19769E 05
	4	1069.	145.8	0.2855	0.1251	150.8	0.27179E 05
	5	1186.	134.5	0.3096	0.1250	143.7	0.25880E 05
	6	1379.	115.9	0.3595	0.1330	162.7	0.30806E 05
	7	1422.	111.7	0.3730	0.1302	161.0	0.29954E 05
	8	1615.	93.1	0.4479	0.1310	177.4	0.33172E 05
	9	1766.	78.5	0.5315	0.1299	178.2	0.33092E 05
	10	2002.	55.8	0.7504	0.1173	156.0	0.26837E 05
D	1	357.	214.5	0.1939	0.1184	128.5	0.22243E 05
	2	593.	191.7	0.2169	0.1212	143.8	0.25318E 05
	3	833.	168.6	0.2468	0.1227	128.5	0.22812E 05
	4	1069.	145.8	0.2855	0.1253	148.9	0.26857E 05
	5	1186.	134.5	0.3096	0.1245	143.5	0.25763E 05
	6	1379.	115.9	0.3595			
	7	1422.	111.7	0.3730	0.1239	154.1	0.27568E 05
	8	1615.	93.1	0.4479			
	9	1766.	78.5	0.5315	0.1111	122.0	0.20246E 05
	10	2002.	55.8	0.7504	0.1100	118.0	0.19463E 05

TABLE II (continued)

Wave frequency  $f = 0.66$  hz, Depth  $D = 187$  cm.

Station		Paddle Distance x(cm)	Channel Width w(cm)	Growth Rate G	Steep- ness H/L	Potential Energy Density E <sub>p</sub> (cm <sup>2</sup> )	Potential Energy Flux F(cm <sup>3</sup> /sec)
E	1	586.	192.4	0.2162	0.1213	140.7	0.24778E 05
	2	688.	182.6	0.2279	0.1150	105.0	0.17821E 05
	3	857.	166.2	0.2503	0.1235	138.2	0.24669E 05
	4	959.	156.4	0.2661	0.1258	146.1	0.26434E 05
	1 5	1118.	141.1	0.2951	0.1272	146.5	0.26746E 05
	2 6	1388.	115.0	0.3623	0.1299	152.9	0.28384E 05
F	1	357.	214.5	0.1939	0.1208	132.7	0.23304E 05
	2	593.	191.7	0.2169	0.1233	145.7	0.25977E 05
	1 3	833.	168.6	0.2468	0.1227	132.2	0.23478E 05
	2 4	1069.	145.8	0.2855	0.1243	145.6	0.26123E 05
	5	1186.	134.5	0.3096	0.1198	139.5	0.24352E 05
	6	1379.	115.9	0.3595	0.1222	133.0	0.23545E 05
	7	1422.	111.7	0.3730	0.1118	123.7	0.20614E 05
	8	1615.	93.1	0.4479	0.1154	124.0	0.21096E 05
	9	1766.	78.5	0.5315	0.1106	114.2	0.18907E 05
	10	2002.	55.8	0.7504	0.1088	110.9	0.18177E 05
G	1	357.	214.5	0.1939	0.1240	140.0	0.25064E 05
	2 1	593.	191.7	0.2169	0.1241	149.4	0.26764E 05
	3	833.	168.6	0.2468	0.1096	115.2	0.18966E 05
	4	1069.	145.8	0.2855	0.1124	122.3	0.20456E 05
	5	1186.	134.5	0.3096	0.1231	141.7	0.25235E 05
	6	1379.	115.9	0.3595	0.1004	96.5	0.15104E 05
	7	1422.	111.7	0.3730	0.1085	115.4	0.18874E 05
	8	1615.	93.1	0.4479	0.1040	100.6	0.16064E 05
	9	1766.	78.5	0.5315	0.1071	106.2	0.17242E 05
	10	2002.	55.8	0.7504	0.1148	125.4	0.21269E 05



TABLE II (continued)

Wave frequency  $f = 0.73$  hz, Depth  $D = 154$  cm.

Station		Paddle Distance x(cm)	Channel Width w(cm)	Growth Rate G	Steep- ness H/L	Potential Energy Density E <sub>p</sub> (cm <sup>2</sup> )	Potential Energy Flux F(cm <sup>3</sup> /sec)
A	1	517.	199.1	0.1708	0.0601	20.7	0.24634E 04
	2	753.	176.3	0.1929	0.0641	23.8	0.28756E 04
	3	914.	160.7	0.2116	0.0714	29.0	0.35890E 04
	4	1094.	143.4	0.2373	0.0736	31.0	0.38706E 04
	5	1180.	135.1	0.2520	0.0772	34.7	0.44046E 04
	6	1330.	120.6	0.2823	0.0800	36.7	0.47218E 04
	7	1428.	111.1	0.3064	0.0800	38.7	0.49725E 04
	8	1561.	98.3	0.3466			
	9	1664.	88.4	0.3858	0.0853	44.3	0.58289E 04
	10	1797.	75.5	0.4518	0.0888	47.9	0.64063E 04
B	1	517.	199.1	0.1708	0.1029	63.7	0.91453E 04
	2	753.	176.3	0.1929	0.1085	79.9	0.11824E 05
	3	914.	160.7	0.2116	0.1152	75.7	0.11637E 05
	4	1094.	143.4	0.2373	0.1234	98.0	0.15797E 05
	5	1180.	135.1	0.2520	0.1273	99.5	0.16428E 05
	6	1330.	120.6	0.2823	0.1268	99.5	0.16391E 05
	7	1428.	111.1	0.3064	0.1217	93.5	0.14917E 05
	8	1561.	98.3	0.3466			
	2 9	1664.	88.4	0.3858	0.1278	108.1	0.17916E 05
	10	1797.	75.5	0.4518	0.1239	107.2	0.17351E 05
C	1	517.	199.1	0.1708	0.1042	69.2	0.10002E 05
	2	753.	176.3	0.1929	0.1131	83.6	0.12695E 05
	3	914.	160.7	0.2116	0.1152	78.2	0.12021E 05
	2 4	1094.	143.4	0.2373	0.1300	111.2	0.18683E 05
	5	1180.	135.1	0.2520	0.1295	86.0	0.14394E 05
	6	1330.	120.6	0.2823	0.1284	102.4	0.17026E 05
	7	1428.	111.1	0.3064	0.1262	98.5	0.16152E 05
	8	1561.	98.3	0.3466	0.1295	109.5	0.18327E 05
	9	1664.	88.4	0.3858	0.1245	100.6	0.16345E 05
	10	1797.	75.5	0.4518	0.1202	99.1	0.15672E 05

TABLE II (continued)

Wave frequency  $f = 0.73$  hz, Depth  $D = 154$  cm.

Station	Paddle Distance $x(\text{cm})$	Channel Width $w(\text{cm})$	Growth Rate $G$	Steepness $H/L$	Potential Energy Density $E_p(\text{cm}^2)$	Potential Energy Flux $F(\text{cm}^3/\text{sec})$
D	1	517.	199.1	0.1708	0.1116	79.0
	2	753.	176.3	0.1929	0.1242	93.9
	3	914.	160.7	0.2116	0.1158	84.2
	4	1094.	143.4	0.2373	0.1278	107.5
	5	1180.	135.1	0.2520	0.1338	116.7
	6	1330.	120.6	0.2823	0.1306	112.2
	7	1428.	111.1	0.3064	0.1300	111.0
	8	1561.	98.3	0.3466	0.1170	95.0
	9	1664.	88.4	0.3858	0.1187	93.1
	10	1797.	75.5	0.4518	0.1111	82.1
E	1	517.	199.1	0.1708	0.1188	82.5
	2	753.	176.3	0.1929	0.1231	92.5
	3	914.	160.7	0.2116	0.1158	80.5
	4	1094.	143.4	0.2373	0.1234	99.5
	5	1180.	135.1	0.2520	0.1256	109.5
	6	1330.	120.6	0.2823	0.1186	92.4
	7	1428.	111.1	0.3064	0.1134	80.5
	8	1561.	98.3	0.3466	0.1122	83.0
	9	1664.	88.4	0.3858	0.1101	77.7
	10	1797.	75.5	0.4518	0.1093	75.8

TABLE II (continued)

Wave frequency  $f = 0.80$  hz, Depth  $D = 132$  cm.

Station		Paddle Distance x(cm)	Channel Width w(cm)	Growth Rate G	Steep- ness H/L	Potential Energy Density E <sub>p</sub> (cm <sup>2</sup> )	Potential Energy Flux F(cm <sup>3</sup> /sec)
A	1	804.	171.4	0.1652	0.0675	18.7	0.20864E 04
	2	1040.	148.6	0.1906	0.0702	20.4	0.23020E 04
	3	1056.	147.0	0.1927	0.0738	22.7	0.25741E 04
	4	1292.	124.3	0.2281	0.0797	29.3	0.34325E 04
	5	1532.	101.1	0.2806	0.0857	32.0	0.38440E 04
	6	1675.	87.3	0.3252	0.0915	35.5	0.43825E 04
	7	1768.	78.3	0.3626	0.0958	39.9	0.50338E 04
	8	1911.	64.5	0.4407	0.1042	46.8	0.61802E 04
B	1	804.	171.4	0.1652	0.1070	49.5	0.66252E 04
	2	1040.	148.6	0.1906	0.1072	50.2	0.67276E 04
	3	1056.	147.0	0.1927	0.1085	52.5	0.70847E 04
	4	1292.	124.3	0.2281	0.1204	66.0	0.95468E 04
	5	1532.	101.1	0.2806	0.1327	79.7	0.12428E 05
	6	1675.	87.3	0.3252	0.1307	76.2	0.11738E 05
	7	1768.	78.3	0.3626	0.1334	77.7	0.12175E 05
	8	1911.	64.5	0.4407	0.1305	79.3	0.12188E 05
C	1	804.	171.4	0.1652	0.1144	59.0	0.82289E 04
	2	1040.	148.6	0.1906	0.1128	56.2	0.77817E 04
	3	1056.	147.0	0.1927	0.1136	55.2	0.76741E 04
	4	1292.	124.3	0.2281	0.1281	77.5	0.11746E 05
	5	1532.	101.1	0.2806	0.1365	85.7	0.13692E 05
	6	1675.	87.3	0.3252	0.1307	73.0	0.11238E 05
	7	1768.	78.3	0.3626	0.1271	70.0	0.10536E 05
	8	1911.	64.5	0.4407	0.1226	72.2	0.10580E 05
D	1	804.	171.4	0.1652	0.1172	61.5	0.87205E 04
	2	1040.	148.6	0.1906	0.1181	61.8	0.88184E 04
	3	1056.	147.0	0.1927	0.1234	67.2	0.98966E 04
	4	1292.	124.3	0.2281	0.1301	82.1	0.12594E 05
	5	1532.	101.1	0.2806	0.1281	72.0	0.10904E 05
	6	1675.	87.3	0.3252	0.1144	60.0	0.83683E 04
	7	1768.	78.3	0.3626	0.1190	64.2	0.92124E 04
	8	1911.	64.5	0.4407	0.1076	51.5	0.69196E 04

### 5.1.1 Wave Propagation Speed

The determination of wavelength, steepness, and energy flux, as well as the conversion of time- to space-scales, all require a suitable definition of the instantaneous speed of moving waves. For steady, irrotational waves of finite height, the Stokes surface profiles to any order are symmetric about their crests. All points of constant phase (crests or troughs, say) move at the same speed (phase velocity,  $C$ ), experimentally determinable by observing the transit times of individual phases over a known distance. Alternatively, where the dispersion relation,  $C = f(H,T)$ , is known analytically,  $C$  can be determined from measurements of wave height,  $H$ , and period,  $T$ . The latter is ordinarily taken as the reciprocal of the paddle frequency,  $f$ . For Stokes waves of 3rd and 5th order, respectively, phase velocity is given implicitly by:

$$C_3 = \frac{g}{2\pi f} \left[ 1 + \left( \frac{\pi f H}{C_3} \right)^2 \right] \quad (\text{Levi-Civita, 1925}) \quad (2a)$$

$$C_5 = \frac{g}{2\pi f} \left[ 1 + \left( \frac{\pi f H}{C_5} \right)^2 + \left( \frac{\pi f H}{C_5} \right)^4 \right] \quad (\text{Beach Erosion Board, 1941}) \quad (2b)$$

In the present experiments, however, all waves within the convergent channel were unsteady, and their profiles became increasingly asymmetric as their height increased towards breaking. The degree to which their instantaneous speeds fit the above steady-state models was investigated by two independent methods:

- o crest speeds were determined by timing the arrivals of corresponding elevation maxima at two tandem wave staffs less than a wavelength apart;
- o phase speeds, defined as the velocity of wave spectral components associated with the paddle frequency,  $f$ , were calculated as follows.

Simultaneous, 25-second, surface elevation series from two tandem wave staffs were Fourier-analyzed, and their cross-spectra (Jenkins and Watts, 1968) were averaged over triplicate wave series. Phase speed was then determined from the relation,  $C = 2\pi f \Delta x / \phi$ , where  $\Delta x$  was the staff spacing, and  $\phi$  the phase of the cross spectrum at frequency,  $f$ . This latter method had the advantage of demonstrating that the paddle-generated waves were essentially free from energy peaks at frequencies other than  $f$  and its higher harmonics (App. B).

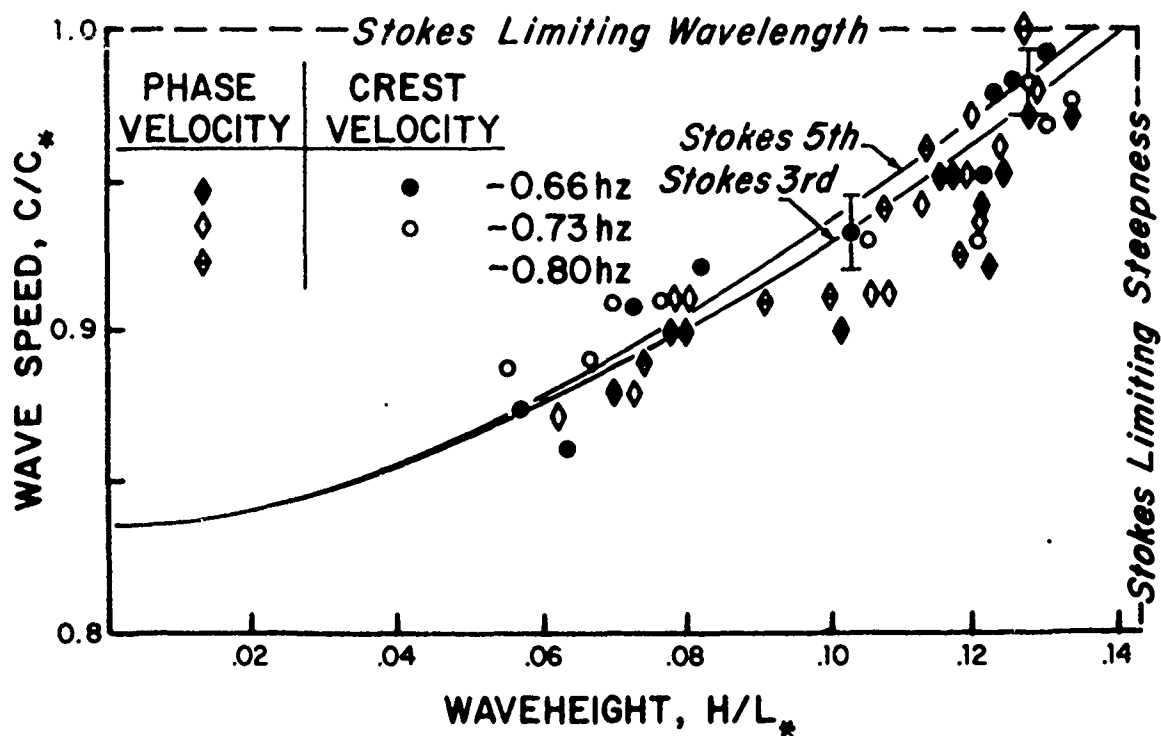


Fig. 7 Influence of wave height on wave speed. Note that experimental crest speeds agree within 3% with Stokes 5th order curve. Coordinates are normalized to Michell's limiting values:  $L_* = C_*T = 1.2g/2\pi f^2$ .

Figure 7 compares representative values of phase and crest speeds so obtained<sup>1</sup> for thirty different wave heights, divided among three paddle frequencies, with curves computed from equations 2a and 2b, from which the following conclusions were drawn

- o The scatter of phase speed was somewhat greater than that for crest speeds, although nowhere greater than  $\pm 3\%$  about the median speed for a particular wave height. This result is somewhat surprising. One might expect that phase speed would be more representative of wave propagation because spectra indicate that over 70% of wave energy is concentrated in a band 0.04 hz wide, centered on the paddle frequency, whereas the crest is a point on a wave whose position can fluctuate due to small disturbances.
- o The locus of crest speeds is closer to the 5th-order Stokes curve than to the 3rd-order curve, although these curves differ by only 1% at the Stokes (Michell) steepness limit,  $H_*/L_* = 0.142$ . Owing to the nature of the power expansions on which these curves are based, neither passes precisely through the limit phase speed at limiting steepness. However, the locus of phase speeds (not formally determined) does appear to pass through this point, and lies consistently below that for crest speeds. This is consistent with the premise that crest speeds should progressively exceed phase speeds in growing waves, and that the latter should better agree with a proper theory.

However, because the overall error is small in any case, and because the 5th order theory gives the best approximation to observed crest speeds, it is used hereinafter for the calculation of phase velocity and wavelength up to breaking. It is also used, where necessary, after breaking, although its applicability is not established because of the uncertainty of determining crest arrivals.

To determine whether the scatter of phase speeds in Fig. 7 might be due, in part, to finite growth rate, the influence of frequency and steepness was removed by normalization with respect to the 5th-order phase velocity,  $C_5$ , and the results plotted vs growth rate in Fig. 8. The lack of any apparent trend implies a negligible influence of  $G$ , compared to that of frequency or steepness.

---

<sup>1</sup>The abscissa for each datum is an average over the first four waves of triplicated series. Crest speed ordinates are averages over about 45 consecutive waves. The two representative error bars denote 84% confidence limits from an assumed Gaussian distribution of variances in arrival times.

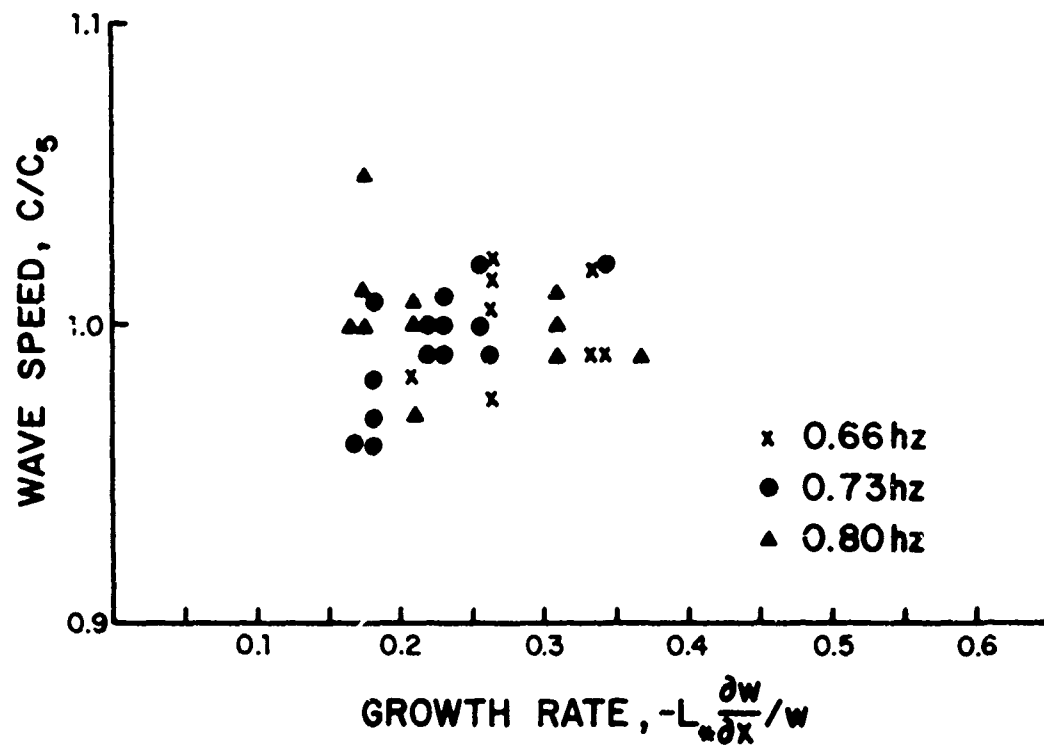


Fig. 8 Influence of growth rate upon wave speed.

### 5.1.2 Steepness-Growth Rate Diagram

It was earlier remarked (Section 4) that, while breaking appeared to be governed by some limiting steepness, breaking intensity was qualitatively linked to growth rate. These relationships can be quantified by plotting  $H/L$  vs  $G$  for individual waves, since any point on such a diagram defines the immediate state of a wave, and a sequence of such points determines a trajectory that gives the wave's steepness history as it grows toward breaking.

Figure 9 shows two representative histories for light and heavily breaking 0.66 hz waves, corresponding to data series E and B in Table II, respectively.<sup>1</sup> Error bars indicate the steepness uncertainty attendant to data averaging. Each trajectory commences at the left at some initial steepness determined by paddle stroke amplitude, and slopes upward to the right as the wave(s) converge towards breaking, as identified by the numbers 1 or 2 previously defined. In this representation, light breaking is evidently distinguished from heavy breaking by a higher, initial steepness, and by a lower growth rate at breaking. Visually, the difference in breaking intensity is obvious (Figs. 5 & 6), and is later shown to depend directly upon growth rate (Section 5.7.1). The fact that both curves appear not to have reached maximum steepness at breaking may, in part, be due to the difficulty of determining steepness accurately after breaking. But it also can be qualitatively argued that breaking within a uniform convergence represents some sort of equilibrium between energy supplied by lateral squeezing and that lost by breaking, and that wave height- and hence steepness- may actually increase slightly beyond the breaking point (see Section 5.7.2).

### 5.1.3 Breaking Steepness

The two curves in Fig. 9 are only representative examples of an infinite set, whose initial steepnesses range from zero to the theoretical limiting value, 0.142, and whose maxima are bounded by this limit, or by

---

<sup>1</sup> Letter-number symbols in this figure identify wave states later discussed in other context.



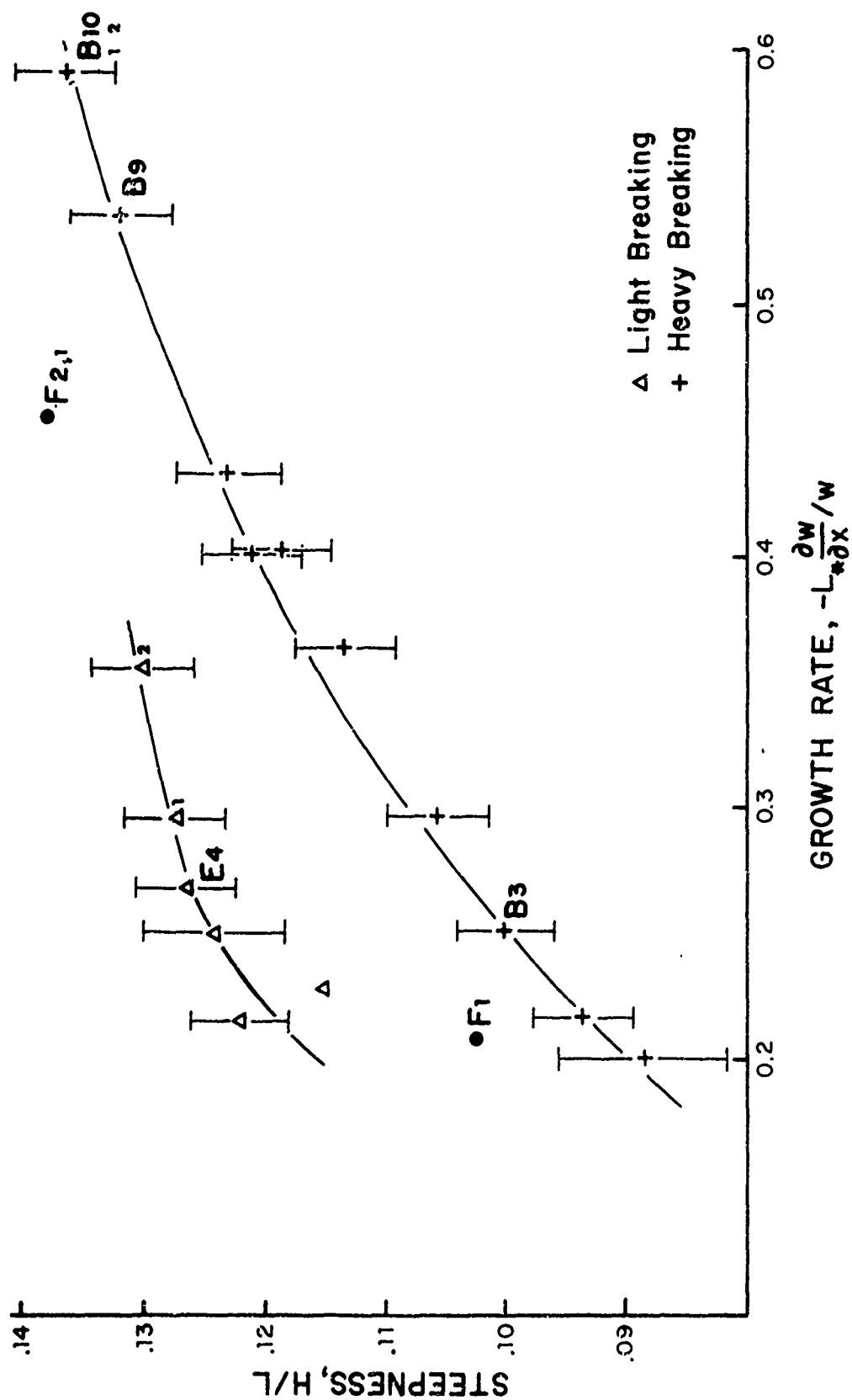


Fig. 9 Typical steepness-growth rate trajectories for light and heavy breaking 0.66 hz waves.

some empirical lower bound. To better define this latter bound, Fig. 10 shows the maximum (breaking) steepnesses for all wave series in Table II plotted against growth rate. Despite the large error bars, which are the result of expanding the steepness scale within the breaking range, there appears to be a significant tendency for breaking steepness to increase with growth rate. This is opposite to the expectation that those waves which grow slowest should achieve maximum steepness-possibly approaching the theoretical limit (0.142) for infinitely slow growth. The converse result implies some steepness moderating factor near breaking that is only transcended by rapid growth. A possible explanation is that steep waves are weakly dissipative before breaking because of strong velocity gradients beneath their crests (Section 5.4.2), and would never achieve limiting steady-state steepness however small their growth rates. If breaking energy loss is a monotonically increasing function of steepness, equilibrium breaking steepness should increase with growth rate, as observed. This point is further elaborated in Section 5.6.

## 5.2 Stationarity in Growing Waves

Most of the operational data in these experiments were obtained from time-series records made at fixed stations. A mathematically more-tractable representation of wave properties, that can be compared to steady wave theory, is one referred to as stationary spatial coordinate system. A measure of stationarity is the accuracy with which a stationary time series can be equated to synoptic observations at an instant. This question was examined here by comparing staff records of surface elevation to simultaneous motion pictures of steep ( $H/L = 0.136$ ), breaking, 0.66 hz waves at high growth rate ( $G = 0.54$ ). These conditions represent the most rapid changes observed, and thus the most critical test of stationarity.

Figure 11 compares three different superimposed profiles of the same wave. The solid line is the true space profile, reconstructed from a single-frame photograph at the instant when the moving wave was most nearly centered on the wave staff. The abscissa of the frame-by-frame and wave staff records were obtained by multiplying corresponding phase arrival time increments by the Stokes 2<sup>nd</sup> order phase velocity,  $C_5$  (Eq. 2b). Except on

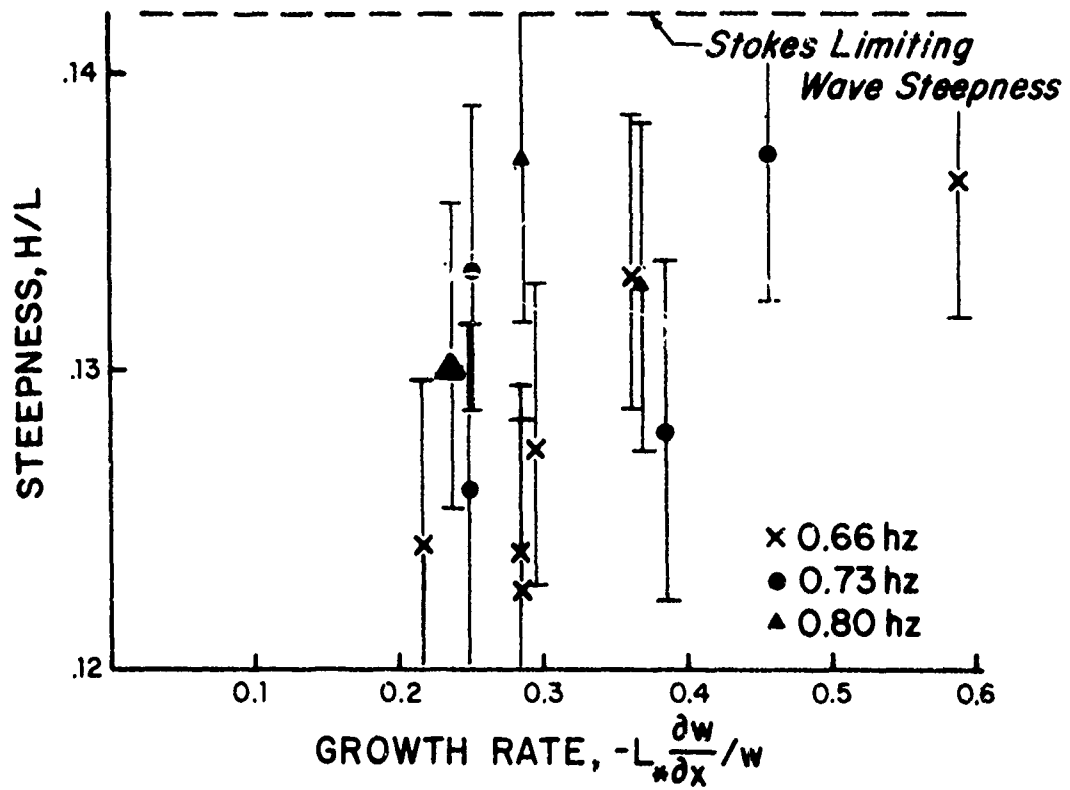


Fig. 10 Influence of growth rate upon breaking steepness.

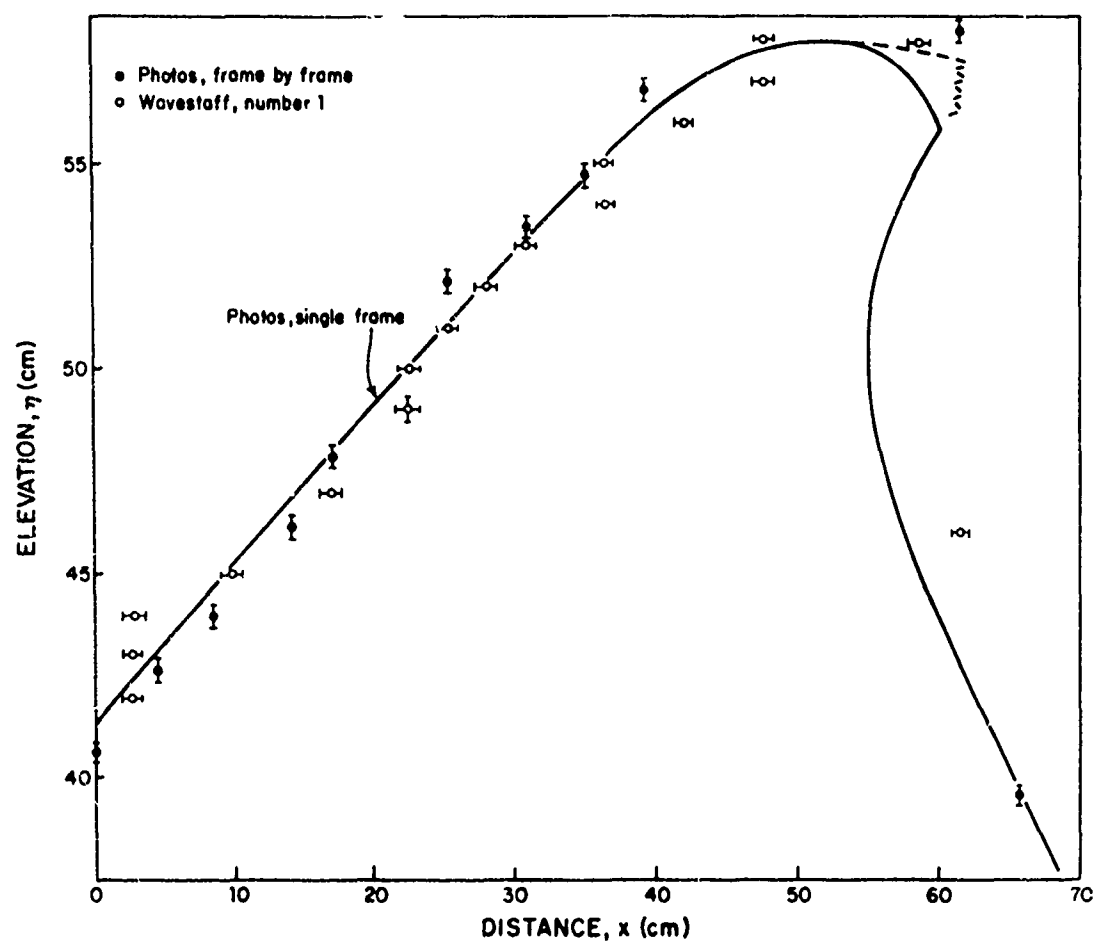


Fig. 11 Comparison of wave profiles obtained by simultaneous wave staff records and sidewall photography.

the overhanging crest face, where the wave staff indicated a near-vertical rise, all three profiles agree within 1.5 cm (2% of  $C_5 \Delta t$ ). This comparison also served to verify the accuracy of wave staff response and resolution.

### 5.3 Scaling and Similitude

In order to compare or contrast flow fields and surface profiles of different waves it is necessary to know if they are dynamically similar. This requires the following conditions be satisfied (Duncan, et al., 1960, pp. 178-185)

- o Corresponding space-time positions are related by constant linear scale factors,  $x_1/d_1 = x_2/d_2$ ,  $y_1/d_1 = y_2/d_2$ ,  $z_1/d_1 = z_2/d_2$ , and  $t_1 e_1 = t_2 e_2$ .
- o All relevant physical properties and locations of the boundaries must be distributed at corresponding positions.
- o Forces or scalar quantities at corresponding positions can be related by constant linear scale factors.

For all frequencies in these experiments the dominant forces were gravitational and inertial, and it was convenient to let  $d = L_*$  and  $e = f$  be linear space and time scales respectively.<sup>1</sup> The second condition requires  $w(x)/L_* = \text{constant}$ ,  $\partial w / \partial x = \text{constant}$ , and  $D/L_* = \text{constant}$ , as was the case in this study.<sup>2</sup> The third condition is a corollary of the constancy of Froude number,  $C^2/L_* g$  (ibid, p. 182). It was shown (Section 5.1.1) that  $C$ , the wave propagation speed, can be expressed as the product of a function of steepness,  $F(H/L)$ , and  $(g/2\pi f)$ , where  $L = C/f$ . Recalling that  $L_* = 1.2g/2\pi f^2$ , it is clear that the Froude number is proportional to  $F(H/L)$ , so that steepness,  $H/L$ , must also be constant for dynamical similitude. For the frequencies used in this study, the nominal values of the constant scale factors are:

<sup>1</sup>This choice of scaling parameters had the advantage that when the waves were breaking,  $C/C_* = L/L_* = 1$ .

<sup>2</sup>This is equivalent to growth rate,  $G = -L_*(\partial w / \partial x) / w(x) = \text{constant}$ .

Frequency f (hz)	Length L* (cm)	Speed C* (cm/sec)	Energy $g_0 L_*^2 \times 10^{-8}$ (ergs/cm <sup>2</sup> )
0.66	430	284	1.82
0.73	352	257	1.22
0.80	293	234	0.84

In summary, with space and time scale factors,  $L_*$  and  $f$ , respectively it is sufficient to maintain constant growth rate,  $-L_* \partial w / \partial x / w(x)$ , and steepness,  $H/L$ , in order to achieve dynamical similitude.

#### 5.4 Results of Flow Velocity Measurements

The measurement of internal flow velocities in growing waves was one of the principal objectives of these experiments, not only because they comprise the most sensitive test of any theory, but also because they permit some insight of the breaking process, for which there presently is no adequate theory. As described in Section 3.3, flow measurements were confined to velocities having components in the direction of wave propagation, to accuracies of order:

Range cm/sec	Magnitude cm/sec	Direction
30<U<65	±6	4°
65<U<550	3%	2°

Flow velocities are discussed here in two different contexts. In section 5.4.1, profiles of maximum horizontal velocity vs elevation beneath individual wave crests are compared to those computed for steady waves of corresponding steepness from Stokes higher-order theory. This representation serves to maximize the discrepancy between theory and observation as unsteady waves grow towards breaking, and to emphasize the influence of growth rate on breaking intensity. Section 5.4.2 represents the internal velocity fields in growing waves in the form of isolines (contours) of constant velocity in space-time coordinates, upon which are superimposed direction arrows and measured wave profiles. Such plots graphically illustrate how increasing steepness and profile asymmetry are reflected

internally by distortion of the velocity field in a manner not predictable for steady waves.

#### 5.4 , Profiles of Horizontal Velocity

Although detailed measurements of internal flow velocities were conducted at over forty stations, six exemplary profiles of maximum horizontal velocity suffice to illustrate without redundancy the principal features of wave development as functions of frequency, steepness, and growth rate. These six stations are identified by letter-number symbols in the steepness-growth rate diagram (Fig. 9), and relevant wave parameters are listed in Table I.

If steady wave theory has any application to unsteady waves, it should best apply to (young) waves of low steepness and growth rate. For these conditions, Fig. 12 shows plots of the vertical distribution of maximum horizontal velocity for the first four uniform waves in heavy-breaking series B-3 and F-1, at frequencies, 0.66 and 0.73 hz, respectively. Also plotted are other data for waves of similar steepness, but higher frequency (1.15 hz), reported by Morison and Crooke (1953).<sup>1</sup> The solid curves in this figure were computed from Stokes 5th-order theory (Skjelbreia and Hendrickson, 1960), using appropriate water depths and steepnesses. In this- and the two succeeding- figures, measurement elevations and flow velocities have been normalized to the Stokes limiting wavelengths and phase velocities, respectively. For constant steepness, this Froude scaling should eliminate the influence of frequency, except in so far as it affects growth rate; that is, profile differences should be functions only of growth rate.

As an engineering approximation, the computed curves might be regarded as a reasonable upper bound to the observed data, but there are consistent differences that exceed the above-stated measurement accuracy. The fit is acceptable near the crests and well below trough level, but the velocities observed here are uniformly low in the mid-range by about 25-30% (12-15 cm/sec), and their vertical distribution is more hyperbolic than exponential,

---

<sup>1</sup> Morison and Crooke computed velocities from photographs of neutral-density oil droplets. Because of slightly lower steepness (0.086 vs 0.10), their normalized wave height range was about 14% smaller, as indicated by the dashed lines in Fig. 11.

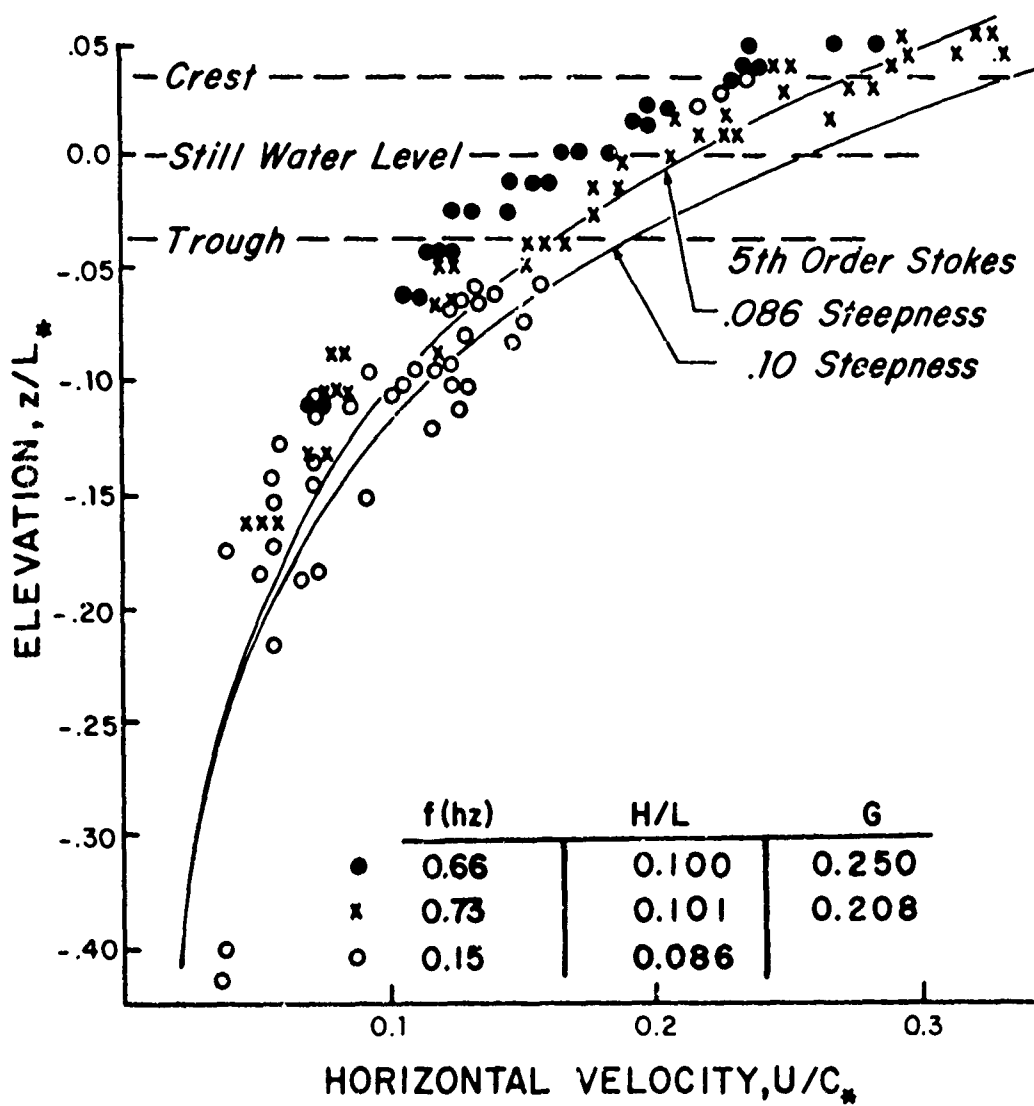


Fig. 12 Maximum horizontal flow velocities within low steepness waves. Open circles represent data from Morison and Crooke (1953).



as predicted by the Stokes curves. As shown below, this tendency increases with steepness. Secondly, the growth rate is about 25% higher for the 0.66 hz waves than for the 0.73 hz waves, whereas the measured velocities are slightly lower-particularly in mid-range. This result is opposite to that observed at higher steepnesses, but the difference is within measurement error, and could have resulted from the somewhat arbitrary choice of the probe response exponent,  $n_a$ , in the low-velocity range (App. A). Similar differences between the present data and those of Morison and Crooke are inexplicable, except to note that they are opposite to what would be expected for waves of smaller steepness and (presumably) zero growth rate.

But these comparisons are pushing the threshold accuracy of the experiments, and the principal conclusion is that flow velocity in waves of steepness  $< 0.1$  are predicted acceptably by Stokes 5th-order theory.

Figure 13 is a similar plot for pre-breaking waves of the same frequency and nearly the same steepness (series E-4 and B-9, Fig. 9 and Table I). The comparison here is the difference between the velocity profiles within lightly- and heavily-breaking waves near terminal growth, as manifested by a large difference in growth rate,  $G$ . Stokes 5th-order curves for both steepnesses are given, together with that for limiting steepness ( $H_*/L_* = 0.142$ ), computed from expansion coefficients given by Michell (1893).

Again, both data distributions are in substantial agreement below trough level, but increasingly diverge upward. Near-crest velocities within waves destined to break heavily (high growth rate) exceed those for light breaking by as much as 40%. Neither distribution much resembles any of the computed curves, all velocities being generally lower until just beneath crest height, and then increasing hyperbolically so as to exceed even those predicted by the limiting wave profile. Thus, for waves of similar near-breaking steepness, the influence of increasing growth rate is to markedly increase the vertical gradient of maximum horizontal velocity and, as later shown, to correspondingly increase breaking intensity.

Lastly, Fig. 14 compares observed profiles for two heavily breaking waves of the same steepness, but different frequency (series B-10 and F-2, respectively, Fig. 9), to the Stokes limiting wave profile. The close

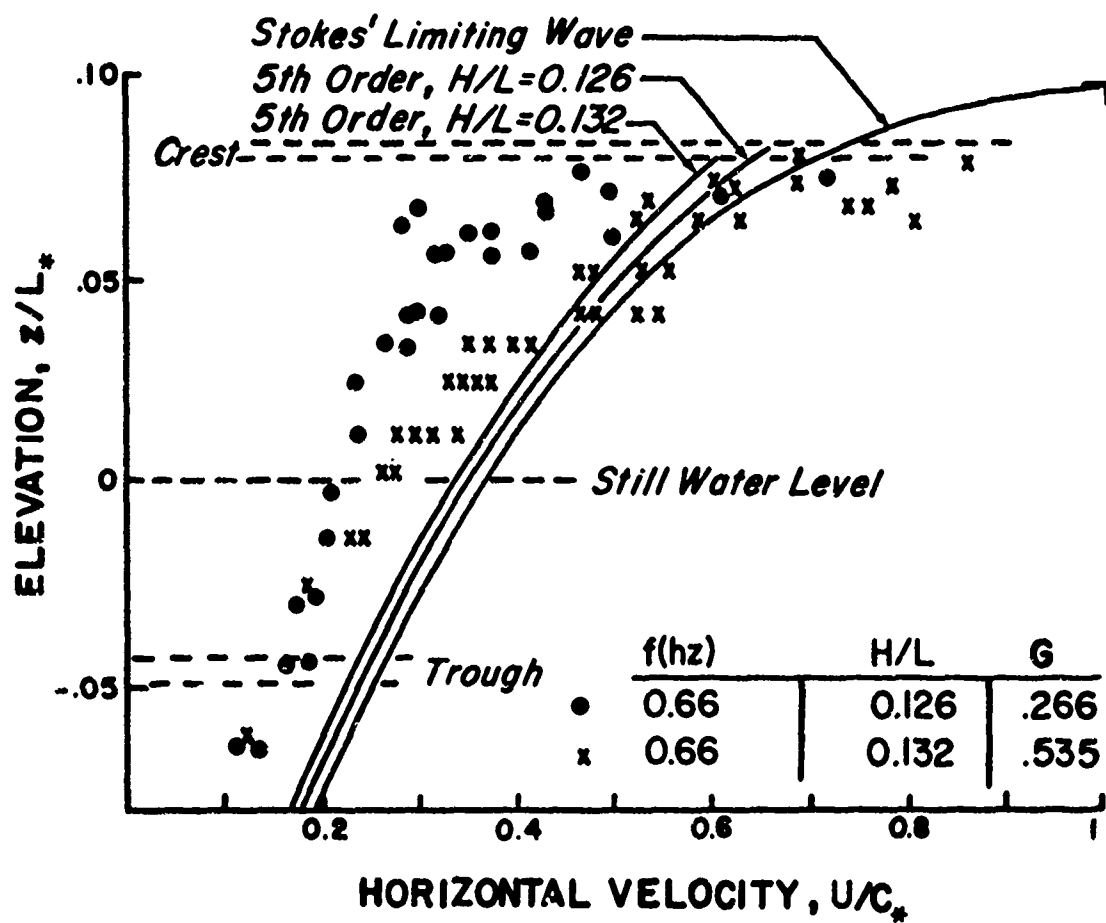


Fig. 13 Comparison of maximum horizontal flow velocities at low (o) and high (x) growth rates near breaking.

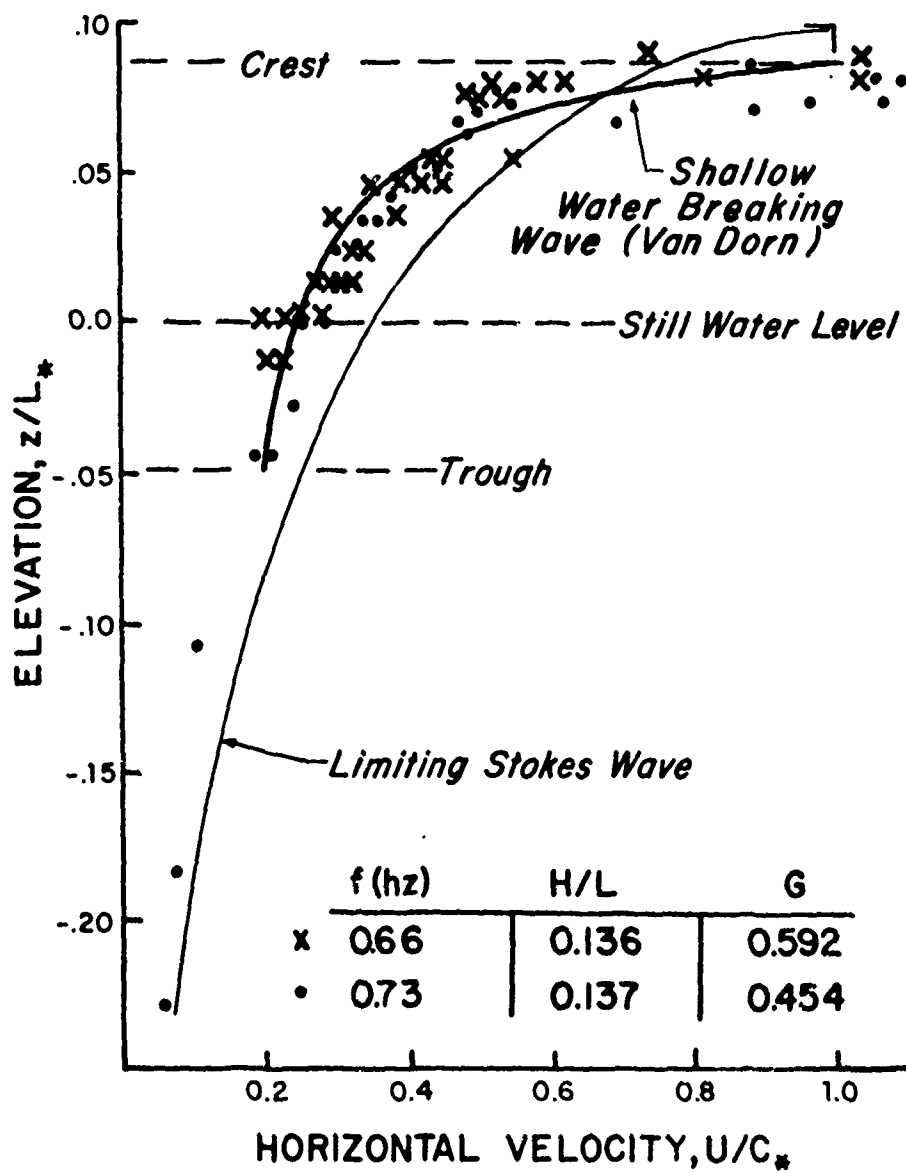


Fig. 14 Maximum horizontal flow velocities within a 0.66 hz heavily breaking wave.

data correspondence between frequencies again supports Froude similitude-- even at breaking. Crest flow velocities slightly exceed the limiting phase velocity,  $C_*$ , although theoretical limiting steepness is never quite achieved. If the 25% higher growth rate of 0.66 hz waves has any influence on velocity distribution, it is to slightly lower the elevation at which maximum velocity occurs. This feature is further discussed in the next section.

Although the observed velocity distributions deviate markedly from the computed limiting Stokes profile, they appear to correspond quite closely to those observed by Van Dorn (1975) within shallow-water waves breaking on gentle slopes. Irrespective of frequency, he found that the ratio of maximum horizontal velocity,  $U$ , to observed phase velocity,  $C$ , was given by the hyperbolic equation:

$$U/C = aZ/(b - Z) + U_0/C, \quad (3)$$

where  $Z = Y/Y_m$  was the fractional ordinate (bottom to crest) at which  $U$  was measured,  $a = 0.10$  and  $b = 1.125$  are arbitrary constants, and  $U_0/C = 0.20$  at the bottom. In Fig. 14,  $U/C = 0.20$ , approximately, at trough elevation,  $z_t$ , for which the appropriate normalization, referred to still water level, requires that  $Z = (z - z_t)/H$ . The heavy curve in Fig. 13 was computed from Eq. (3), using the same coefficients. Although its extrapolation below trough level is obviously unwarranted, the fit above this level suggests that the breaking of deep and shallow waves have marked dynamical similarities.

#### 5.4.2 Internal Velocity Fields

Although over 600,000 independent determinations of fluid velocity and direction were obtained in the course of these experiments, a substantial fraction comprised redundant repetitions to insure accuracy. It was also found that, while discrete data were highly reproducible at all points within individual waves of repetitive and quasi-uniform series, the details of the velocity distributions near the crests of steep waves varied just enough from wave to wave so as to obscure the fine structure which it was desirable to resolve. This result proscribed near-crest, wave-to-wave averaging of velocity data in the same manner as employed for wave height or steepness. The fact that individual flow representations of the type

described below looked very much alike from wave to wave argues that the above differences are attributable to slight phase shifts, rather than to timing errors. At depths greater than about 22 cm beneath steep crests, flow details were sufficiently similar so as to permit meaningful averages. Accordingly, the few examples included here were selected from a very large body of data as typically illustrative of the instantaneous velocity fields at principal stages of wave growth.

All velocity fields were generated from computer print-outs in which flow velocity magnitudes were displayed as numbers, vertically arrayed in proportion to scaled measurement elevation, and horizontally according to synchronized time sequence. Horizontal number spacing was scaled according to phase velocity so that the array corresponded to an undistorted x-z field at the instant of crest passage. Flow directions were indicated by a computer-generated arrow between each pair of numbers. Smoothed contour lines of constant velocity were then drawn by eye across each array. For elevations lower than 22 cm beneath a wave crest, arrays for the first four uniform waves in a series were superimposed to better define average flow; above this level only that array having the highest velocities was contoured. Each plot was bounded upwardly by the corresponding synchronized surface elevation record from staff data. Considering that each array spanned only about  $120^\circ$  of wave phase and comprised upwards of 3,000 data points, it is felt that even the fairly-complicated flow detailing portrayed at breaking is an accurate representation. Accuracy was considered lowest where flow directions were inclined more than  $45^\circ$ , so as to produce backflow on either probe tip, although the directional calibrations were still consistent and reproducible. These areas are indicated by shading in the following figures.

Figures 15, 16, and 17 show velocity fields so constructed for young, pre-breaking, and breaking stages of a heavily-breaking 0.66 hz wave, corresponding to data series B-3, B-9, and B-10, respectively, in Fig. 9 and Table I. The profile of the young wave is fairly symmetric about its crest, as are its internal flow directions and velocity contours. The latter are widely spaced and convex upward. As shown in Fig. 12, even maximum horizontal velocities are close to those computed from Stokes 5th-order theory, and a velocity field, so computed, would undoubtedly look very similar to Fig. 15.

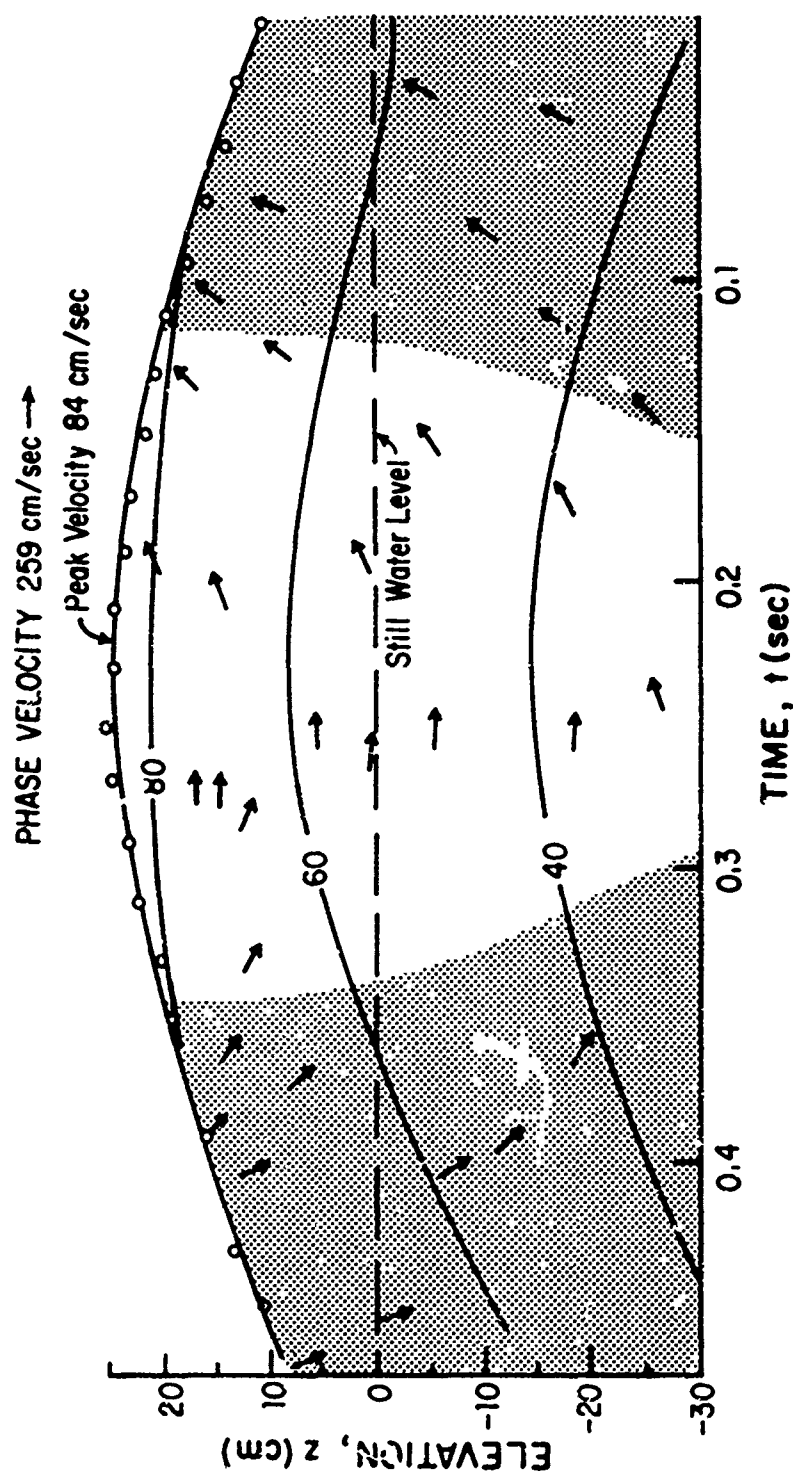


Fig. 15 Velocity field within heavily breaking 0.66 Hz wave at early growth stage (point B-3, Fig. 9).

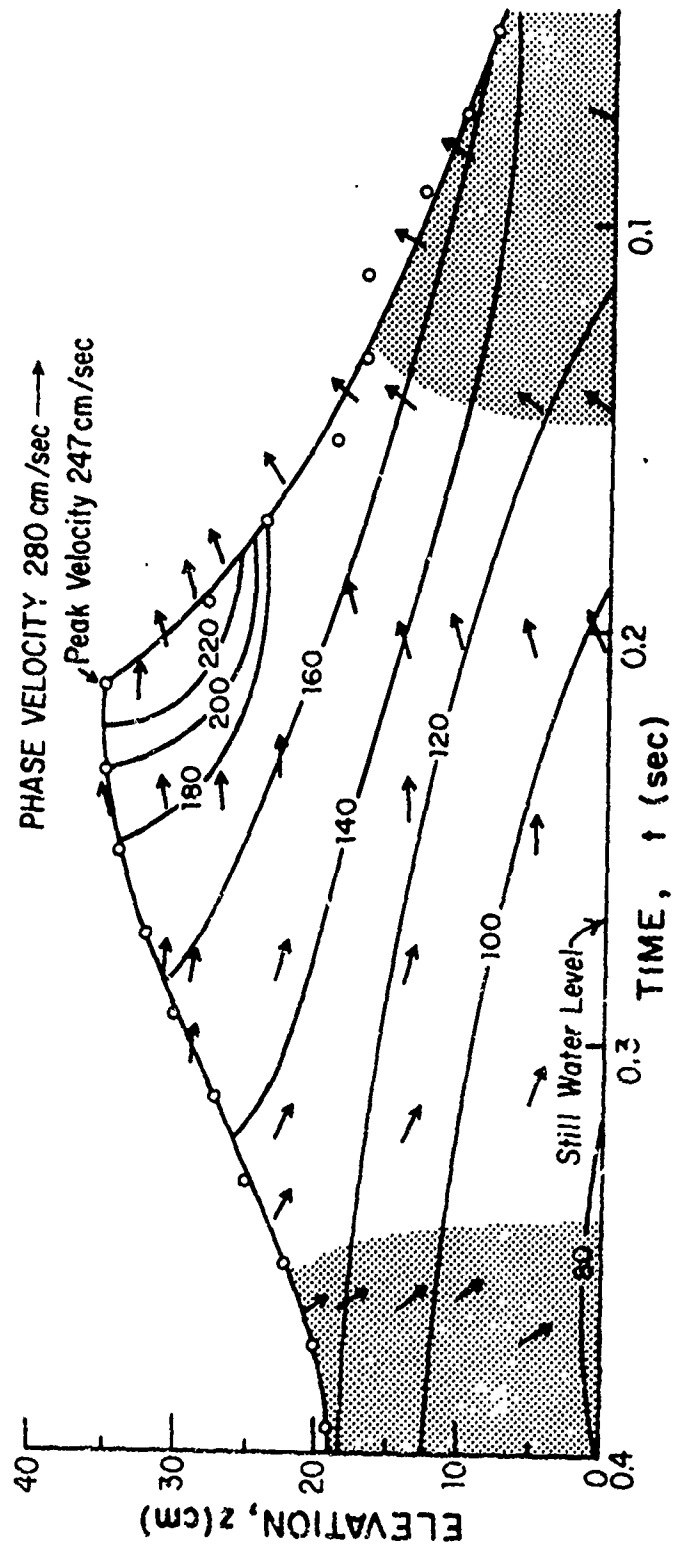


Fig. 16 Velocity field in same wave as Fig. 15, but 0.18 wavelengths before breaking (point B-9, Fig. 9).

Figure 16 shows the same wave about 0.25 sec (0.18 wavelengths) before breaking. Steepness has increased by 32%, and the surface profile has become markedly asymmetric. The higher velocity contours are now concave upward and concentrated toward the forward crest face. All contours are tilted in the direction of wave advance, and only the flow directions resemble those in the previous illustration. The lowest velocity contour shown (80 cm/sec) is also the highest shown in Fig. 15.

Figure 17 shows the wave at the point of plunging. The upper velocity contours have now wrapped around a high-velocity jet issuing from the forward face just beneath the crest at about 1.1 times phase velocity.<sup>1</sup> The crest face itself is approaching verticality, and the flow directions are strongly skewed toward the issuing jet. This picture is in great contrast to a similar representation for a Stokes limiting wave of the same height and frequency (Fig. 18), whose flow directions and velocity contours were computed from Michell's expansion coefficients. More than any other evidence, this comparison demonstrates the inapplicability of steady wave theory to unsteady waves. While the stream-function method of Dean (1965) was developed to calculate the interior potential fields within steady, irrotational waves of arbitrary surface profile, Dean's method must fail at breaking, where the free surface is no longer a streamline, and the interior velocities are double-valued along the vertical. While these details are of obvious significance to an understanding of the breaking process, they comprise such a small fraction of the total field of motion as to be of only secondary importance to the calculation of forces and their moments for engineering purposes. It remains to be shown whether Dean's method otherwise predicts the essential velocity structure.

The distinction between the interior flow fields of heavy vs light-breaking waves can be seen by comparing Figs. 16 and 19. Both waves have about the same height, steepness, surface profile, and are represented about 0.18 wavelength before breaking. However both growth rate and flow velocities at corresponding elevations are much lower in the light-breaking case (Fig. 19). Such a distinction might not be evident from Dean's stream function analysis, since it is derived from a surface profile. Thus, again, the measure of breaking intensity is shown to be the (growth) rate at which a wave deforms as it approaches limiting steepness.

---

<sup>1</sup>The droplets shown are actually higher velocity data separating from the wave face.



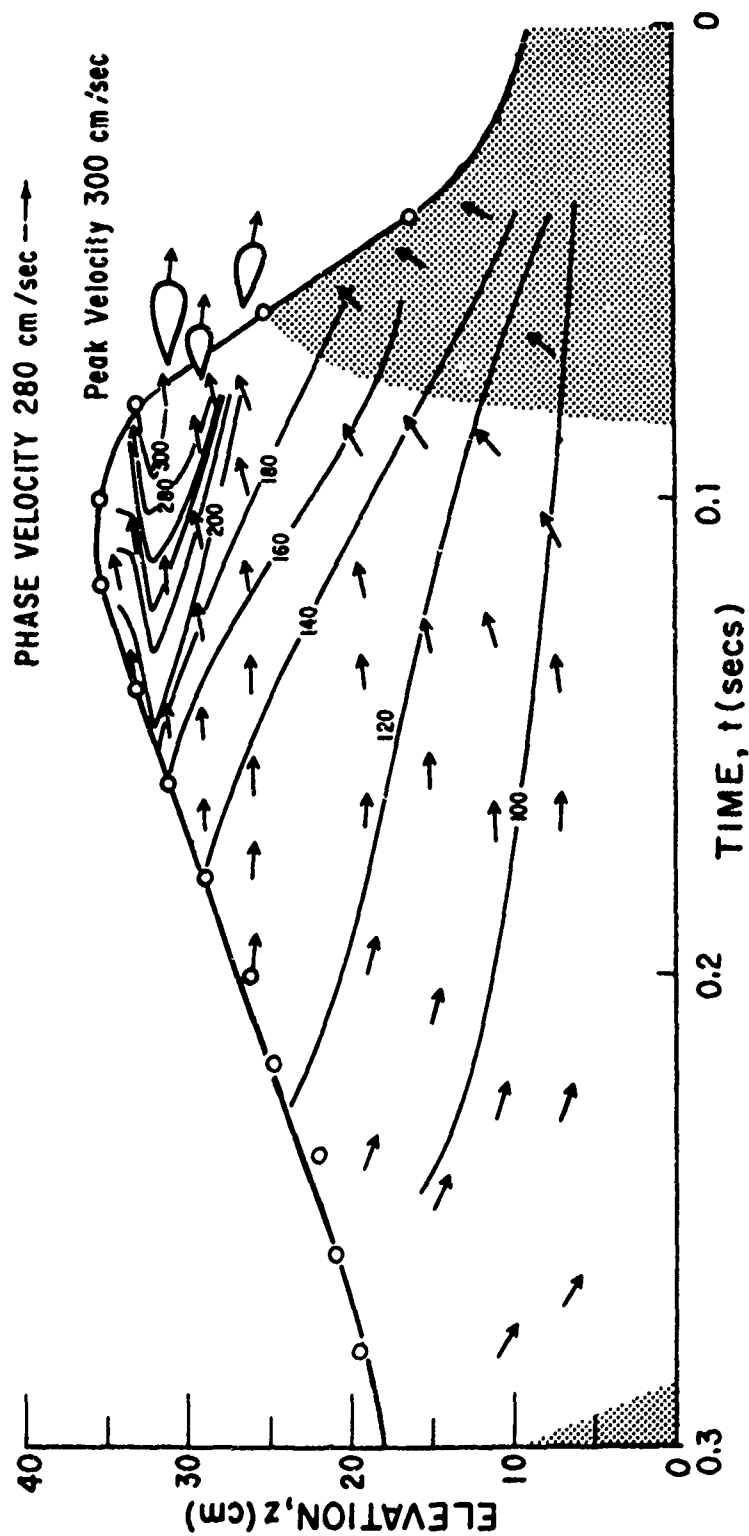


Fig. 17 Same wave as Fig. 16, but at breaking point (B-10, Fig. 9).

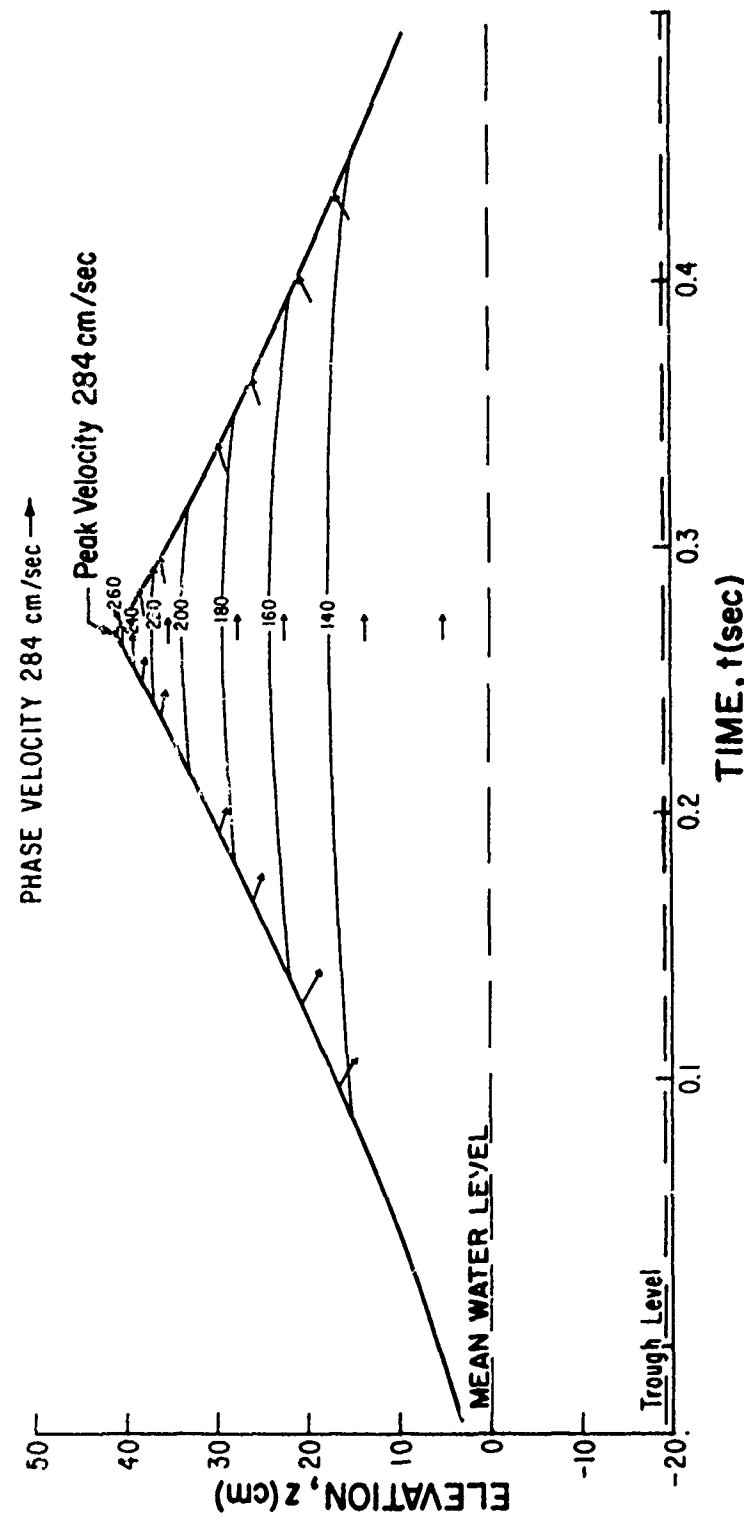


Fig. 18 Calculated velocity field with a limiting Stokes wave of same wave height and frequency as that in Fig. 17.

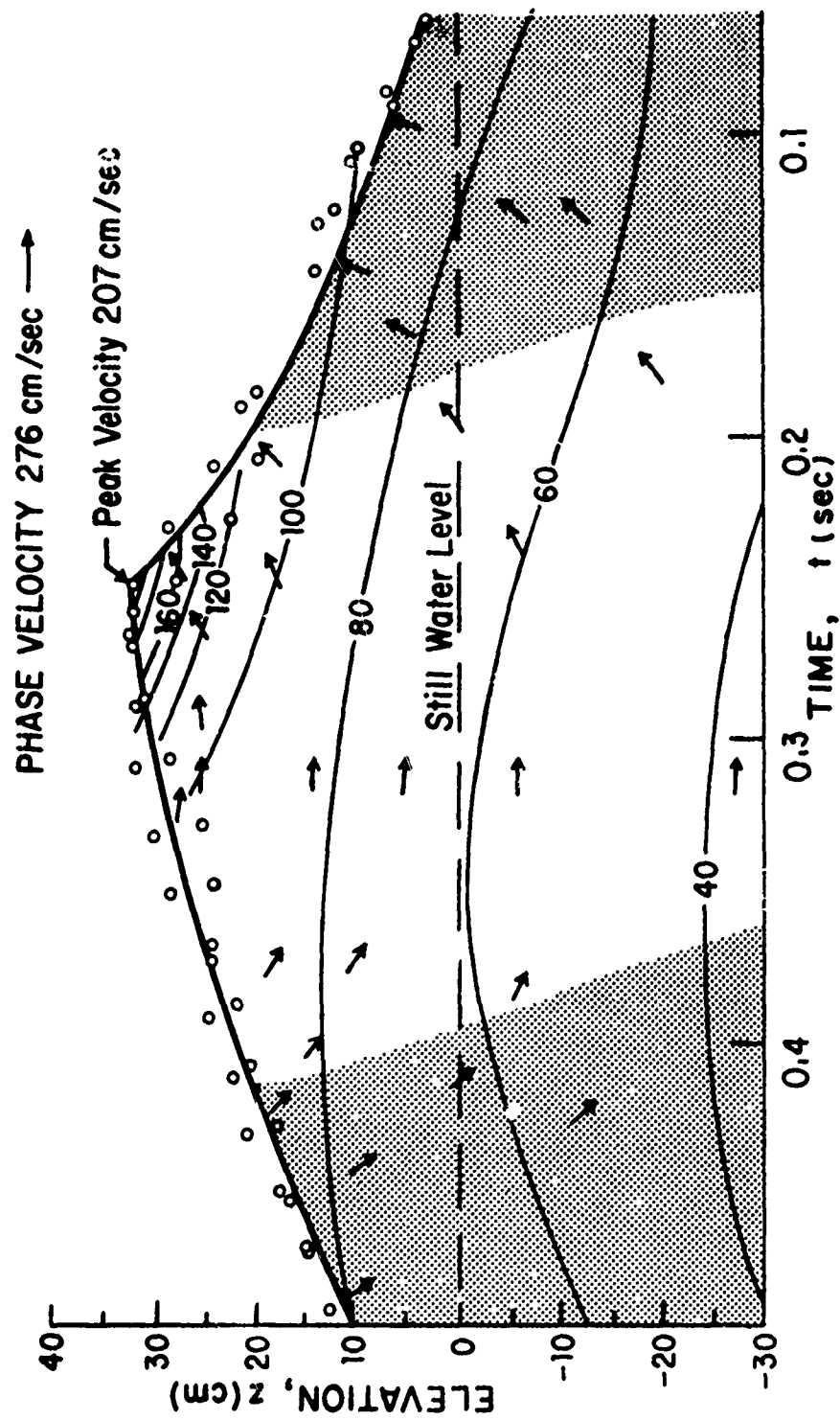


Fig. 19 Velocity field within a lightly breaking 0.66 Hz wave (E-4, Fig. 9) at the same pre-breaking stage as that in Fig. 16.

The principal conclusions resulting from flow velocity measurements can be summarized as follows.

- o Owing to lateral symmetry, the flow fields within unsteady progressive waves of steepness lower than about 0.10 can be calculated with reasonable accuracy by Stokes' 5th-order steady wave theory.
- o As opposed to a singular cusped-crest instability (Price, 1971), breaking appears to be the culmination of a continuous process whose effects extend well below trough level. Beginning at a steepness,  $H/L = 0.1$ , it is characterized by increasing profile asymmetry, tilting of velocity isolines, and progressive increase of velocities at all elevations, until the forward crest face erupts as a jet, slightly beneath maximum crest elevation, and within which flow velocities attain- or slightly exceed- crest speed. Visible evidence of crest instability occurs well in advance of this last stage.
- o The distinction between light and heavy breaking is principally confined to the relative magnitudes of flow velocities, which increase with growth rate.

## 5.5 Surface Profiles

Of all wave parameters, surface elevation is the easiest to measure in the laboratory, if not the field. All later consideration of potential energy and energy loss are based on such measurements. In this section, the steepness limit to which higher order theory reasonably describes wave profiles is examined, together with a more sensitive measure of asymmetry for waves of higher steepness.

### 5.5.1 Low Steepness Profiles

Figure 15 shows that the velocity isolines, flow directions, and surface profile of a young wave (B-3, Fig. 9 and Table I) all exhibit lateral symmetry. Figure 20 compares the complete profile of this same wave to those of the same steepness,  $H/L = 0.10$ , computed from Stokes' theory to 3rd-order (Kinsman, 1965, p. 251), 5th-order (Beach Erosion Board, 1941), and 15th-order (Monkmeyer and Kutzbach, 1965). All profiles were normalized to  $L_*$ , and the measured still-water level was matched to the mean of the computed profiles. Although there appears to be a significant

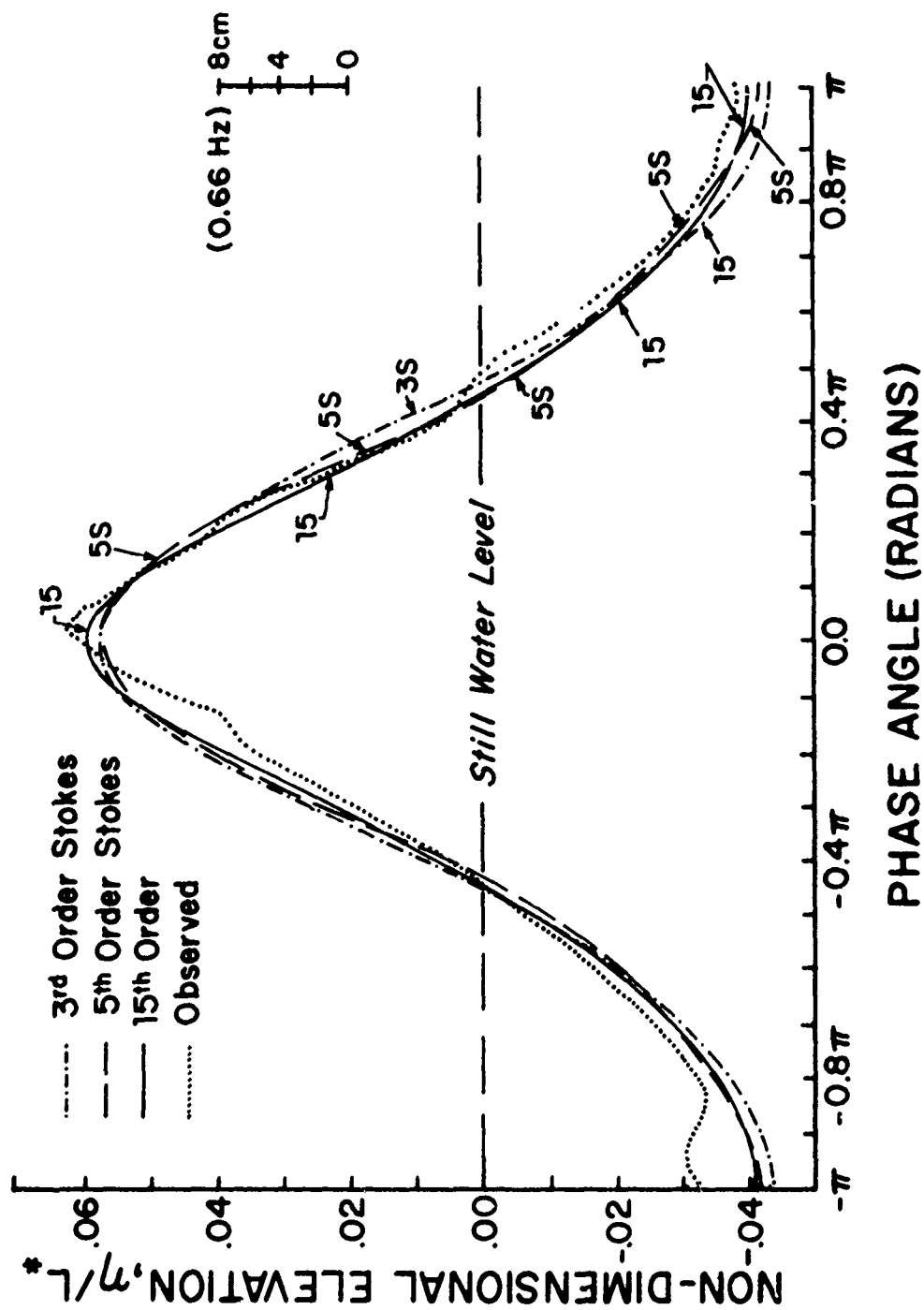


Fig. 20 Comparative profiles of observed surface elevation vs. phase angle for a low steepness ( $H/L = 0.10$ ) 0.66 hz wave, and corresponding profiles for Stokes waves of higher order.

improvement in going from 3rd to 5th order, the distinction between 5th and 15th order is smaller (1 cm) than the measurement uncertainty (2 cm). Thus, as with phase speed and flow velocity, the 5th-order solution can be regarded as adequate to describe wave profiles for  $H/L \leq 0.10$ .

## 5.2 Asymmetry in Steep Waves.

As shown in Figs. 16, 17, and 19, regardless of growth rate, profiles for waves steeper than 0.10 become increasingly asymmetric. These changes are most pronounced near the wave crest and, in heavily breaking waves, occur very rapidly. Figure 21 shows two consecutive photographic profiles of an 0.66 hz wave 0.156 sec. apart (0.12 wavelengths) as it approaches breaking. Within this short interval, the near-vertical crest face has developed into a plunging jet, within which flow velocities exceed the phase velocity by about 8%.

Because growth rate is difficult to assess under field conditions, a search was made for a quantitative measure of asymmetry which might be correlated with growth rate as an alternative parameter. Of several possibilities, the third moment of slope  $A(x,t)^3$  appeared to give most consistent results. For waves moving in the positive x-direction, this moment is given by:

$$A(x,t)^3 = -f^3 L^2 \int_{x-L/2}^{x+L/2} [\partial \eta(x',t) / \partial x']^3 dx' \quad (4)$$

where  $-fL^2$  is an arbitrary normalization. From previously-demonstrated stationarity (Section 5.2), the space-time equivalent of (4) is, approximately,

$$A(x,t)^3 = -1/T \int_{t-T/2}^{t+T/2} [\partial \eta(x,t') / \partial t']^3 dt' \quad (5)$$

If, for any time increment,  $-T/2 < t'' < T/2$ ,  $\partial \eta(t+t'') / \partial t = -\partial \eta(t-t'') / \partial t$ , the profile is symmetrical and  $A(x,t) = 0$ . If the forward wave face is steeper than the back face,  $A(x,t) > 0$ , and conversely. In computer format, (5) was further approximated as:

$$A(x,t)^3 = 1/N \sum_t (\eta_i - \eta_{i-1})^3 / \Delta t^2 \quad (6)$$

where  $\eta_i$  is the  $i$ th elevation sample in a wave staff time series of sample interval,  $\Delta t$ .

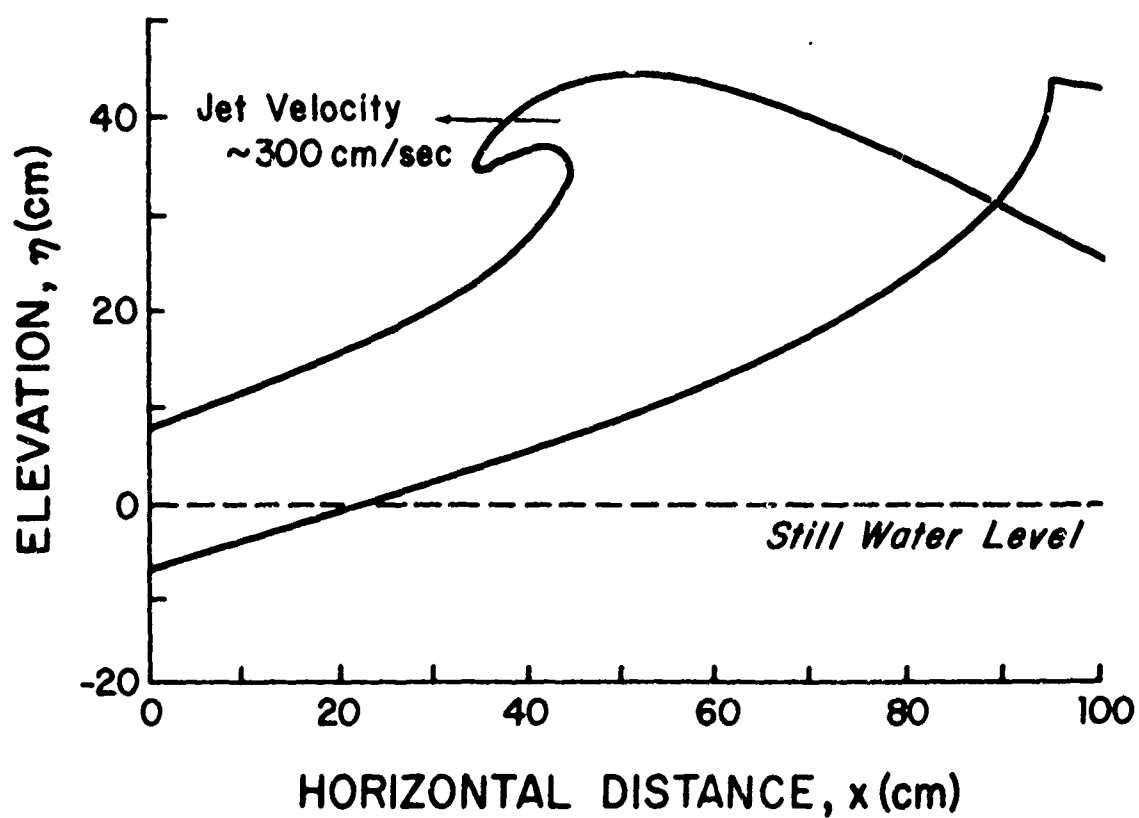


Fig. 21 Photographic profiles of heavily breaking 0.66 hz wave over a time interval of 0.156 sec., showing rapid acceleration of crest to form high velocity jet.

Table III lists the asymmetries calculated from (6) for the first three or four uniform waves averaged over about 20 repetitive runs for light breaking series E-4 and E-5 (Fig. 9), and heavy breaking series B-3, 9, and 10, together with their growth rates and similarly-averaged steepnesses. Although there appears to be a consistent increase in average asymmetry between young and pre-breaking waves, the asymmetry variations among individual waves of a series are substantially larger than corresponding steepness variations, and effectively preclude any distinction between heavy and light breaking, or between pre-breaking and breaking. This (essentially negative) result suggests that steepness is still a more reliable index of breaking, and that the possibility of determining growth rate from surficial evidence appears doubtful.

#### 5.6 Wave Energy

One of the principal objectives of these experiments was to quantify energy lost by wave breaking, and to parameterize energy loss rates in terms of frequency, steepness, and growth rate. Because of decreasing measurement accuracy in flow velocities below about 50 cm/sec., quantitative estimates of kinetic energy were restricted to wave crests above trough level, and then only up to the breaking point. Consequently, all energy estimates reported here refer to potential energies calculated from the variance of surface elevation averaged over time, converted where necessary to space averages by virtue of demonstrated stationarity (Section 5.2). Energy estimates within the breaking zone suffered from corresponding inaccuracies owing to the difficulty of precisely determining the instantaneous surface elevation, and must be regarded only as upper bounds. Despite these shortcomings, by assuming that that total mean energy density was equally partitioned between potential and kinetic, and that total energy flux was conserved before breaking, it was possible to construct reasonable and consistent representations of the energy equilibria prevailing in growing and breaking waves (Section 5.7).



TABLE III  
ASYMMETRY VS. STEEPNESS

$f = 0.66 \text{ hz}$

Station	Order of Wave Arrival	Growth Rate G	Steepness H/L	Asymmetry A (cm/sec)
B-3  (young)	1	0.250	0.093	$0.04 \pm 0.18$
	2	"	0.095	$0.14 \pm 0.19$
	3	"	0.097	$-0.25 \pm 0.06$
	4	"	0.095	$-0.25 \pm 0.16$
E-4  (pre- breaking)	1	0.266	0.125	$0.77 \pm 0.03$
	2	"	0.123	$0.60 \pm 0.04$
	3	"	0.125	$0.32 \pm 0.27$
	4	"	0.132	$0.73 \pm 0.05$
E-5  (breaking)	1	0.295	0.131	$1.24 \pm 0.18$
	2	"	0.138	$0.90 \pm 0.01$
	3	"	0.129	$1.17 \pm 0.03$
	4	"	0.132	$0.47 \pm 0.09$
B-9  (pre- breaking)	1	0.535	0.118	$0.77 \pm 0.16$
	2	"	0.134	$1.51 \pm 0.21$
	3	"	0.132	$0.66 \pm$
B-10  (breaking)	1	0.592	0.132	$0.84 \pm 0.06$
	2	"	0.136	$1.33 \pm 0.09$
	3	"	0.134	$0.61 \pm 0.04$

### 5.6.1 Energy Balance Within a Convergent Channel

In the most general sense, the energy balance equation for surface waves on deep water with no mean flow<sup>1</sup> is given by (Phillips, 1969, p. 50):

$$\partial E(x,t)/\partial t + \vec{\nabla} \cdot \vec{F}_t(x,y,t) = Q(x,t), \quad (7)$$

where  $E(x,t)$  is the total energy density,  $\vec{F}_t(x,y,t)$  the total energy flux, and  $Q(x,t)$  the energy dissipation per unit area. The symbol  $\vec{\nabla}$  is the horizontal gradient operator,  $\hat{i}\partial/\partial x + \hat{j}\partial/\partial y$ , where  $\hat{i}$  and  $\hat{j}$  are unit vectors in the  $x$  and  $y$  directions, respectively. In this study, paddle stroke was kept at a constant amplitude after an initial growth period, so that  $\partial E/\partial t = 0$ ,  $\vec{F}_t(x,y,t) = \vec{F}_t(x,y)$ , and  $Q(x,t) = Q(x)$ .

Figure 22 shows a section of the tapered channel from above. Arrows denote unit vectors  $\vec{n}$  normal to the sides of the quadrilateral area  $A$ . Let  $p$  be the perimeter of  $A$ . If equation (7) is integrated over  $A$  and Green's theorem is applied to the integral, one obtains

$$\int_A \vec{\nabla} \cdot \vec{F}_t(x,y) dA = \int_p \vec{F}_t(x,y) \cdot \vec{n} dp = \int_A Q(x) dA. \quad (8)$$

Letting  $\vec{F}_t(x,y) \cdot \vec{n} = 0$  along the channel walls, and neglecting the  $y$ -component and  $y$ -dependence of  $\vec{F}_t(x,y)$  and  $Q(x)$  along the open ends of  $A$  introduces an error of order  $1 - \cos 6^\circ - 20' \div 0.01$ . Then, if the left end of the quadrilateral is a distance  $x_1$  from the paddle and the right end a distance  $x_2$ , (8) reduces to

$$w(x_2)F_t(x_2) - w(x_1)F_t(x_1) = \int_{x_1}^{x_2} Q(x)w(x) dx, \quad (9)$$

where  $F_t(x)$  is the  $x$ -component of  $\vec{F}_t(x,y)$ .

Equation (9) expresses the conservation of energy flux in a slowly converging channel. It can be put in more useful form incorporating the growth rate,  $G = -L_*(\partial w/\partial x)/w$ , by holding  $x_1$  constant, and differentiating with respect to  $x$ -variable:

$$-F_t(x)G/L_* + \partial F_t(x)/\partial x - Q_v(x) - Q_r(x) = Q_b(x), \quad (10)$$

where  $Q_v$ ,  $Q_r$ , and  $Q_b$  are losses attributable to viscous dissipation, reflection, and breaking, respectively. The problem of determining breaking losses, then, reduces to evaluating the terms on the LHS of (10).

<sup>1</sup>In these experiments, data sampling was concluded before transport could establish even transient mean flow.

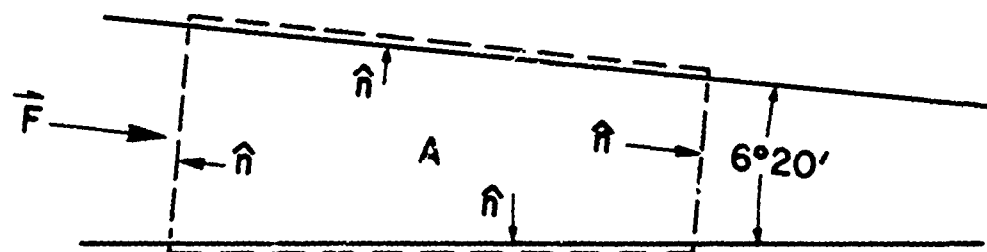


Fig. 22 Plan view of the convergent channel.

### 5.6.2 Energy Flux

For small amplitude waves propagating in one direction, energy flux is conventionally given by:

$$F_t(x) = C_g E(x), \quad (11)$$

where  $C_g = \partial\omega/\partial k = g/4\pi f$  is the group velocity, and  $E(x)$  the total energy density. Hayes (1973) has recently shown that (11) also applies to finite amplitude waves in deep water, provided that the proper dispersion relation is used in determining  $C_g$ , and that  $E(x)$  is equally partitioned between potential and kinetic energy.

For present purposes, group velocity was determined from (2b) by taking  $f = 2\pi/\omega$  and  $C_g = \omega/k$ , and solving for the differential relation:

$$C_{g5} = \partial\omega/\partial k = (g/4\pi f) [1 + \frac{3}{4}(kH)^2 + \frac{5}{16}(kH)^4] \quad (12)$$

Although, as previously stated, total kinetic energy was not determined in these experiments, it is shown in Appendix G that the error in assuming energy equipartition in the steepest and most asymmetric waves observed in the converging channel is substantially less than 4%. Accordingly,

$$\rho g E(x) = 2\rho g E_p(x), \quad (13)$$

where  $\rho g E_p(x)$  is the potential energy density.

Potential energy density was calculated here from the discrete time series:

$$\rho g E_p(x, t) = \frac{\rho g}{2T} \sum_{t-T/2}^{t+T/2} \eta(x, t')^2 \Delta t' \quad (14)$$

which can be compared with its spatial equivalent (Kinsman, 1965, p. 146):

$$\rho g E_p(x, t) = \frac{\rho g}{2L} \sum_{x-L/2}^{x+L/2} \eta(x', t)^2 \Delta x'. \quad (15)$$

Their normalized difference,  $[E_{px}(x, t) - E_p(x, t)]/E_p(x, t)$ , is estimated to be less than 0.03 (Appendix C).

Combining equations (12), (13), and (14), the expression for total energy flux,  $F_t(x)$ , becomes,

$$F_t(x) = 2F(x) = 2\rho g C_{g5} E_p(x). \quad (16)$$

### 5.6.3 Viscous Dissipation

The spatial degradation of wave amplitude by viscous dissipation within layers at the bottom, sides and free water surface of waves in a channel is given by (Van Dorn, 1965):

$$\eta_2 = \eta_1 \exp - \int_{x_1}^{x_2} \frac{2}{w(x)} (\nu/4\pi f)^{1/2} \left[ \left( \frac{k w(x) (1 + \cosh^2 kD) + \sinh 2kD}{2kD + \sinh 2kD} \right) \right] k dx, \quad (17)$$

where  $\nu$  is the kinematic viscosity, and  $k(x) = 2\pi f/C_5$ . Energy dissipation was calculated from this equation by approximating energy density by  $\eta^2$ . This was an accurate estimate because the spectral peak at the paddle frequency,  $f$ , contained over 90 percent of the wave energy (Appendix B).

Over the travel distances listed in Table II, maximum energy losses, computed before breaking for all frequencies, varied from 3 to 4%, which was small compared to the energy increase (about 100%) occurring during wave growth. Accordingly it was assumed that  $Q_v = 0$  in Eq. (10).

### 5.6.4 Wave Reflection

Of several possible approaches to estimating the amount of wave energy reflected from the converging channel walls, that adopted here essentially reduces to calculating energy flux with the assumption of no reflection losses, and then estimating the attendant error from the variance of the computed results from lines of conserved flux. Energy flux is discussed in Section 5.7.1, and the above calculations are described in Appendix E. The results indicate that less than one per cent of incident energy was reflected before breaking, so that  $Q_r = 0$  in Eq. (10).

### 5.6.5 Potential Energy After Breaking

Because breaking turbulence-particularly on the forward wave face-could be expected to render continuous wave staff records somewhat ambiguous,

independent evidence was sought for obtaining more-accurate estimates of mean-square elevation after breaking. Figure 23 shows photographically that the crests and troughs of even a heavily breaking wave were relatively smooth, so that wave height could be estimated within about 2 cm.

Figure 24 is a plot of mean-square surface elevations before and after breaking versus the Stokes linear wave energy parameter,  $H^2/16$ , for two frequencies and a wide range of steepnesses. The solid curve for Stokes 5th-order potential energy was computed from the expansions given by Mason (Beach Erosion Board, 1941), using  $k = 2\pi f/C_5$ . From this figure, it can be concluded that:

- o The breaking and non-breaking distributions are reasonably colinear, with increasing scatter at high steepness.
- o The fact that mean-square elevations among breaking waves do not differ significantly from those among non-breaking waves, independent of frequency or steepness, has possible application to energy determinations from measurements of surface elevation in storm seas.
- o Both data distributions fall systematically beneath the Stokes 5th-order curve, by amounts that increase with steepness.

The dashed curve in Fig. 24 was computed from the empirical expression:

$$E_p = \frac{H^2}{16} \left(1 - A \frac{H^2}{L_*^2}\right), \quad (18)$$

where  $A = 6.70$  is the solution of (18) for  $H = H_*$  and  $E_p = E_{p*}$  = mean-square elevation for a limit Stokes wave.

While this curve may have no physical significance, it does pass through the point defined by the potential energy for a Stokes wave of limiting steepness, and it provides a convenient and adequate description of the data distribution.

## 5.7 Energy Flux and Breaking Losses

Having reasonably established the energy flux equilibrium within the convergent channel in terms of measureable variables, it remains to attempt to relate local equilibria to frequency, steepness and growth rate, in order to quantify energy loss rate as a measure of breaking intensity.



Fig. 23 Trough (upper) and crest (lower plate) of a 0.66 Hz, heavily breaking, wave 18 m from the paddle. The vertical scales are in decimeters.

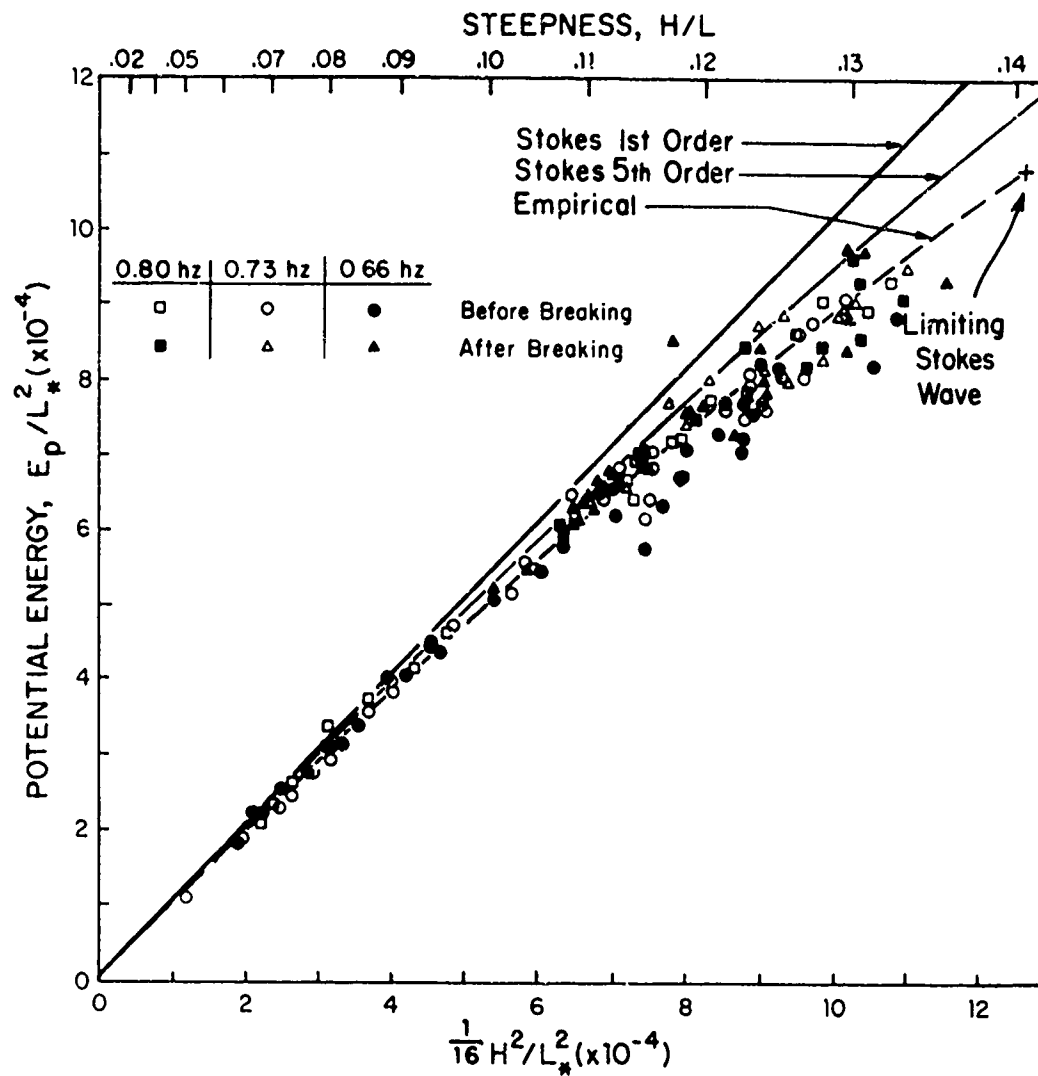


Fig. 24 Comparison of mean-square surface elevation with potential energies computed from Stokes 1st and 5th-order theory.



### 5.7.1 Flux Conservation Before Breaking

Prior, at least, to breaking, it has been shown that viscous dissipation and reflected energy can be neglected, so that  $Q_v = Q_r = Q_b = 0$ , energy flux is conserved, and equation (10) can be written:

$$G/L_* \equiv -(\partial w / \partial x) / w = (\partial F_{tx} / \partial x) / F_{tx} \quad (19)$$

Integrating (19) between the limits  $x_0$  and  $x$ , and recalling (18), one obtains:

$$G/G_0 = F_x(x) / F_x(x_0), \quad (20)$$

which shows that energy flux is proportional to growth rate when normalized to common initial conditions. For present purposes,  $F_0 = F_x(x_0)$  was arbitrarily chosen to be that flux corresponding to  $G = G_0 \doteq 0.19$ , since, for all wave series in Table II, there happened to be a station where growth rate was close to this value, and no wave had yet broken.

Evidence that the experimental non-breaking energy flux determinations are consistent with (20) is shown in Figs. 25-27 for all wave series at the three operating frequencies listed in Table II. Since the data series were ordered in terms of increasing paddle amplitude, commencing with strokes so small that no breaking occurred within the test section (Series A), these data never depart significantly from the conserved-flux lines, whose slopes are:  $F/F_0 G_0 = 1/0.19 = 0.67$ . With increasing wave amplitude (initial steepness), breaking of successive wave series - as indicated by dashed branchings from these lines - occurred with decreasing intensity at correspondingly lower growth rates. If this qualitative presumption is true, the branch points marking the onset of breaking energy loss should also be correlated with growth rate. The difficulty here is the precise determination of the branch points. For a given wave series, normalized energy flux is essentially the product of the square of wave steepness (Fig. 24) multiplied by group velocity, both of which vary monotonically with growth rate, so that their product has no well-defined maximum at breaking. Accordingly, the best estimates of breaking inception were here taken as the dashed intercepts of the post-breaking flux lines in Figs. 25-27 with the lines of conserved energy flux. These, normalized by  $L_*^3 f$  to remove frequency dependence, are plotted against growth rate in

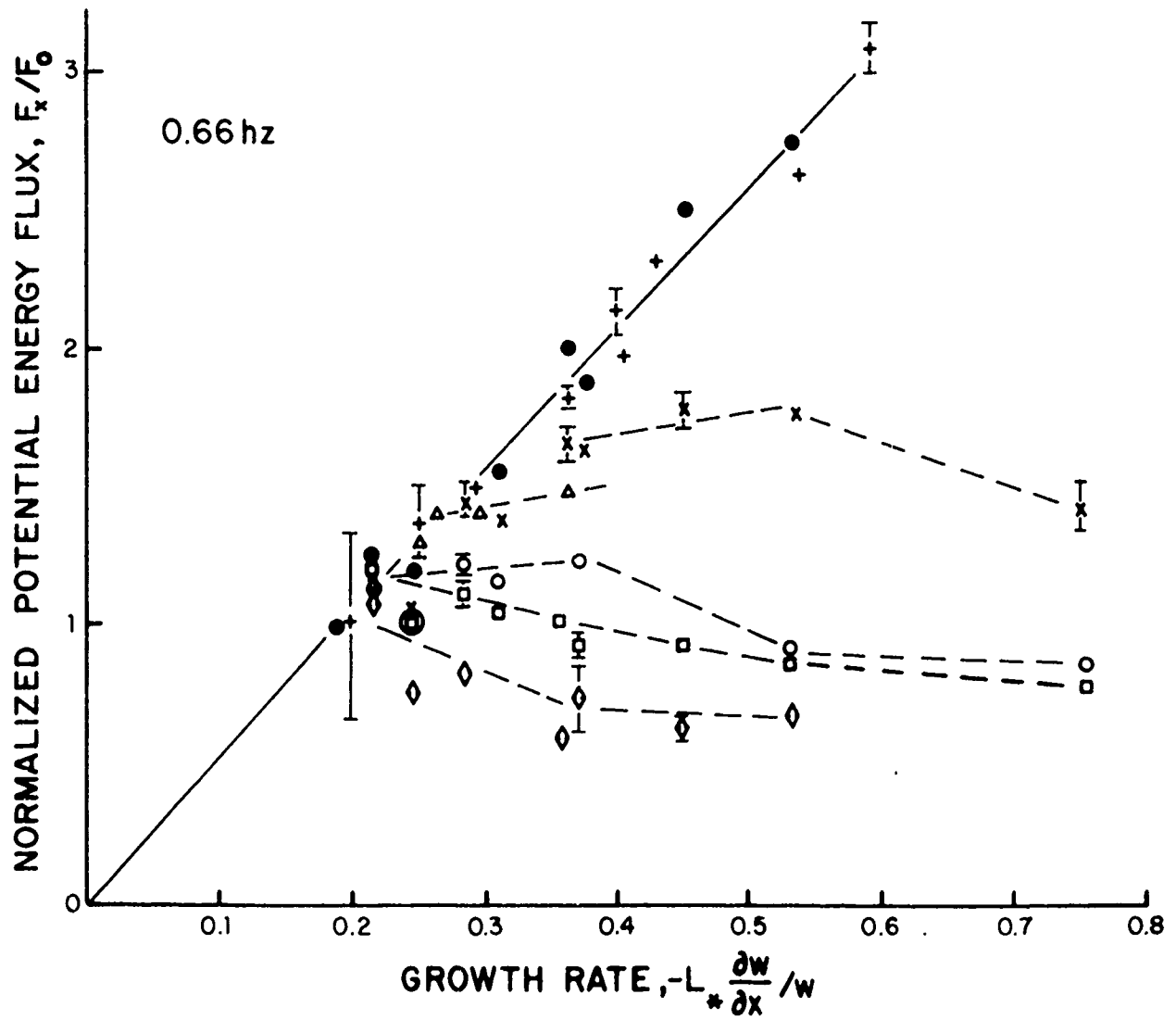


Fig. 25 Energy flux vs. growth rate at  $f = 0.66$  Hz for seven initial wave steepnesses.

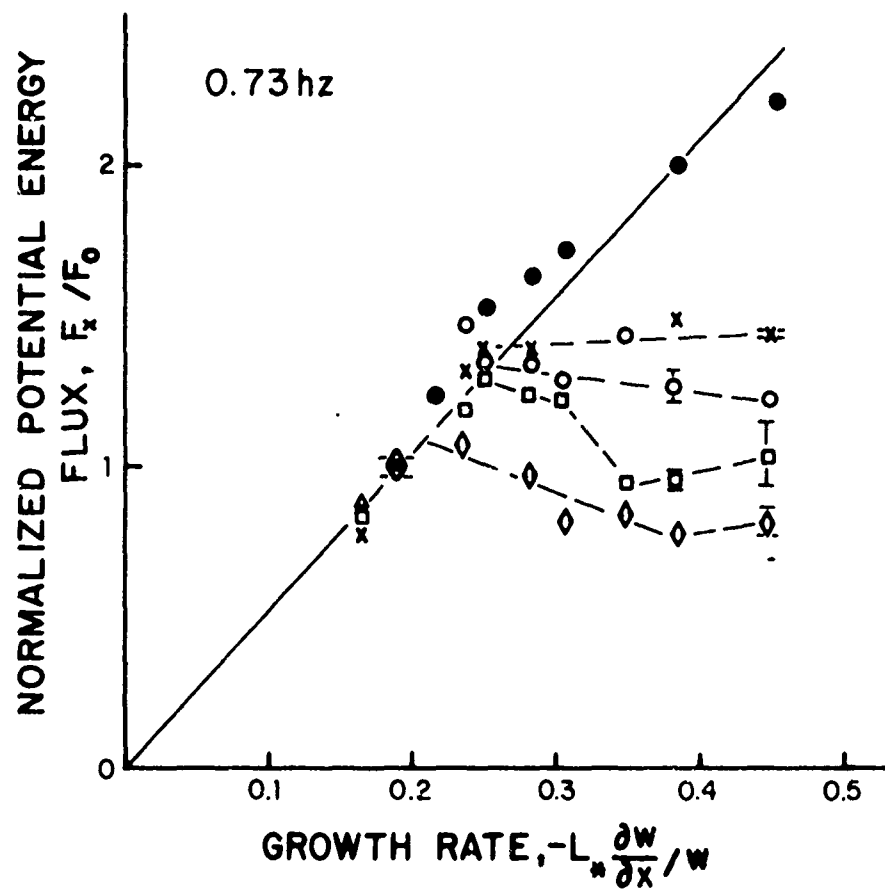


Fig. 26 Energy flux vs. growth rate at  $f = 0.73$  Hz for five initial wave steepnesses.

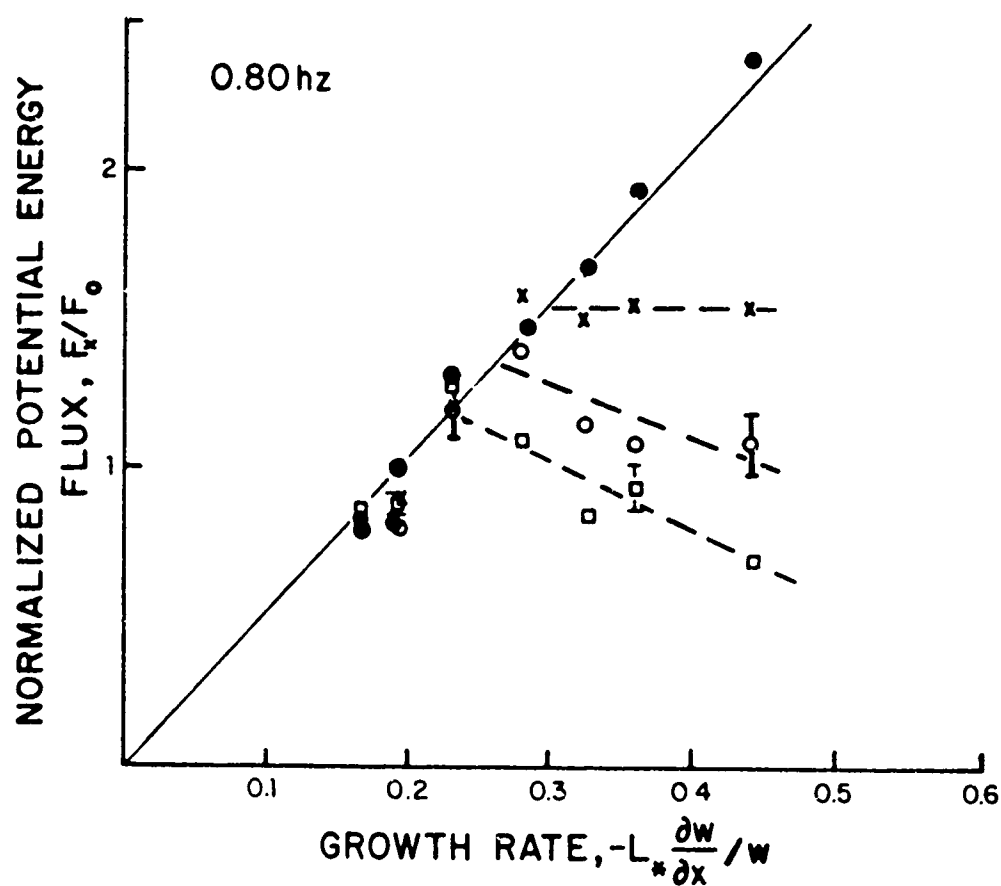


Fig. 27 Energy flux vs. growth rate at  $f = 0.80$  Hz for four initial wave steepnesses.

Fig. 28. Expectedly, the data distribution much resembles that for breaking steepness (Fig. 10), exhibiting considerable scatter with, perhaps, a slight tendency to increase with growth rate. The dashed line, drawn through the data by inspection, is convex upward in accordance with the intuitively-reasonable assumption that normalized energy flux must approach some asymptotic limit as  $G \rightarrow \infty$ .

### 5.7.2 Breaking Energy Loss Rate

Subsequent to breaking,  $Q_b \neq 0$ , and (10) becomes:

$$\partial F_t / \partial x - F_t G / L_* = Q_b. \quad (21)$$

Recalling (16), and making use of the operator,  $\partial / \partial x = G^2 (\partial / \partial G) / L_*$ , (21) can be written:

$$\rho g Q_b = \frac{2 \rho g F_0 G}{L_*} \left[ \frac{G}{F_0} \frac{\partial F_x}{\partial G} - \frac{F_x}{F_0} \right] \text{ (ergs/cm}^2\text{-sec),} \quad (22)$$

which must be satisfied along the dashed branched lines in Figs. 25-27.

A more convenient measure of energy loss rate is its ratio, per wave cycle, to the average energy present,  $E = 2F_x / C_{g5}$ :

$$\frac{Q_b}{FE} = -G \frac{F_0}{F_x} \cdot \frac{C_{g5}}{C_*} \left[ \frac{F_x}{F_0} - \frac{G}{F_0} \frac{\partial F_x}{\partial G} \right] \quad (23)$$

In this equation, all quantities are known, except for the normalized flux gradient parameter,  $(1/F_0)(\partial F_x / \partial G)$ , which is given by the slopes of the above branch lines.

As with the branch points, the quantitative determination of potential flux gradients is somewhat subjective, since they depend upon small variations in group velocity and potential energy amid significant data scatter. Qualitatively, the dashed lines in Figs. 25-27 appear to have systematically negative slopes at low transition growth rates (large initial wave amplitude and weak breaking); slopes tend to increase with transition growth rate (greater breaking intensity), and, perhaps, even go slightly positive during the early stages of intense breaking. Despite these initial (transitional) tendencies, all slopes tend toward zero if breaking proceeds long enough.

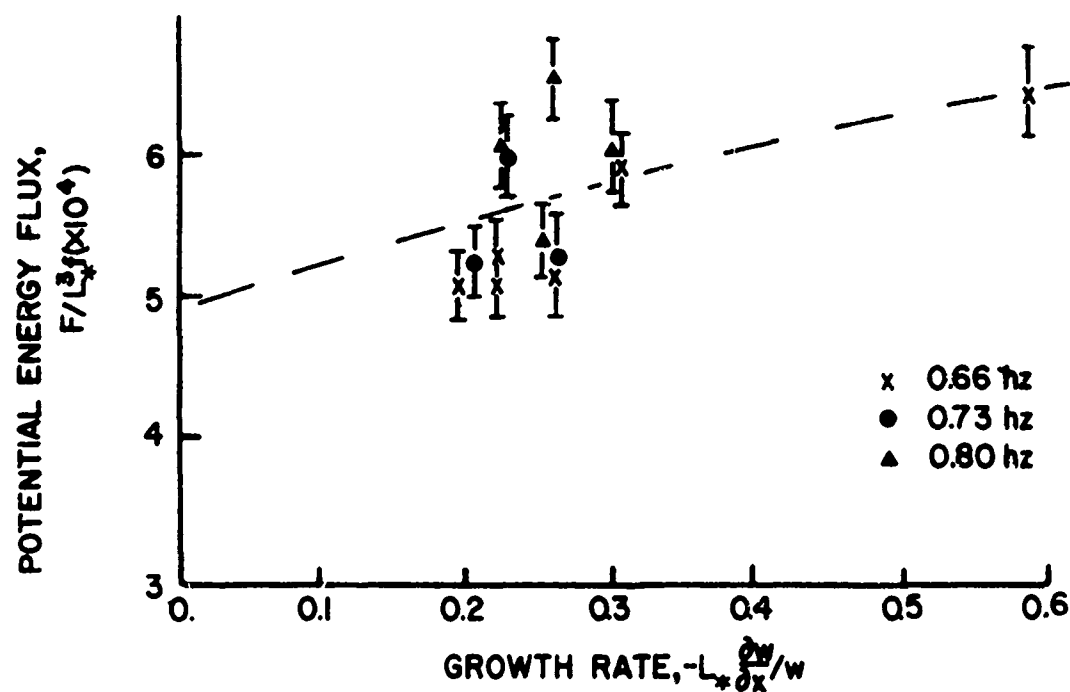


Fig. 28 Energy flux at breaking inception vs. growth rate.

As regards equation (23), the physical interpretation to be placed on these tendencies is tentatively the following. A zero flux gradient implies that breaking energy loss is always in equilibrium with the energy input imposed by channel convergence, the rate of both being determined by a wave's initial steepness and growth rate. Just prior to breaking transition, there appears to be tendency for all waves to overshoot their respective equilibrium breaking flux rates, and to decay back to the equilibrium rate as breaking continues. Both overshoot and decay rate appear to increase with breaking intensity.

For lack of sufficient data to properly quantify these transient approaches to equilibrium, breaking energy losses were instead estimated by considering the extreme ranges of relevant variables:

- o potential energy flux gradient;  $-2 < (1/F_0) (\partial F_x / \partial G) < 0$
- o breaking steepness;  $0.125 < H/L < 0.140$
- o normalized group velocity;  $0.64 < C_{g5}/C_* < 0.70$

Figure 29 is a plot of normalized energy loss rate at breaking transition (Eq. 23) versus growth rate. The straight lines bounding the "error" bars give, roughly, the uncertainty attached to determinations of energy flux rate for all wave series in Table II. Uncertainty of group velocity is given by the shaded bands centered on these lines. The upper line might be considered the best estimate of breaking overshoot, and the lower line that for equilibrium breaking loss, corresponding to  $Q_b/fE = -0.93G$  and  $-0.67G$ , respectively. Thus, within the range of these experiments, breaking loss rates amount, roughly, to:

Breaker Type	Growth Rate $G = -L_*(\partial w / \partial x) / w$	$Q_b/fE$ (per cent/cycle)	
		Transition	Equilibrium
Light	0.2	19	13
Heavy	0.6	57	39*

\*This value is an extrapolation, since no equilibrium breaking was observed at this growth rate because of limited channel length.

The above rates indicate substantial energy losses--even for light breaking, and the median value (26%) for equilibrium breaking is about 3000 times larger than that per mean wave cycle estimated for sea waves (Longuet-Higgins, 1969b). While this result may have little significance to natural

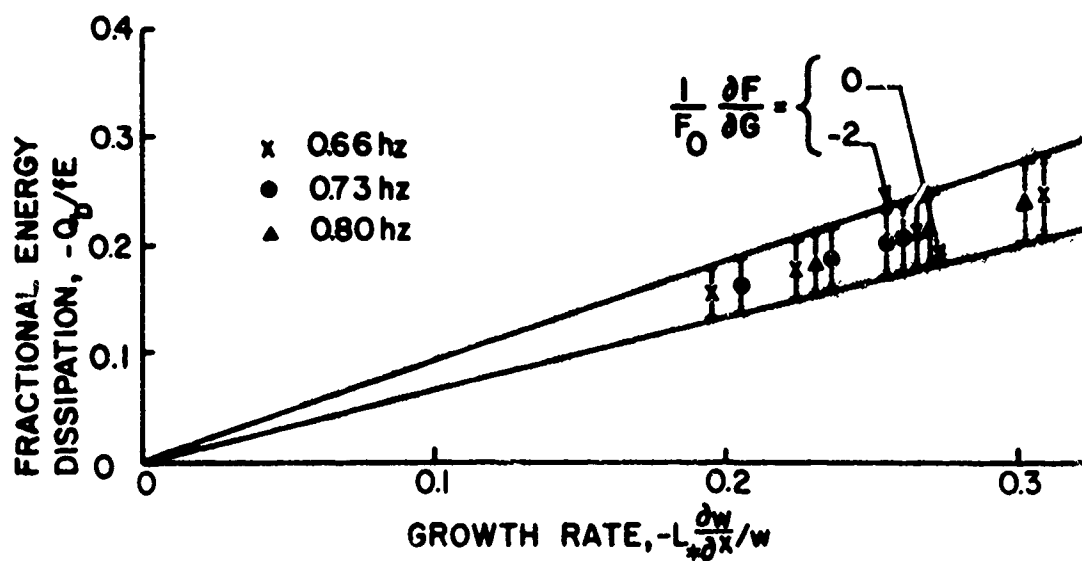


Fig. 29 Transitional (upper) and equilibrium (lower) breaking energy loss rates as a function of growth rate.



conditions, the concept of growth rate is perfectly general. Its application to the more natural case of biharmonic waves breaking as a result of constructive interference is discussed in the next section.

## 6. DISCUSSION

This section is devoted first to a brief summary and interpretation of the principle results of this study and, second, to an extension of these results to an estimate of the energy loss rate attributable to waves breaking solely by virtue of constructive interference among components of a narrow spectrum.

### 6.1 Results Summary and Interpretation

The growth towards breaking of uniform trains of periodic deep water waves propagating within a straight-sided convergent channel was found to be characterized by three successive, steepness-dependent phases:

- 1) a young phase ( $0 < H/L < 0.10$ ), wherein surface profiles and internal flow fields are symmetric and, together with phase (crest) speeds, are roughly in accord with those predicted by Stokes steady wave theory to 5th order;
- 2) a pre-breaking phase ( $0.10 < H/L < 0.125$ ), wherein there is no obvious surface manifestation of crest instability, but where crest profiles are markedly unsymmetric, flow isolines are concave upwards and tilted in the direction of wave propagation, and strong velocity gradients develop just beneath the crest;
- 3) a breaking phase ( $0.125 < H/L < 0.14$ ), involving verticality of the forward crest face, obvious crest instability, and increased tilting and curvature of sub-crest fluid velocity isolines so as to form a plunging jet, within which flow velocities equal or exceed the local crest speed.

Except for phase speed, which continues to accord with Stokes 5th-order theory, none of the properties described in phases (2) and (3), above, are predicted by any steady wave theory. The fact that their degree and speed of occurrence increases with growth rate,  $G$ , suggests that they involve unsteady (accelerative) processes. At the same time, evidence for

continued stationarity (space-time equivalence) right up to breaking suggests that these changes are not specific to a convergent channel, but would occur similarly in a parallel channel, if its width could somehow be mechanically decreased at corresponding rates.

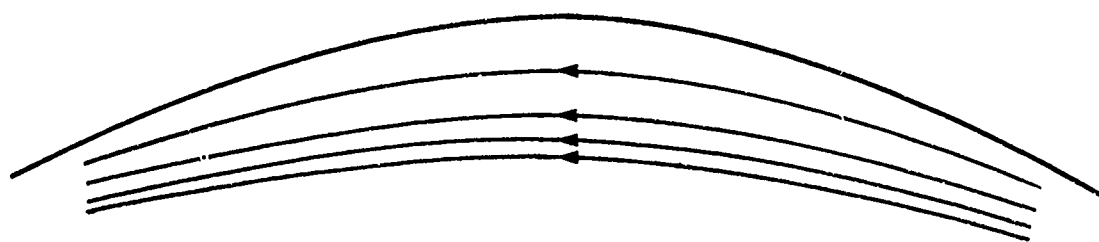
An alternative and, perhaps, intuitively clearer picture of the internal flow field changes associated with terminal wave growth is given by the "streamline" representations in Fig. 30a, b, c, whose indices correspond, respectively to the three growth phases described above, as well as to the flow-isoline representations for a heavily-breaking 0.66hz wave shown in Figs. 15-17. In a coordinate system moving at wave speed, streamlines can be defined as curves everywhere parallel to the local flow direction whose spacing varies inversely with flow velocity. While the curves shown were subjectively contoured from observational flow and profile data<sup>1</sup>, they provide a qualitative insight to breaking kinematics.

In a steady inviscid (young) wave (Fig. 30a), the surface is a streamline, and all subsurface streamlines are homologous nested curves, symmetric about the wave crest. With increasing steepness, (Fig. 30b), profile asymmetry is reflected by corresponding streamline asymmetry, at least to trough depth. However, with breaking (Fig. 30c), the flow is no longer steady; streamlines can terminate in the surface, or inviscid flow can create a vortex. While the vortex shown is speculative, the indicated flow reversal corresponds to fluid velocity exceeding phase speed, and offers a possible explanation for the observation that the breaking jet always issues somewhat below the wave crest. If this concept has physical validity, one expects that energy dissipation could arise both from vortex shear and jet advection out of the wave.

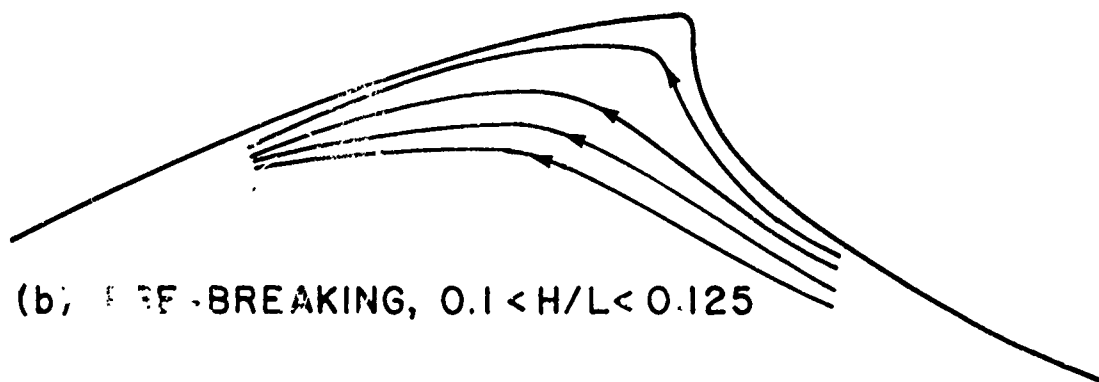
As regards the energy balance in growing waves, the following points can be made. The fact that potential energy flux was found to be conserved right up to breaking transition is perhaps the best indication that potential flow persists, and that kinetic energy flux is similarly conserved. This conclusion is supported by the arguments for energy equipartition presented in Appendix G. The onset of breaking-defined by a relatively abrupt drop in the local energy flux rate-was invariantly

---

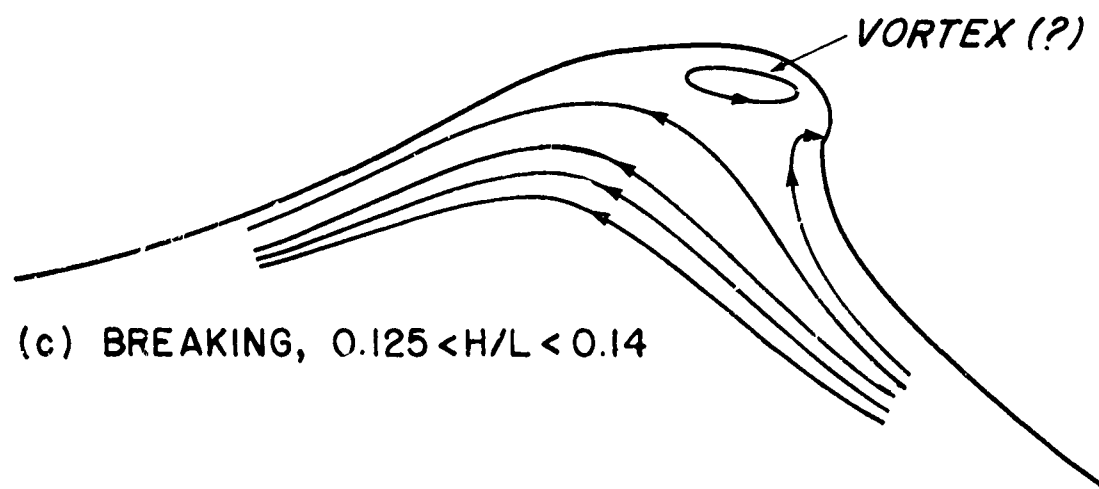
<sup>1</sup>An attempt was made to calculate streamlines directly by least-squares fitting the observed flow fields to 7th-order polynomials. But even this order was insufficient to follow details of crest flow.



(a) YOUNG,  $H/L < 0.1$



(b) PRE-BREAKING,  $0.1 < H/L < 0.125$



(c) BREAKING,  $0.125 < H/L < 0.14$

Fig. 30 Streamline representation of consecutive wave growth stages.

associated with a transient normalized energy loss rate of about,  $Q_b f/E = -0.93G$ , that decayed within a wavelength to an equilibrium level of about two-thirds this rate. Such an equilibrium implies that waves lose energy through breaking at just the rate at which it is supplied by channel convergence. Thus the equilibrium energy flux is also proportional to growth rate. Since the former is approximately the product of group velocity times twice the local energy density, both of which are weak, monotonically increasing functions of steepness (Eqs. 12 and 18), the above proportionality implies that equilibrium breaking steepness must also increase weakly with increasing growth rate. Although the experimental data are not sufficiently accurate to quantify this premise, the entire range of breaking steepness ( $0.125 < H/L < 0.14$ ) indicates that a steepness increase of only 12 percent triples the breaking loss rate. (13-39 per cent/cycle).

## 6.2 Interactive Breaking

A logical extension of these results is the question of their application to the breaking of wind waves at sea. Despite the recognized randomness of sea waves, when the wind is steady-as in the trades-the surface is often characterized by the appearance of rather regular wave groups. Owing to small directional differences of energy propagation, the groups are staggered in a 'chicken-wire' pattern. Under such circumstances, Donelan, et al (1972) have observed-and confirmed by simple experiment-that breaking occurs systematically at the group antinodes at intervals of about twice the period of the principal waves. While breaking of this type requires a fairly narrow frequency and direction spectrum, there is increasing evidence (Rye, 1974) that the storm wave spectrum is rather narrower than that earlier proposed by Pierson and Moskowitz (1964). Lastly, preliminary experiments with interactive breaking among waves of a unidirectional biharmonic series in the present (non-convergent) wave channel fully substantiates the premise that regular breaking can be produced by constructive interference in the absence of wind. The ensuing discussion advances the hypothesis that variable steepness and growth rate may account, in part, for the qualitative features observed.

Consider, as the simplest example, a linear biharmonic wave train composed of two sinusoids having the same amplitude,  $a$ , but different radian frequencies,  $n_1 > n_2$ , and wave numbers  $k_1 > k_2$ , related by  $k = n^2/g$ :

$$\eta(x,t) = a \cos(k_1 x - n_1 t) + a \cos(k_2 x - n_2 t). \quad (24)$$

Although breaking may depend weakly upon nonlinear effects, the time and place-and perhaps the duration-of breaking should coincide roughly with this linear model.

The general nature of breaking interaction is better visualized by an alternative form of (24):

$$\eta(x,t) = 2a \cos(k_c x - n_c t) \cos(k_m x - n_m t), \quad (25)$$

where the subscripts  $c$  and  $m$  represent mean sums and differences, respectively, of the component frequencies and wavenumbers defined above. Observed in space at a fixed time (Figure 31a) or in time at a fixed point, the wave form is a carrier wave of amplitude  $2a$ , frequency  $n_c$ , and wavenumber  $k_c$ , modulated by a sinusoidal envelope of frequency  $n_m$ , and wavenumber  $k_m$ . In a tank experiment where such a disturbance is generated by a wave paddle, the carrier waves are those actually seen by an observer; they move at "phase velocity",  $C_c = n_c/k_c$ , passing through the invariant modulation envelope, which propagates a "group velocity",  $C_m = n_m/k_m$ . At any instant, the number of carrier waves in a group is,  $N = k_c/2k_m$ .

By analogy to the convergent channel, it is now supposed that carrier wave growth is everywhere specified by frequency,  $n_c$ , and the local values of steepness ( $H_c/L_c$ ) and growth rate,  $G_c$ , and that breaking will occur whenever the local steepness exceeds some critical value, say,  $H_c/L_c \geq 0.13$ .

The parametric transformation is most simply developed in a coordinate system moving at phase velocity,  $C_c$ , so that  $x = x' + C_c t$ , where  $x'$  is the space coordinate fixed to some particular wave. If the time coordinate is redefined as  $t = t' - (k_m x'/n_c B)$ , where  $B = (k_m n_c - k_c n_m)/k_c n_c$ , and  $t' = 0$  at the antinode of the modulation envelope (Fig. 31a), equation (25) can be rewritten as:

$$\eta(x',t') = 2a \cos(k_c x') \cos(B n_c t'). \quad (26)$$

Thus, as a carrier wave passes through a node of the modulation envelope,

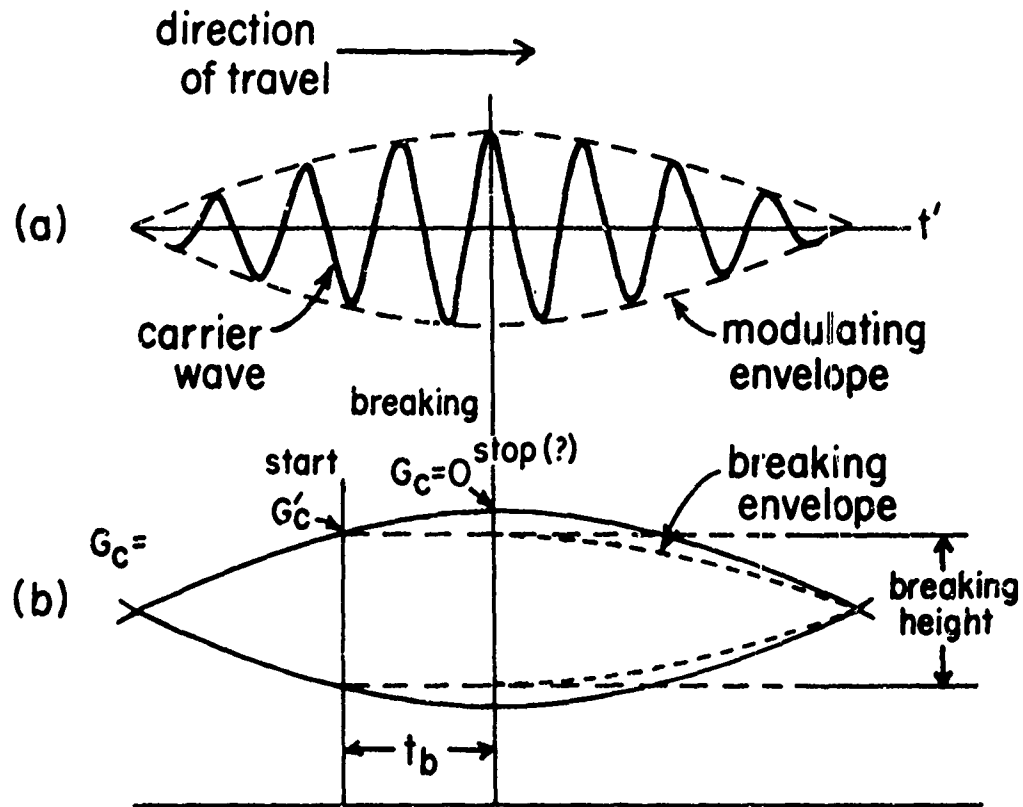


Fig. 31 (a) Biharmonic wave packet composed of carrier waves modulated by a low frequency envelope.  
 (b) Equilibrium breaking of duration  $t_b$  reduces post-breaking envelope, as shown by dashed curves.

it grows with time,  $t'$ , and its local steepness is given by:

$$H_c/L_c = H_c k_c / 2\pi = \frac{4a}{L_c} \cos(Bn_c t') = \frac{4a}{L_c} [1 + \tan^2(Bn_c t')]^{-1/2} \quad (27)$$

The carrier wave energy flux,  $F_c$ , is proportional to its potential energy density, hence to the square of the modulation amplitude:

$$F_c \sim \cos^2(Bn_c t'). \quad (28)$$

Accordingly, by analogy to equation (19), local growth rate,  $G_c$ , can be defined as the normalized time rate of change of  $F_c$ :

$$G_c = \frac{2\pi}{n_c} \cdot \frac{1}{F_c} \frac{\partial F_c}{\partial t'} = -4\pi B \tan(Bn_c t') \quad (29)$$

Evidently,  $G_c$  decreases from infinity at the modulation nodes (where the carrier amplitude vanishes) to zero at the antinodes, and has intermediate values within the range  $(0.6 > G > 0.2)$  of the convergent channel experiments.

That value of growth rate,  $G'_c$ , corresponding to the onset of breaking ( $H_c/L_c \doteq 0.13$ ) can be determined through substitution of (27) into (29):

$$G'_c = -4\pi B \left[ \left( \frac{2a/L_c}{0.065} \right)^2 - 1 \right]^{1/2} \quad (30)$$

which, expectedly, is a function only of the carrier steepness index,  $2a/L$ , and the frequency ratio parameter,  $B$ . If, as in the convergent channel, the subsequent breaking history is characterized by equilibrium between growth rate and breaking energy loss rate, breaking steepness will thereafter remain constant until the wave reaches the antinode of the original modulation envelope, ( $G_c = 0$ ), where breaking ceases as growth rate begins to diminish. Thereafter, the reduced modulation envelope is defined by,  $\eta_m = 0.13L_c \cos(Bn_c t')$ , as shown by the dashed curves in Fig. 31b. Similarly, the breaking duration,  $t_b$ , in carrier wave periods,  $T_c$ , can be determined from (29) and (30):

$$t_b/T_c = - \frac{1}{2\pi B} \arctan \left[ \left( \frac{2a/L_c}{0.065} \right)^2 - 1 \right]^{1/2} \quad (31)$$

The mean fractional breaking energy dissipation rate per carrier wave period is here most conveniently determined by considering the wave group as a black box whose input energy flux is  $C_m E_1$  and output flux is  $C_m E_2$ . The fractional dissipation rate,  $Q_c$ , is then the ratio of the energy

lost in a wave period to the average energy present:

$$Q_c = C_m T_c (E_1 - E_2) / L_c E_1 = (C_m / C_c) (1 - E_2 / E_1) \quad (32)$$

Since, after breaking, the energy density ratio is  $E_2 / E_1 = [0.065 / (2a / L_c)]^2$  and recalling that  $C_m$  and  $C_c$  are functions only of the biharmonic frequency ratio  $\alpha = n_2 / n_1$ , (32) becomes, finally:

$$Q_c = \frac{1 + \alpha^2}{(1 + \alpha)^2} \left[ 1 - \frac{0.065}{2a / L_c} \right]^2 \quad (33)$$

All of the foregoing results are summarized in Fig. 32, in which isolines  $a, \alpha, G'_c$ , and  $Q_c$  are drawn in a coordinate system with steepness index as ordinate and breaking duration as abscissa. While it would have been more orthodox to use  $\alpha$  as an independent variable than  $t_b / T_c$ , the above representation provides clearer distinction between the other variables. The reasonable range of natural sea conditions is effectively bounded by the lines  $0.6 < \alpha < 0.9$ , corresponding, roughly, to  $N = 1$  and  $N = 5$  waves per wave group, as indicated by numbers in parentheses. The shaded region covers the range of experimental values of these parameters determined for the convergent wave channel.

The conclusions inferred from this (admittedly-simplified) model for biharmonic breaking are, tentatively, the following. Note, first, that breaking losses are determined almost solely by the steepness index, and are almost independent of breaking kinematics.<sup>1</sup> This is a result of the assumption of equilibrium breaking within the black box, which uniformly truncates the wave envelope. Figure 32 indicates that for small  $\alpha$  (wide component frequency separation), there will be only one or two waves in a group; growth rate will be high and breaking, presumably, intense, but breaking duration is short. Conversely, for large  $\alpha$ , there will be many waves in a group, associated with low growth rate and weak breaking of longer duration. Within the region of practical interest, these effects tend to compensate, so that total breaking loss remains nearly constant.

Second, as regards application of the biharmonic model to wind wave breaking, Longuet-Higgins (1969b) and Hasselmann (1974) indirectly arrive at estimates of order  $10^{-4}$  and  $10^{-3}$ , respectively for breaking energy

<sup>1</sup>All breaking loss curves in Fig. 32 drop hyperbolically to zero near the left margin. This is because breaking is limited by decreasing steepness when there is less than one wave per group.



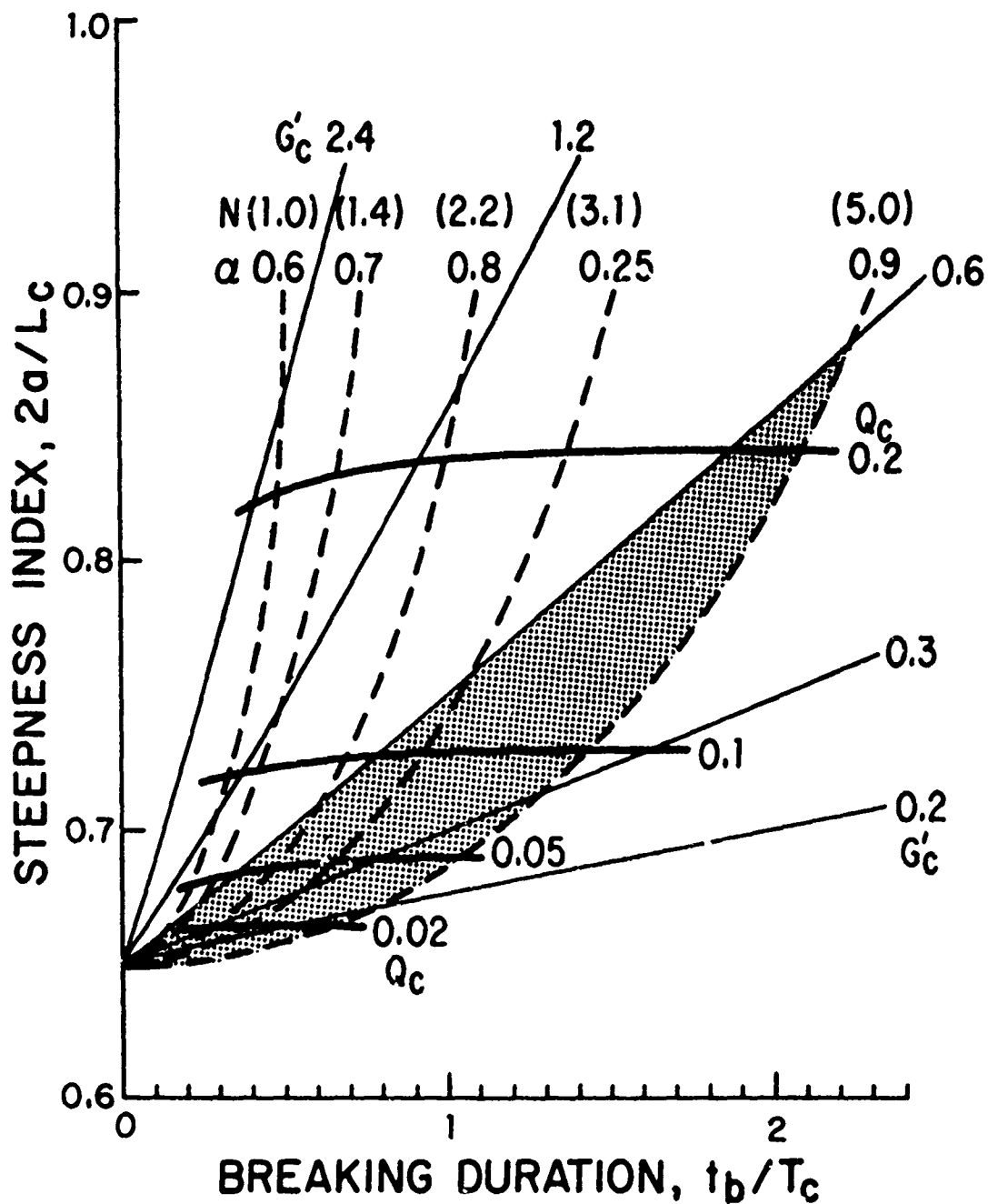


Fig. 32 Isolines of growth rate  $G'_c$  at breaking, frequency ratio  $\alpha = n_2/n_1$ , and equilibrium breaking energy loss  $Q_c$ , as functions of carrier wave steepness index  $2a/L_c$  and breaking duration  $t_b/T_c$ . Shaded area shows region of overlap between present experiments and narrow-band ocean wave interactions.

loss per mean wave cycle within the equilibrium range of the energy spectrum. The first estimate supposes a narrow spectrum, and the second a breaking duration short compared with the 'period' of the principal waves. With these restrictions, Fig. 32 indicates loss rates of order  $10^{-2}$ . However, the present model is unidirectional and assumes infinite crest length. The geometric extension to bidirectionality would have the effect of additional crest-wise modulation of wave steepness, and hence breaking. A rough estimate suggests that this would reduce loss rates by about an order of magnitude.

Thus, despite neglect of randomness, the influence of wind shear, and internal energy transfer among frequencies, the present biharmonic model, extended to include directionality, appears to be not too far removed from reality to warrant further study. The principal results suggest that breaking losses depend mainly upon steepness and breaking duration (via  $G'_c$ ) and are largely independent of frequency. The former variables are amenable to field observation and laboratory study, and form the basis for further work in this important and relatively unexplored area of wave dynamics.

## BIBLIOGRAPHY

- BEACH EROSION BOARD (1941) A study of progressive oscillatory waves in water. Tech. Report #1, U.S. Army Corps of Engineers, Washington, D.C.
- DEAN, R.G. (1965) Stream function representation of nonlinear ocean waves. J. Geophys. Res. 70 (18): 4561-4572.
- DONELAN, M.; M.S. Longuet-Higgins and J.S. Turner (1972) Periodicity in whitecaps. Nature, 239: 449-451.
- DUNCAN, W.J.; A.S. Thom, and A.D. Young (1970) Mechanics of Fluids (2nd ed.). American Elsevier, New York.
- HASSELMANN, K. (1974) On the Spectral Dissipation of Waves due to White-Capping, Boundary-Layer Meteorology, 6 (1/2): 107-127.
- HAYES, W.D. (1973) Group velocity and nonlinear dispersive wave propagation. Proc. Roy. Soc. Lond. A, 322: 199-321.
- HINZE, J.O. (1959) Turbulence, McGraw-Hill Book Co. Inc., New York.
- HOEL, P.G. (1947), Introduction to Mathematical Statistics, John Wiley & Sons. Inc., New York.
- JENKINS, G.M. and D.G. Watts (1968) Spectral Analysis and its Applications. Holden-Day, San Francisco.
- KINSMAN, B. (1965) Wind Waves. Prentice-Hall, Englewood Cliffs, New Jersey.
- LAMB, H. (1932) Hydrodynamics (6th ed.). Cambridge Univ. Press, London (Reprinted by Dover, New York, 1945).
- LE MEHAUTE, B., D. Divoky, and A. Lin, (1968) Internal characteristics of explosion-generated waves on the continental shelf. Tetra Tech Report No. TC-116, prepared Defense Atomic Support Agency contract DASA 01-67-C-0099.
- LONGUET-HIGGINS, M.S. (1969a) Anonlinear mechanism for the generation of sea waves. Proc. Roy. Soc. A, 311: 371-389.
- LONGUET-HIGGINS, M.S. (1969b) on wave breaking and the equilibrium spectrum of wind-generated waves. Proc. Roy. Soc. A, 310: 151-159.
- LONGUET-HIGGINS, M.S. (1973) A model of flow separation at a free surface. J. Fluid Mech., 57(1): 129-148.
- LONGUET-HIGGINS, M.S. (1974) An 'entraining plume' model of a spilling breaker. J. Fluid Mech. 63(1): 1-20.
- MADSEN, O.S. (1971) On the Generation of Long Waves, Jour. Geophys. Res. 76(36): 8672-8683.

- MICHE, M. (1954) Undulatory movements of the sea in constant or decreasing depth. University of California, Institute of Engineering Res., Wave Research Laboratory, Series 3, Issue 363.
- MICHELL, J.H. (1893) The highest waves in water. Phil. Mag., 36(5): 430-437.
- MONKMEYER, P.L., and J.E. Kutzbach (1965) A higher order theory for deep water waves. Conf. on Coastal Eng. Specialty Proc., Chapter 13: 301-326.
- MORISON, J.R. and R.C. Crooke (1953) The mechanics of deep water, shallow water, and breaking waves. Beach Erosion Board, Tech. Memo. No. 40, U.S. Army, Corps of Engineers, Washington, D.C.
- PHILLIPS, O.M. (1969) The Dynamics of the Upper Ocean. Univ. Press, Cambridge.
- PIERSON, W.J. and L. Moskowitz (1964) A proposed spectral form for fully developed wind seas based on the similarity theory of S.A. Kitaigorodskii. J. Geophysical Res. 69(24): 5181-5190.
- PRICE, R.K. (1971) Detailed structure of the breaking wave. J. Geophysical Res. 75(27): 5276-5278.
- RYE, H. (1974) Relative crest lengths of sea and swell. J. Physical Ocean. 3(4): 492-493.
- SKJELBRIA, L. and J. Hendrickson (1960) Fifth order gravity wave theory. Proc. of Conf. on Coastal Eng., Chapter 10, pp. 184-196.
- SNYDER, R.L. and C.S. Cox (1966) A field study of the wind generation of ocean waves. SIO Contribution, New Series #2007, vol. 36, 40 pp.
- TOPPING, J. (1962) Errors of Observation and Their Treatment (3rd ed.). Chapman and Hall, London.
- VAN DORN, W.G. (1966) Boundary dissipation of oscillatory waves. J. Fluid Mech., 24(4): 769-779.
- VAN DORN, W.G. (1975) Laboratory Study of Wave Breaking, Part I, Shallow Water Waves, In Press.

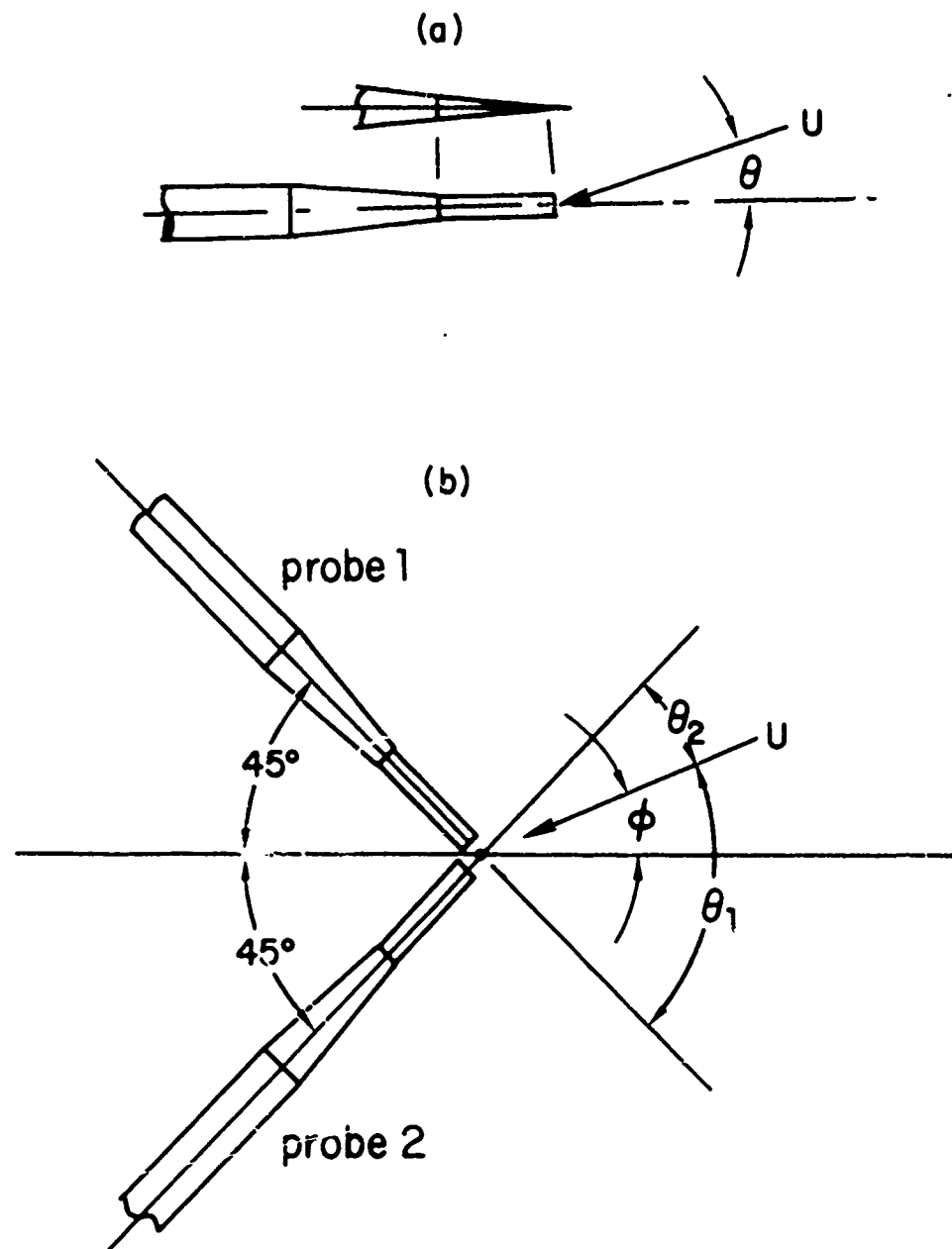


Fig. A-1 (a) single, and (b) orthogonal, hot film probe geometry.

## APPENDIX A

### Determination of Fluid Velocity and Direction

The functional part of the DISA 55A81 hot film probes used in these experiments consists of a wedge-shaped quartz rod about 3 mm in diameter on whose chisel edge is sputtered a resistive nickel film element 1 mm long by 0.35 mm wide. When connected to a DISA 55D01 constant temperature anemometer, DISA claims a frequency response of over 30 khz in water over the velocity range  $10 < U < 2500$  cm/sec. This response is sufficiently rapid to assure equilibrium output by the time the probe tip--initially in air--has penetrated a distance of 0.1 mm into a vertical wave front moving at 300 cm/sec.

The anemometer output is an analog voltage  $V$ , functionally related to the relative flow velocity  $U$  past the probe tip by:

$$V^2 - V_0^2 = A(\theta)U^n \quad (A-1)$$

where  $V_0$  is the no-flow voltage,  $\theta$  is the probe yaw angle (Fig. A-1a)<sup>1</sup>. The physical "constant"  $n$  and the normalized directional coefficient,  $A(\theta)$ , are determined for each probe by calibration.<sup>2</sup> Figure A-2 shows a representative set of calibration curves made in the 500 ft Lockheed towing tank in San Diego, and covering the range of flow velocities ( $30 < U < 550$  cm/sec) and yaw angles ( $0 < \theta < \pi/2$ ) common to these experiments.<sup>3</sup> The following general comments can be made.

- o The fact that these curves are not straight lines shows that  $n \neq$  constant, but decreases slightly with increasing velocity. Because fitting these curves with even the simplest polynomial approximation greatly increases the complexity of determining angular response, they were, instead, approximated by two straight lines of slope  $n_a$  for  $30 < U < 65$  cm/sec, and  $n_b$  for  $65 < U < 300$  cm/sec, respectively. As later shown, this simplification introduced errors of less than 6 cm/sec over the entire velocity range.

<sup>1</sup>Since an investigation of pitch response indicated less than 1% of error due to cross channel velocities, the pre-breaking measurements were essentially two-dimensional.

<sup>2</sup>While the angular response of hot wire probes can be approximated from physical principles (Hinze, 1959, Ch. 2), flow perturbations induced by a film probe's shape and attitude proscribe simple analysis.

<sup>3</sup>The calibrations actually extended over yaw angles from  $-\pi/2$  to  $\pi/2$  in order to resolve small probe asymmetries.

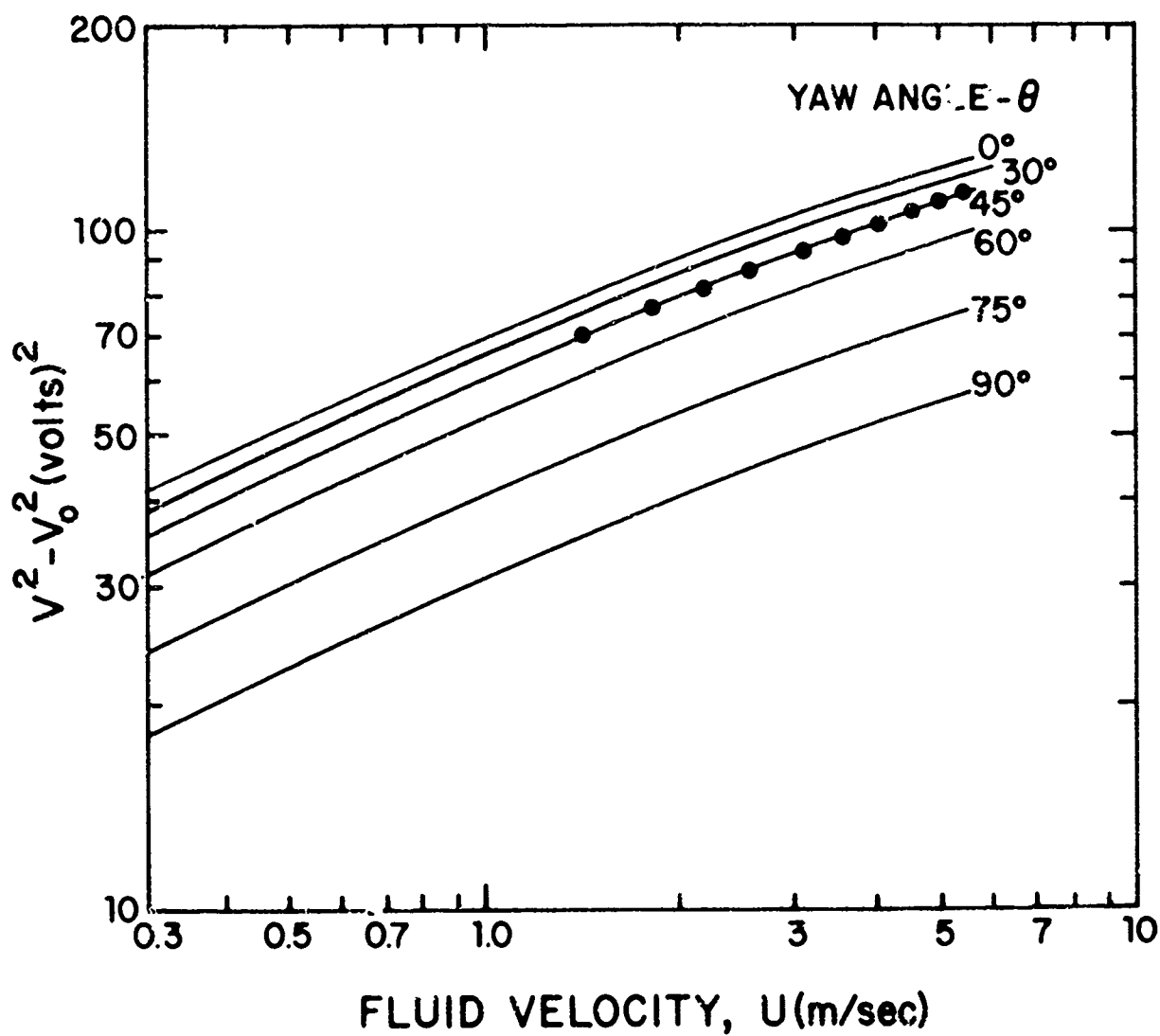


Fig. A-2 Representative individual probe calibration.

- o The fact that all curves have everywhere the same slope at any given velocity made it possible to use the same values of  $n_a$  and  $n_b$  for all yaw angles.
- o Repeat calibrations at different temperatures in a closed water tunnel at the University's Applied Mathematical and Engineering Science Laboratory established the temperature independence of  $n_a$ , and  $n_b$ , and yaw response.

Since polar plots of normalized yaw response  $g(\theta) = [A(\theta) - A(\pi/2)] / [A(0) - A(\pi/2)]$  exhibited slight sinusoidal perturbations, the response of each probe was expanded in truncated Fourier series:

$$g(\theta) = \sum_{i=0}^6 g_i \cos 2i\theta. \quad (A-2)$$

The Fourier coefficients  $g_i$  were determined for 13 yaw angles in  $15^\circ$ -increments and for 7-10 velocities within the range  $30 < U < 550$  cm/sec. by standard methods. Representative values of  $g_i$  for a single probe, averaged over seven velocities, together with their respective standard deviations  $\Delta g_i$ , are listed in Table A-1. For the first two coefficients, which account for about 90 percent of the total contribution to  $g(\theta)$ , the proportional error  $\Delta g_i / g_i$  is less than 0.01. Such small deviations indicate that the probe's angular response is essentially independent of velocity.

Table A-1

index (i)	0	1	2	3	4	5	6
$g_i$	0.649	0.442	-0.122	0.043	-0.020	0.016	-0.008
$\Delta g_i$	.005	.004	.005	.003	.003	.003	.002

The directional ambiguity  $\Delta\theta(\theta)$  associated with these deviations  $\Delta g_i$  can be estimated by setting  $\sum_{i=0}^6 \frac{\partial g(\theta)}{\partial g_i} \Delta g_i + \frac{\partial g(\theta)}{\partial \theta} \Delta\theta = 0$  and solving for  $\Delta\theta(\theta)$ :

$$\Delta\theta(\theta) = \frac{\sum_{i=0}^6 \Delta g_i \cos 2i\theta}{\sum_{i=0}^6 2ig_i \sin 2i\theta} \quad (A-3)$$

which can be evaluated from the data in Table A-1 for any yaw angle  $\theta$ . The results are shown in Table A-2, from which it is apparent that the directional ambiguity of a single probe is always small, except near  $\theta = 0$ , for which  $\sin 2i\theta \rightarrow 0$  and the angular response becomes indeterminate. However, for a pair of orthogonal probes, the directional ambiguity is always determinable and small (see below).



Table A-2

Flow angle $\theta$ (degrees)	0	10	20	30	40	50	60	70	80	90
Ambiguity $\theta$ (degrees)	$\infty$	4.0	0.3	0.6	0.3	0	0.1	0.1	0.1	2.0

Having verified the form of the probe response equation (A-1), it remains to generalize the factor  $A(\theta)$  in terms of the normalized directional response  $g(\theta)$  and some measureable response parameter, say  $A(\pi/4)$ , since all probes were dynamically calibrated at  $\theta = \pi/4$  in these experiments. To do this, it was found convenient to define an additional directional constant which, like the coefficients  $g_i$  could be evaluated from a complete directional calibration of each probe, and stored for later use. Of several alternatives, the definition:  $g^* = g_0 + A(\pi/2)/[A(0) - A(\pi/2)]$ , where  $g_0$  is the first Fourier coefficient in A-2, leads to a particularly simple expression for directional response:

$$A(\theta) = A(\pi/2) \left[ \frac{g^* + g(\theta)}{g^* + g(\pi/4)} \right] \quad (A-4)$$

The values of  $g^*$  obtained for each probe were all found to fall within the range  $1.0 < g^* < 1.15$ , and can be thought of as being related to slight physical eccentricities. The simplification  $g^* = 1.0$  would lead to directional errors of a few degrees, which is sufficient for most practical purposes. However the constants actually determined were employed in all data analysis.

Since the anemometer output is the product of a velocity function and a directional function, two probes were needed to resolve these functions separately. In the present experiments, the two probes were mounted in the vertical plane of the probe turret so that their tips nearly abutted at right angles (Fig. A-1b). Although the turret was rotatable in  $45^\circ$  increments, consider first the configuration shown, for which the unknown flow has a velocity  $U$  and a direction making an angle  $\theta$  with the (horizontal) bisector of the probe axes. If the probe (anemometer) outputs are defined by:  $P_1 = (V^2 - V_0^2)_1 = U^{n_1} A_1(\theta_1) = U^{n_1} A_1(\theta + \pi/4)$  and  $P_2 = (V^2 - V_0^2)_2 = U^{n_2} A_2(\theta_2) = U^{n_2} A_2(\theta - \pi/4)$ , then, for all  $\theta$  within the range  $\pi/4 > \theta > -\pi/4$ , the ratio of the directional coefficients is unique. If the probes had identical velocity responses, so that  $n_1 = n_2$ ,  $\theta$  could be obtained by computing  $P_1/P_2$  and searching a table of  $A_1/A_2$  for the corresponding value. However, even where  $n_1 \neq n_2$ , one can use an analogous

procedure. Letting  $m = n_2/n_1$ , we can write:

$$P_1^m/P_2 = A_1^m(\theta + \pi/4)/A_2(\theta - \pi/4), \quad (A-5)$$

from which  $\theta$  can be found from a table of  $A_1^m/A_2$ . Spurious ratios of  $P_1^m/P_2$ , such as may occur with one probe out of water, will fall outside the range of this table. Having found  $\theta$ , the corresponding flow velocity  $U$  is given explicitly for either probe by:

$$U = \exp [(1/n) \ln(P/A)] \quad (A-6)$$

Separate directional calibration of individual probes in the Lockheed towing tank was considered to be much more efficient and inherently more accurate than calibrating them by pairs in the turret head, which would have required a much larger number of test runs. Once all probes were calibrated and their Fourier coefficients  $g_i$  and directional constants stored on punch cards, they could be exchanged in the turret at any time when there was evidence of malfunction. Altogether, only five different probes were used in the course of three months of data taking. Probe failure was usually evidenced by progressive loss of sensitivity after several hundred hours of use.

During data runs, the turret-mounted probe pairs were dynamically calibrated at the fixed yaw angles  $\theta_1 = -\theta_2 = \pi/4$  ( $\theta = 0$ ) over the velocity range  $80 < U < 550$  cm/sec, as follows. The probe turret mounting strut was first elevated to an indexed position and rotated  $90^\circ$  until the turret locked into place with the probe bisector vertically centered on the 0.9 cm-diameter discharge orifice in the bottom of the jet calibrate cylinder (Fig. A-3). This cylinder was about 10 cm in diameter and 2 m high, and was equipped with an orifice plug valve (initially closed), and 11 pairs of shorting contacts up its side. The cylinder was filled with water pumped directly from the wave channel so as to provide a calibration at the in situ temperature of the channel. The plug valve was then opened, and the issuing jet impinged symmetrically upon the probe tips about 1.2 cm beneath. As the water level in the cylinder fell consecutively below each contact pair, an electrical signal instructed the computer to sample two anemometer voltages  $V_1$  and  $V_2$ . The turret strut was then returned to the vertical and lowered until the turret was immersed, and the computer instructed by push button to sample the no-flow anemometer outputs  $V_{o1}$  and  $V_{o2}$ . The computer, having previously been supplied with jet

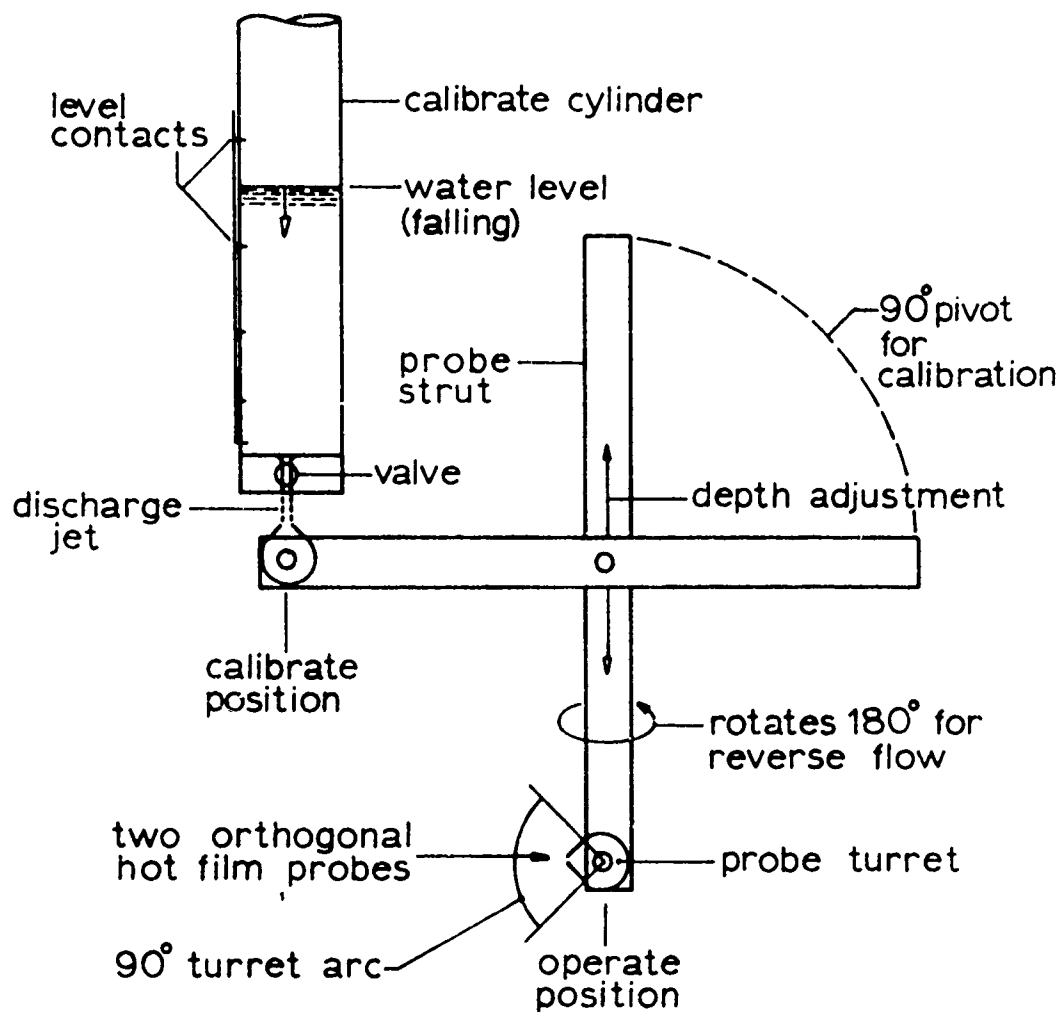


Fig. A-3 Method of mounting strut for hot-film velocity probes for elevation, reversal, and calibration.

velocities corresponding to the 11 contact pairs<sup>1</sup>, then plotted  $\ln(V^2 - V_0^2)$  vs  $\ln U$  for each probe. These points were fitted with a straight line and its intercepts at  $\ln U = 4$  and 6 read off, from which the calibration constants  $n$  and  $A(\pi/4)$  were computed and stored for later use. The data points plotted in Fig. A-2 show how closely a typical cylinder calibration fits the  $45^\circ$  yaw angle curve obtained from the directional towing tank tests. From analysis of randomly selected cylinder calibrations it was concluded that the computed directional resolution was accurate to within  $2^\circ$  at most, and usually much less than  $1^\circ$ , and that the velocity resolution above 65 cm/sec was within 3%. The constant  $n_a$  for the velocity range  $30 < U < 65$  cm/sec could not be determined from cylinder calibrations. However, repeated spinning tank tests at  $\theta = 0$  showed that all probes had very similar low-velocity responses, and rms value  $n_a = 0.54$  was used to compute all velocities within this range. The best error estimate for low velocities was  $3^\circ$  in direction and  $\pm 6$  cm/sec in velocity. This amounted to fairly large percentage errors in velocity, but because the velocities were low, the errors did not significantly affect the overall results or the conclusions drawn.

---

<sup>1</sup>These were determined independently by calculation and by weighing the discharge at constant contact levels.

## APPENDIX B

### Purity of Generated Waves

It is now well known (Madsen, 1971) that, unless a periodic wave-maker produces particle displacements closely akin to those of the desired waves in stationary sequence, free secondary waves will be generated in phase with the second harmonic of the paddle frequency. Because the primary and secondary waves travel at different speeds, the wave profile may suffer progressive distortion. This phenomenon is particularly important in shallow water (Van Dorn, 1975), but was examined here as a possible contributor to wave asymmetry even though the depth was always half the primary wavelength.

Figure B-1 shows three frequency (potential energy) spectra calculated by Fourier methods (Jenkins and Watts, 1968) from 25-second wave staff records of 0.66 hz waves at stations D-2, F-2, and G-2 (Table D). Although relatively close to the wave paddle (593 cm), the waves were sufficiently high ( $h = 50$  cm) and steep ( $H/L = 0.12$ ) as to represent extreme conditions for all wave series in these experiments.

All three spectra are coherent to at least the 4th harmonic, with sharp peaks centered on integer multiples of 0.66 hz. The primary peak contained at least 70% of the potential energy in a band 0.04 hz wide, and over 90% in a 0.2 hz band. The 2d harmonic contains only about 6% of the energy of the primary. Corresponding spectra at increasing distance from the paddle exhibited no detectible phase shift of the 2d or higher harmonics. Accordingly, it was concluded that free waves--if present--were too low to significantly affect the results reported here.

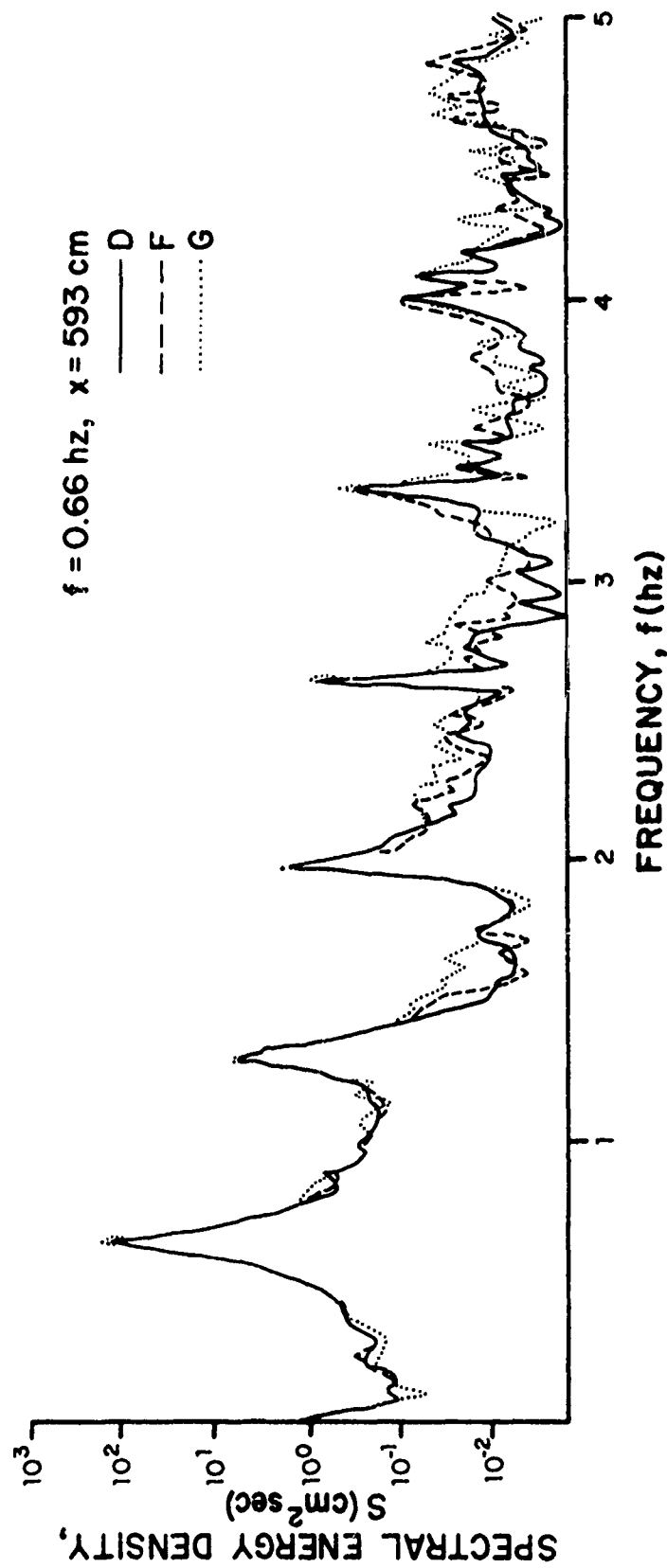


Fig. B-1 Comparison of spectra from different wave series.

## APPENDIX C

### Energy Error Arising from Assumed Stationarity

The assumption of stationarity implies that potential energy calculated from a time series of surface elevation at a fixed location (Eq. 14) is equivalent to that which would be obtained from a spatial profile at a corresponding instant (Eq. 15). An estimate of the associated error was obtained as follows.

Surface elevation can be expressed as a sum of harmonics:

$$\eta(t, x) = a_1(x) \cos \theta + a_2(x) \cos 2\theta + a_3(x) \cos 3\theta + \dots, \quad (C-1)$$

where  $k = \partial \theta / \partial x$ ,  $\omega = \partial \theta / \partial t$ ,  $x$  is distance along the channel from an arbitrary origin, and  $k$  is a slowly varying wavenumber. If variation is small,  $a_n(x)$ ,  $n = 1, \dots$ , can be represented by the first two terms of a Taylor's series,

$$a_n(x) = a_{n0} + a_{n1}x + \dots; \quad n = 1, 2, \dots \quad (C-2)$$

The integral definitions of equations (14), and (15) are respectively,

$$E_p = \frac{1}{2T} \int_{-T/2}^{T/2} \eta(t, 0)^2 dt, \quad (C-3a)$$

$$E_{px} = \frac{1}{2L} \int_{-L/2}^{L/2} \eta(0, x)^2 dx, \quad (C-3b)$$

Using equations (C-1), (C-2), and the identities  $\int_{-\pi}^{\pi} y \cos^2 ny \, dy = 0$ , and  $\int_{-\pi}^{\pi} y^2 \cos^2 ny \, dy = \pi^3/3 + \pi/2n^2$ , where  $n = 1, 2, 3, \dots, \infty$ , these can be written:

$$E_p = \frac{1}{8\pi} \sum_n a_{n0}^2, \quad (C-4a)$$

$$E_{px} = \frac{1}{8\pi} \sum_n \{a_{n0}^2 + L^2 a_{n1}^2 [\frac{\pi}{6} + \frac{1}{4\pi n^2}]\}, \quad (C-4b)$$

and their normalized difference is

$$\frac{E_{px} - E_p}{E_p} \leq \frac{L_*^2 [0.6 a_{11}^2 + 0.54 a_{21}^2]}{a_{10}^2 + a_{20}^2} \quad (C-5)$$

Since most of the wave energy is contained in harmonic peaks of the

energy spectrum (Appendix B), the  $a_{10}$ ,  $a_{20}$ ,  $a_{11}$ ,  $a_{21}$  coefficients are related to potential energy spectra by,

$$S(nf_0, x) = (a_{n0} + a_{n1}x)^2, \quad (C-6)$$

where  $S(f, x)$  is the calculated spectral potential energy in 0.12 hz bands about harmonics of paddle frequency,  $nf_0$ . Because the spatial variation of energy was found to be approximately proportional to growth rate, equation (C-5) was evaluated from the representative spectrum of an 0.66 hz wave at high growth rate,  $G$ , as follows:

$$S(f_0, x_1) = 146, S(2f_0, x_1) = 4, x_1 = -193.5 \text{ cm}, (G = 0.448)$$

$$S(f_0, x_2) = 208, S(2f_0, x_2) = 6, x_2 = 193.5 \text{ cm}, (G = 0.75)$$

where the origin has been shifted so that  $x_1 + x_2 = 0$ . If the ratio of spectral densities at  $x_1$  and  $x_2$  is defined by  $R^2(f) = S(f, x_1)/S(f, x_2)$ , the ratios  $a_{n1}/a_{n0}$  can be determined in terms of  $R(f)$ :

$$a_{11}/a_{10} = 2(x_2 - x_1)^{-1} [(1 - R(f_0))/(1 + R(f_0))] = 0.00046 \text{ (cm}^{-1}\text{)}$$

$$a_{21}/a_{20} = 2(x_2 - x_1)^{-1} [(1 - R(2f_0))/(1 + R(2f_0))] = 0.00046 \text{ (cm}^{-1}\text{)}$$

The smallness of these ratios tends to support the Taylor's series truncation after two terms.

The values of  $a_{n0}^2$  found by substituting  $a_{n1}/a_{n0}$  ratios into equation (C-6) were determined to be  $a_{10}^2 = 177$ , and  $a_{20}^2 = 5$ , from which (C-5) was determined to be:  $(E_{px} - E_p)/E_p \doteq 0.028$ , or less than 3%.



## APPENDIX D

### Wave Height and Potential Energy

This table is a computerized printout of wave heights and mean-square surface elevations calculated automatically from time series elevation measurements at individual wave staffs. The table is divided into three sections in order of increasing paddle frequency,  $f$ . Each section is subdivided into consecutive wave series, A,B,C..., in order of increasing paddle stroke. Each series listing gives, from left to right, a station number, paddle distance, channel width, and the corresponding wave heights and potential energies of the first four uniform waves averaged over three consecutive data runs at a wave staff 9 cm from the channel sidewall. Corresponding data for an additional cross-channel staff at some stations appear in the last two columns.

Wave heights were calculated as the maximum elevation differences in the time series, and energies as half the time-variance of elevation, averaged over a wave period. These values were arithmetically averaged over the triplicated repeat runs to give the table entries.

Table 13.13

Wave frequency:  $f = 0.66$  Hz, Depth  $D = 187$  cm.

[illegible]

TABLE D (continued)

Wave frequency $f = 0.60$ Hz, Depth $D = 18.7$ cm.																			
Station	Paddle Distance $x$ (cm)	Channel Width $w$ (cm)	Average Wave Height				Average Pot. Energy				Staff near Wall				Staff near Convergence				
			$H_1$	$H_2$	$H_3$	$H_4$	$E_{p1}$	$E_{p2}$	$E_{p3}$	$E_{p4}$	$H_1$	$H_2$	$H_3$	$H_4$	$E_{p1}$	$E_{p2}$	$E_{p3}$	$E_{p4}$	
D	1	357.	48	49	50	43	124	129	131	130									
	2	593.	49	51	48	45	123	131	129	112	50	50	51	52	152	149	145	151	
	3	833.	50	51	51	52	130	126	134	124									
	4	1069.	55	51	50	49	159	144	140	137	54	52	53	54	147	151	156	153	
	5	1186.	52	50	53	53	145	141	138	150									
	6	1379.																	
	7	1422.	54	56	55	55	157	158	172	165	51	53	48	50	156	164	146	138	
	8	1415.	44	44	45	47	117	119	122	130									
	9	1766.	42	44	41	43	115	102	111	117	46	47	46	46	129	112	126	130	
	10	2002.	55.																
E	1	586.	50	49	52	50	140	133	146	144									
	2	689.	48	46	48	46	105	107	105	103									
	3	857.	46	47	48	46	120	112	117	108	54	53	56	52	150	150	155	145	
	4	959.	51	52	56	53	149	145	158	154	55	52	53	50	154	144	143	133	
	5	1118.	55	53	55	51	142	155	148	141									
	6	1388.	55	59	54	56	151	161	155	164	50	58	52	58	145	158	146	154	
F	1	357.	48	52	50	50	130	133	130	138									
	2	593.	47	48	47	46	124	126	125	115	52	53	54	51	157	149	152	150	
	3	833.	51	51	50	52	137	142	125	125									
	4	1069.	53	54	52	48	147	148	137	131	52	51	54	51	140	149	156	152	
	5	1186.	49	50	49	50	137	139	140	142									
	6	1379.	51	43	53	51	134	137	125	136									
	7	1422.	45	43	48	49	118	108	121	134	46	44	47	43	127	133	118	122	
	8	1615.	46	46	49	49	121	116	120	142	48	50	46	44	139	109	121	125	
	9	1766.	47	43	43	46	115	120	111	111									
	10	2002.	46	44	44	43	114	108	108	107	44	46	43	41	122	108	109	111	
G	1	357.	49	52	53	53	133	141	141	145									
	2	593.	51	50	51	48	143	138	146	129	55	52	52	50	158	152	150	149	
	3	833.	46	44	44	43	119	115	111	116									
	4	1069.	48	47	48	43	135	123	130	112	42	44	47	47	111	110	128	133	
	5	1186.	44	50	53	58	119	133	157	158									
	6	1379.	58	39	40	42	86	91	101	108									
	7	1422.	38	38	43	41	94	87	109	108	42	43	51	44	109	122	121	122	
	8	1615.	42	41	42	44	88	98	101	102	42	39	39	44	96	102	109	105	
	9	1766.	41	43	43	45	104	111	104	106									
	10	2002.	48	47	45	47	118	124	141	134	48	49	45	46	117	122	137	112	



TABLE D (continued)

Wave frequency  $f = 0.73$  Hz, Depth  $D = 154$  cm,

Station	Paddle Distance x (cm)	Channel Width w (cm)	Average Wave Height				Average Pot. Energy				Average Wave Height				Average Pot. Energy			
			H <sub>1</sub>	H <sub>2</sub>	H <sub>3</sub>	H <sub>4</sub>	E <sub>p1</sub>	E <sub>p2</sub>	E <sub>p3</sub>	E <sub>p4</sub>	H <sub>1</sub>	H <sub>2</sub>	H <sub>3</sub>	H <sub>4</sub>	E <sub>p1</sub>	E <sub>p2</sub>	E <sub>p3</sub>	E <sub>p4</sub>
1	517.	198.	36	36	38	38	76	76	81	83								
2	753.	175.	42	41	40	38	97	92	91	91								
3	914.	160.	39	39	39	38	86	81	65	65								
4	1094.	162.	43	44	44	45	107	108	104	111								
5	1180.	134.	46	46	47	48	111	118	117	121								
6	1330.	120.	47	47	47	48	114	119	117	117								
7	1428.	110.	47	45	43	45	115	110	108	111								
8	1561.	97.	42	37	37	41	105	82	90	104								
9	1664.	87.	45	41	37	39	105	93	82	89								
0	1797.	75.	33	32	40	36	71	79	78	74								
1	517.	198.	40	40	40	40	80	82	84	84								
2	753.	175.	41	40	41	39	94	88	91	85								
3	914.	160.	38	38	40	39	82	80	81	79								
4	1094.	142.	42	41	43	42	101	101	98	98								
5	1180.	134.	46	45	42	39	123	115	104	96								
6	1330.	120.	40	41	40	40	93	98	102	95								
7	1428.	110.	39	39	37	36	85	78	77	82								
8	1561.	97.	36	37	40	36	77	83	87	85								
9	1664.	87.	39	37	36	33	84	83	82	72								
0	1797.	75.	34	34	37	35	68	76	83	68								

**FOR VELOCITY MEASUREMENTS ONLY:**

1	891.	163.	33	34	36	34	32	34	35	34
2	1801.	75.	46	48	49	48	45	46	48	47

TABLE B (continued)

Wave frequency f = 0.80 Hz, Depth D = 132 cm.		Staff near wall				Staff near Convergence			
Station	Paddle Distance x (cm)	Channel Width w (cm)	Average Wave Height $H_1$	Average Wave Height $H_2$	Average Wave Height $H_3$	Average Wave Height $H_4$	Average Pot. Energy $E_{p1}$	Average Pot. Energy $E_{p2}$	Average Pot. Energy $E_{p3}$
			$H_1$	$H_2$	$H_3$	$H_4$	$E_{p1}$	$E_{p2}$	$E_{p3}$
			(cm)	(cm)	(cm)	(cm)	(cm <sup>2</sup> )	(cm <sup>2</sup> )	(cm <sup>2</sup> )
<b>A</b>									
1	804.	170.	17	17	17	18	18	18	19
2	1040.	148.	18	18	18	19	23	22	22
3	1056.	146.	19	19	19	20	22	24	23
4	1292.	123.	20	21	21	22	24	27	29
5	1532.	100.	23	23	22	22	31	33	33
6	1675.	86.	24	25	24	24	36	35	35
7	1768.	77.	25	25	25	25	39	40	37
8	1911.	64.	29	28	28	27	45	49	45
<b>B</b>									
1	804.	170.	29	29	30	29	49	51	50
2	1040.	148.	30	29	30	29	49	48	46
3	1056.	146.	30	29	31	31	53	52	54
4	1292.	123.	33	33	34	31	57	60	57
5	1532.	100.	38	38	41	37	79	79	85
6	1675.	86.	37	39	40	35	71	88	79
7	1768.	77.	41	39	38	38	85	81	78
8	1911.	64.	37	36	36	39	75	74	82
<b>C</b>									
1	804.	170.	31	32	32	32	57	57	61
2	1040.	148.	33	32	31	32	60	60	57
3	1056.	146.	30	32	33	31	53	57	58
4	1292.	123.	39	37	36	33	77	72	68
5	1532.	100.	39	39	42	40	86	90	86
6	1675.	86.	34	39	39	39	63	68	80
7	1768.	77.	39	40	37	40	69	83	88
8	1911.	64.	34	33	33	33	67	66	67
<b>D</b>									
1	804.	170.	33	33	32	33	61	62	62
2	1040.	148.	34	33	33	33	63	61	57
3	1056.	146.	35	36	34	35	67	69	66
4	1292.	123.	35	36	34	34	67	65	64
5	1532.	100.	38	37	39	33	82	77	65
6	1675.	86.	31	31	32	33	58	59	59
7	1768.	77.	38	24	25	28	97	53	44
8	1911.	64.	28	24	25	27	60	50	49

## APPENDIX E

### Wave Reflection

Systematic deviations of  $F/F_0$  from the line of conserved energy flux can be used to calculate an upper limit on the reflection term,  $Q_r(x)$ , in equation (10). Wave elevation time series,  $\eta(x,t)$ , can be represented as a sum of reflected,  $R$ , and transmitted,  $I$ , Fourier coefficients:

$$\eta(x,t) = \sum_j I_j e^{ik_j x} + R_j e^{-ik_j x + i\theta_j}, \quad (E-1)$$

where wavenumber  $k = 2\pi f/C_g$  (p. 27). Since the phase angle,  $\theta_j$ , determines the relative complex phases of reflected and transmitted coefficients, both  $I_j$  and  $R_j$  are real. Total potential energy is

$$\frac{1}{2} \rho g \eta^2 = \frac{1}{2} \rho g [I_j^2 + R_j^2 + 2I_j R_j \cos(k_j x - \theta_j)], \quad (E-2)$$

and by equation (16), the total energy flux is  $2C_{g5} \rho g \eta^2$ . Since over 90 percent of this sum is contained in the frequency band centered on the paddle stroke frequency,  $f$ , the energy flux is approximated by that single term. The normalized potential energy flux is approximately

$$[I^2/I_0^2] + [2IR \cos(kx - \theta)/I_0^2],$$

where  $I$  and  $R$  are the transmitted and reflected Fourier coefficients at the paddle frequency, respectively, and  $I_0$  is a transmitted Fourier coefficient corresponding to the normalizing energy flux,  $F_0$ . It is assumed that  $R_0^2 \ll I_0^2$ , and  $R^2 \ll I^2$ . An upper limit on normalized energy flux fluctuations due to the last term in (E-2), above, can be estimated from the 10 percent maximum deviations from the lines of conserved energy flux observed in Figures 25-27, at stations before breaking. Station spacing was close enough so that, for at least half of the stations,  $|\cos(kx - \theta)| > 0.5$ , which leads to  $0.1 > IR/I_0^2 > R/I$ . Therefore the ratio of reflected to transmitted energy,  $R^2/I^2$  was less than 0.01.

## APPENDIX F

### Error Estimates

Error estimates associated with velocity measurements are discussed in Appendix A. This section deals with the maximum probable errors in the operational data of waveheight, steepness, potential energy, and energy flux listed in Tables I and II (Section 5.1), which were derived by averaging from Table D, which, itself, represents averages from multiple data runs.

Except for steepness and energy flux, which involve phase and group velocities, respectively, all errors in the above parameters arise from variances in the measurement of surface elevation, compounded by averaging between cross-channel wave staffs, and among four uniform waves in a train and from three to 15 repetitive data runs.

While the number of individual staffs, uniform waves, and repeat runs was always too small to apply usual tests of statistical normality, the smallness of their fractional standard deviations ( $\sim 0.04$ ) implies that their meaned distributions are considerably more likely to be normal (Hoel, 1947, p. 69). Accordingly, with this assumption, if  $H_i = H_1 \dots H_4$  (Table D) are ensemble averages of wave height over  $N$  repeat runs, including cross-channel staffs, let  $H = H_i/2N$  and  $\bar{H} = H/4$  be the cross-channel and four-wave means, respectively, and  $\sigma(H) = [\langle \bar{H}^2 \rangle - \langle \bar{H} \rangle^2]^{1/2}$  and  $\sigma(\bar{H}) = \sigma(H)/2$  be their respective standard deviations (Topping, 1960). If similar terminology applies to the mean-square elevations (potential energies,  $E_p$ ) in Table D, then their respective 95% confidence limits are, approximately,  $\bar{H} \pm \sigma(\bar{H})$  and  $\bar{E}_p \pm \sigma(\bar{E}_p)$ .

Defining, now, the corresponding fractional errors in wave height and potential energy as,  $\sigma(\bar{H})/\bar{H}$  and  $\sigma(\bar{E}_p)/\bar{E}_p$ , using the previously estimated fractional error for phase velocity,  $\sigma C_5/C_5 = 0.03$  (Sect. 5.1.1), and assuming that for group velocity  $C_{g5}$  to be no larger, the respective error estimates for steepness,  $H/L = H/C_5 T$ , and for energy flux,  $F_t = 2C_{g5}E_p$ , become, finally (Ibid., p. 82):

$$\frac{\sigma(\bar{H}/L)}{\bar{H}/L} = \left[ \frac{\sigma(\bar{H})^2}{\bar{H}^2} + 0.03^2 \right]^{1/2}; \quad (F-1)$$



and

$$\frac{\sigma(\bar{F}_t)}{\bar{F}_t} = \left[ \frac{\sigma(E_p)^2}{\bar{E}_p^2} + 0.03^2 \right]^{1/2}. \quad (F-2)$$

The range of these estimates varied slightly between stations and wave series, but the overall 95% confidence limits for fractional errors listed in Section 5.1 are considered to be conservative.

## APPENDIX G

### Energy Partition in an Inhomogeneous Wave Field

For any conservative wave system, total energy is the sum of potential and kinetic energy; for small-amplitude waves, the two are equal. However, kinetic energy could not be determined in the present experiments because flow velocities were measured only under the wave crests. Since no means of calculating kinetic energy with inhomogeneous waves of finite amplitude, have been reported, resort was made to a result obtained by Davies (1951), for symmetric waves of finite amplitude. To fifth order, he gives:

$$E_k/E_p = 1 + \frac{1}{18}A^2 + \frac{25}{972}A^4 + \dots = 1.080 \quad (G-1)$$

where,  $A = 0.992$  for a Stokes wave of limiting steepness. Subject, then, only to the uncertainty imposed by inhomogeneity, the present assumption that  $E_p = E_k$  is only in error by about 4%, which is less than the fractional error estimate ( $\pm 3\%$ ) given in the previous section for the calculation of  $E_p$  itself.